THE UNIVERSITY OF CALGARY

Optimizing Georeferencing of Airborne Survey Systems by INS/DGPS

by

Jan Škaloud

A THESIS

SUBMITTED TO THE FACULTY OF GRADUATE STUDIES

IN PARTIAL FULFILLMENT OF THE REQUIREMENTS FOR THE

DEGREE OF DOCTOR OF PHILOSOPHY

DEPARTMENT OF GEOMATICS ENGINEERING

CALGARY, ALBERTA

MARCH, 1999

ABSTRACT

This research scrutinizes the method of INS/DGPS integration to provide the parameters of exterior orientation needed for direct georeferencing of airborne imagery more reliably and with better accuracy. Since the well established method of INS-GPS data integration by means of Kalman filtering suppresses sensor noise over a limited frequency bandwidth only, a new filtering methodology has been developed to optimally eliminate noise over the whole motion band of interest. The proposed method includes optimal band-limiting for the inertial signal and de-noising by use of wavelets. The latter accommodates a model for short-term inertial errors, especially applicable to ring-laser gyro and fibre optic gyro technologies and presents a technique for adaptive estimation of the model parameters based solely on data analysis. In the second part of the thesis, the influence of inertial measurements on the process of GPS ambiguity determination is investigated with the purpose of optimizing INS/DGPS integration in this respect. An analytical proof demonstrating in which cases data integration by means of a centralized Kalman filter provides considerable advantages over its de-centralized counterpart is presented, and the contribution of inertial systems of different accuracy classes is evaluated. In addition, the operational aspects of airborne mapping with INS/DGPS are analyzed and strategies for minimizing the effect of hardware integration errors on the process of direct georeferencing are proposed. Lastly, the feasibility of using INS/DGPS data for the derivation of the parameters of exterior orientation is demonstrated with respect to aerotriangulation without ground control.

ACKNOWLEDGMENTS

I would like to express my gratitude to my supervisor, Professor Klaus-Peter Schwarz, for his continuous support, encouragement, guidance throughout my studies and especially for his positive influence for years to come. To him also belongs the credit for maintaining a world class research team where work is fun and fun is work.

Many thanks go to Dr. Michael Sideris and Dr. Rod Blais for their comments on filtering methods and to Mr. Darren Cosandier for providing the software for the bundle adjustment. My friend Vladimir Argeseanu is gratefully acknowledged for polishing the language of this thesis. I also wish to express thanks to my past and present colleagues in the research group, especially to Dr. M. Wei, Mr. A. Bruton, Mr. C. Glennie, Mr. A. Mohamed and Mr. M. Mostafa for many fruitful discussions and the support given in many ways.

The financial support of this research, obtained through an NSERC grant of my supervisor, the Helmut Moritz Graduate Scholarship, Teaching and Research Assistantships of the University of Calgary, is gratefully acknowledged. Flight time and expertise was provided by the Rheinbraun AG-Department of Photogrammetry, Cologne. Thanks are due to the Stuttgart Institute of Photogrammetry, and especially Mr. Michael Cramer, for the time and effort spent on organizing and executing the flight test and to Mr. Werner Schneider for performing high quality photogrammetric measurements.

TABLE OF CONTENTS

LIST OF TABLES

LIST OF FIGURES

NOTATION

1. Convention

1.1 Vectors are represented by lower-case letters.

1.2 Matrices are represented by upper-case letters.

1.3 'Vector' means components of a vector. A superscript indicates the particular frame in which the vector is represented.

1.4 Rotation matrices between coordinate systems are defined by a subscript and a superscript denoting the two coordinate systems, (e.g. $\boldsymbol{R}_b^{\,l}$ indicates a transformation from the body frame (*b*) to the local-level frame (*l*)).

1.5 Angular velocity between two coordinates system may be expressed either by an angular velocity vector (e.g. $\omega^b{}_{ib}$ describes the rotation between the inertial and body frames expressed in the body frame) or by the corresponding skew-symmetric matrix

$$\Omega_{ib}^{b} = \begin{pmatrix} 0 & -\omega_z & \omega_y \\ \omega_z & 0 & -\omega_x \\ -\omega_y & \omega_x & 0 \end{pmatrix}$$

2. Coordinate Frames

Operational Inertial (i):

Approximate inertial frame of reference for INS measurements.

origin: at centre of mass of the Earth

x^i: towards the mean vernal equinox

y^i: completes a right-handed system

z^i: towards the mean celestial pole

Earth (e):

origin: at centre of mass of the Earth

x^e: towards the mean Greenwich meridian in the equatorial plane

y^e: completes a right-handed system

z^e: towards the mean celestial pole

The rotation of the earth-fixed frame with respect to the inertial frame is given by

$$\boldsymbol{\omega}_{\boldsymbol{ie}}^{\boldsymbol{e}} = \begin{pmatrix} 0 \\ 0 \\ \omega_{Earth} \end{pmatrix} = \begin{pmatrix} 0 \\ 0 \\ 7.2921158 \;\; rad \cdot \sec^{-1} \end{pmatrix}$$

Local-level (l)

Refers to the chosen reference ellipsoid.

origin: at the centre of the body frame

x^l: towards ellipsoidal east

y^l: towards ellipsoidal north

z^l: upwards along ellipsoidal normal

The transformation matrix between the local-level frame and the earth-fixed frame is:

$$\boldsymbol{R}_{\boldsymbol{l}}^{\boldsymbol{e}} = \begin{pmatrix} -\sin\lambda & -\sin\varphi\cos\lambda & \cos\varphi\cos\lambda \\ \cos\lambda & -\sin\varphi\sin\lambda & \cos\varphi\sin\lambda \\ 0 & \cos\varphi & \sin\varphi \end{pmatrix}$$

where,

φ is the geodetic latitude

λ is the geodetic longitude

Body frame (b):

origin: at the centre of the INS accelerometer triad

x^b: towards the right side of the INS block seen from the front panel

y^b: opposite to the front panel, generally in forward direction

z^b: upwards and completing a right-handed system

The transformation matrix between body frame and local-level frame is:

$$\boldsymbol{R}_b^l = \begin{pmatrix} \cos\varphi\cos\psi - \sin\theta\sin\varphi\sin\psi & -\cos\theta\sin\psi & \sin\varphi\cos\psi + \sin\theta\cos\varphi\sin\psi \\ \cos\varphi\sin\psi + \sin\theta\sin\varphi\cos\psi & \cos\theta\cos\psi & \sin\varphi\sin\psi - \sin\theta\cos\varphi\cos\psi \\ -\cos\theta\sin\varphi & \sin\theta & \cos\theta\cos\varphi \end{pmatrix}$$

where,

θ, φ, ψ are three Euler angles defined as:

θ pitch, around x-axis, positive counter-clockwise when seen from the positive end of the axis

φ roll, around y-axis, positive counter-clockwise when seen from the positive end of the axis

ψ yaw, around z-axis, positive counter-clockwise when seen from the positive end of the axis

In navigation applications, the axes of the body frame often correspond to the vehicle axes (i.e. x^b - right side, y^b - forward, z^b - upward). This requires a rigorous alignment between the body axes defined here and the vehicle axes (right, forward, upward).

Camera frame (c):

definition varies with the imagery type.

Mapping frame (m):

definition corresponds to the specific projections used.

3. Acronyms

3-D	Three dimensional
A/D	Analog/Digital
ADOP	Ambiguity Dilution of Precision
AFM	Ambiguity Function Method
AKF	Adaptive Kalman Filter
C/A Code	Coarse/Acquisition code
CASI	Compact Airborne Spectrographic Imager
CCD	Charge Coupled Devices
CKF	Conventional Kalman Filter
DD	Double difference
DGPS	Differential GPS
DIAS	Direct Integer Ambiguity Search
DOP	Dilution of Precision
DSP	Digital Signal Processing
DWT	Discrete Wavelet Transform
EM	Estimate Maximize
FARA	Fast Ambiguity Resolution Approach
FFT	Fast Fourier Transform
FIR	Finite Impulse Response
FWT	Fast Wavelet Transform

GCP	Ground Control Point
GLONASS	Russian GNSS
GNSS	Global Navigation Satellite Systems
GPS	Global Positioning System
Hz	Hertz
IIR	Infinite Impulse Response
INS	Inertial Measurement System
IMU	Inertial Measurement Unit
IRQ	Interrupt Request
KF	Kalman Filter
LAMBDA	Least-square AMBiguity Decorrelation Adjustment
LPF	Low Pass Filter
LS	Least Square
LSAT	Least Square Ambiguity search Technique
ML	Maximum Likelihood
OTF	On The Fly
PC	Personal Computer
P Code	Precise Code
PDOP	Position Dilution of Precision
PPS	Pulse Per Second (of the GPS receiver)
PSD	Power Spectral Density
QRS	Quartz Rate Sensors

RF	Radio Frequency
RMS	Root Mean Square
RPM	Rotation Per Minute
SD	Single Difference
sgn	signum
SNR	Signal to Noise Ratio
STD	Standard Deviation
SURE	Stein’s Unbiased Risk Estimate
VQR	Vibrating Quartz Accelerometers
UTM	Universal Transverse Mercator
VISAT	Video-Inertial-SATellite.

4. Symbols

a	ambiguity vector
b	baseline vector or filter coefficients
C	C/A code measurements
D	transformation matrix between single and double differences
dm	code multipath
δm	phase multipath
d_{ω}	gyro drift

δ_ω	quantization noise
f	frequency
H	transfer function or high-pass filter
h	filter coefficients
I	ionospheric delay
L	filter order, or low-pass filter
L_1	signal carrier L_1
L_2	signal carrier L_2
λ	carrier wavelength
M	wavelet scale
p	code measurements in general
P	P-code measurements
φ	carrier phase measurements or correlation function of filter input
s	scale factor between image and object coordinate frames
σ	standard deviation (usually empirical)
T	tropospheric delay
w	window function coefficients or wavelet coefficient of white noise
W	wavelet domain or wavelet transform
ω	angular frequency or angular velocity
ω_c	cut off frequency

CHAPTER 1

INTRODUCTION

1.1 Background

Increasing demand for up-to-date information in spatially referenced Geographic Information Systems (GIS) requires the development of fast, reliable and accurate acquisition systems. With advances in kinematic geodesy and the ready availability of digital imaging sensors, a considerable portion of GIS information can be acquired from moving platforms operating on land, water or in the air. While the progress in imaging sensors yields Earth scenes with better quality, the research in kinematic geodesy focuses on providing more accurate information about the origin of the imagery in space-time. The advances in both research areas work in a complementary fashion producing stream(s) of remotely sensed data which can be interpreted in a chosen mapping frame faster, more economically and with better accuracy.

Georeferencing can be defined as a process of obtaining knowledge about the origin of some event in space-time. Depending on the sensor type, this origin needs to be defined by a number of parameters such as time, position (location), attitude (orientation) and possibly

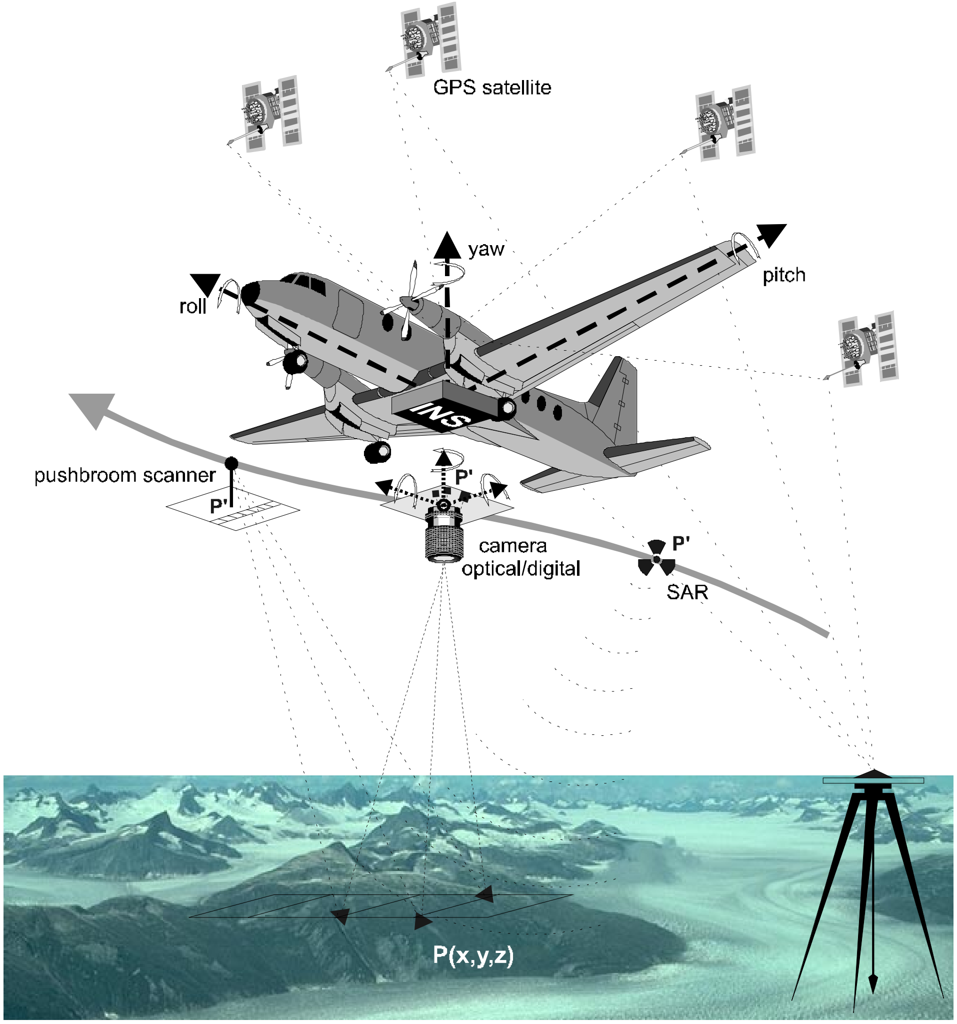

Figure 1.1. Direct georeferencing of airborne imaging data by INS/DGPS.

also the velocity of the object of interest. When this information is attained directly by means of measurements from sensors on-board the vehicle the term direct georeferencing is used. For an airborne mapping application this concept is schematically depicted in Figure 1.1. An aircraft carries a distinct set of sensors capturing patches of the Earth as well as navigation sensors collecting measurements needed for direct georeferencing. The latter information is in this case provided by integrated inertial and satellite technology comprised of an **I**nertial

Navigation **S**ystem (INS), receivers of the **G**lobal **P**ositioning **S**ystem (GPS), and a computer. The accuracy of the position and attitude components (together called the parameters of exterior orientation) required to fully utilize the resolution of current airborne imaging sensors are shown in Table 1.1. Since the airborne mapping industry is not large enough to drive the evolution of a dedicated INS/DGPS[1] system, the given specifications represent a challenge for the development of data processing algorithms which could possibly achieve these goals with the standard hardware currently available. As will be described later, the development and analysis of such data processing techniques is the main topic of this thesis.

Table 1.1 Georeferencing accuracy requirements for airborne survey systems. (Note: Simplified to one image-to-map scale, which may vary with applications).

Type of sensor	**Position**	**Orientation**
aerial camera, scale > 1:2000	0.05~0.1 m	15"~30"
aerial camera, scale < 1:5000	0.75~1 m	50"~60"
CCD camera or scanner (correlated with pixel size)	0.25~1.0 m	1′~3′
interferometric SAR	1 ~ 2 m	10"~40"

---

[1] DGPS is an acronym for differential GPS, a method of utilizing simultaneous observations between a pair of GPS receivers to perform relative positioning of high accuracy.

1.2 Evolution of Georeferencing

Traditionally, for the last few decades, the concept of image georeferencing has relied on the presence of ground control points in a project area. They are imaged together with other objects of interest. To reduce the amount of **g**round **c**ontrol **p**oints (GCP) necessary to orient every single frame-based image, a concept of overlapping images, called aero-triangulation, was introduced. Despite the reduction of the number of GCP's needed, the reliance on the GCP in classical aero-triangulation remained heavy, about one GCP for every five photos. The cost of performing aero-triangulation, including establishing ground control, is currently estimated to be $50 to $70 per stereo model, where an airborne survey company is processing about 5,000 to 10,000 stereo models per year.

The introduction of GPS technology in the late eighties (the system became fully operational in 1993) together with the advances in computational algorithms resulted in the development of DGPS-supported aero-triangulation. In this already well-established industry method the DGPS data provide partial knowledge about the origin of the image in space-time, particularly on its position. By coupling this information with the concept of overlapping imagery and at least three ground control points for each block of images, the remaining parameters of exterior orientation can be found and images can be georeferenced.

Although the introduction of DGPS to the georeferencing problem has not completely eliminated the need for ground control and overlapping imagery, it has pointed the way to the integration of DGPS and the already existing inertial technology. This idea has been strongly promoted at the University of Calgary in the eighties (Schwarz et al., 1984; Goldfarb, 1987), and results of several on-going projects were described already in the early nineties (Cannon, 1991; Schwarz et al., 1993). Parallel development then became noticeable at other institutions (Hein et al., 1988; Bossler et al., 1993). It was not till the second half of the nineties that the airborne mapping industry gave serious consideration to this technology and first results with commercially available systems appeared (Abdullah, 1997; Scherzinger, 1997). The possibility of measuring the instantaneous position, velocity and attitude of the on-board imagery sensor by an INS/DGPS system also widened the application field of non-frame-based imagery including pushbroom scanners or synthetic aperture radars (SAR).

The development of direct georeferencing by INS/DGPS systems also gave rise to land-vehicle based acquisition systems, since the requirements on the accuracy of the parameters of the exterior orientation can be somewhat relaxed in this case. The land-vehicle based acquisition systems are usually capable of delivering coordinates in object space with a typical absolute accuracy of 1-2 metres; see for instance Ash et al. (1994) or Bossler et al. (1993). More recently, an accuracy of 10-30 cm has been achieved with the VISAT system (El-Sheimy, 1996). However, the carriers which are in highest demand by industry for semiautomatic mapping are aircraft and helicopter. To design an airborne survey system with the accuracy of a few decimetres (see Table 1), the method of direct georeferencing needs further improvement.

1.3 Research Objectives

The main objective of this thesis is to improve the methods of INS/DGPS data processing in such a way that a significantly better estimate of the parameters needed for direct georeferencing can be achieved. The developed algorithms should be valid across the typical range of sensors used, and also possibly over the whole field of INS/DGPS operation. The main emphasis in the thesis will be given with respect to airborne carriers.

Since the starting point in these investigations will be an existing georeferencing methodology developed at The University of Calgary for land-based application (El-Sheimy, 1996), the primary goal of the thesis can also be formulated as 'optimizing georeferencing of airborne survey systems by INS/DGPS'. Considering this fact, further objectives can be specified as identifying the essential components in the error budget of the currently used method of INS/DGPS airborne georeferencing, and designing methods for their reduction. This requires that the following tasks are addressed:

1. Design filtering methods for reducing short-term noise in the inertial data, including short-term periodic, short-term correlated and wide-band noise in inertial data, and test them.
2. Investigate how the inclusion of inertial measurements improves the on-the-fly (OTF) ambiguity[2] determination.

---

[2] Initial uncertainty of integer number of cycles in the GPS carrier phase observations. This information is vital for accurate position determination.

3. Investigate operational procedures to eliminate or substantially reduce error sources of the integrated system.

The design of filtering methods to reduce short-term inertial noise will lead to a substantial improvement in the determination of attitude parameters, which greatly affects the accuracy of direct georeferencing and subsequently also airborne mapping. This fact is indicated in Figure 1.2, which compares achievable mapping accuracies between the traditional and the proposed approach of data processing as a function of the quality of the attitude parameters.

The investigations into the process of ambiguity determination will clarify the benefits between the possible methods of INS/DGPS integration (i.e. centralized versus de-centralized filtering), as well as evaluate the positioning contribution of inertial systems from

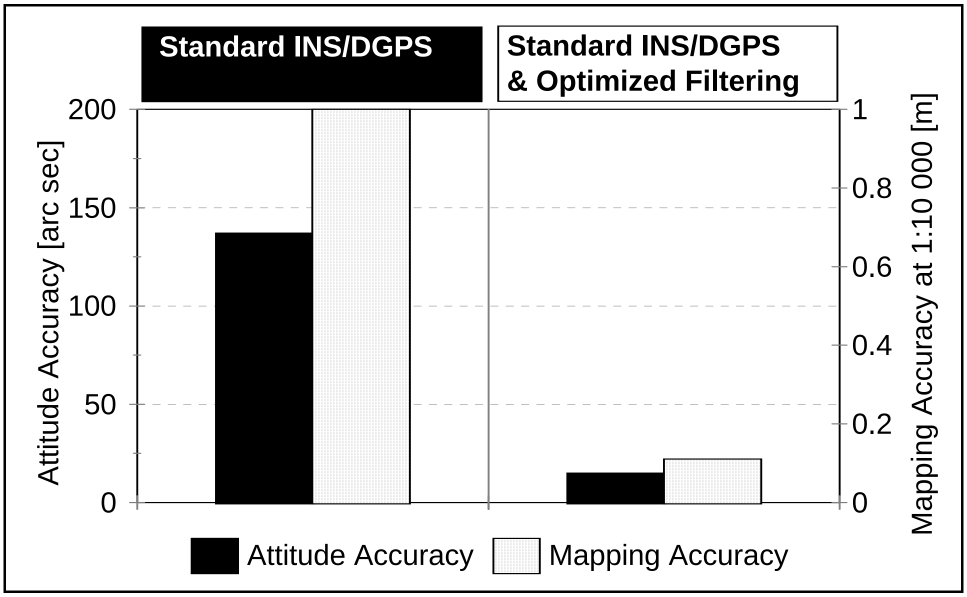

Figure 1.2. Accuracy gain through optimized filtering.

different accuracy classes. The latter will simplify decisions when making a choice of an INS for a specific application.

The analysis of operational procedures will specify the practical aspects of direct georeferencing which should be carefully considered when designing an airborne survey system.

1.4 Thesis Outline

Chapter 2 is an introductory chapter explaining the concept of direct georeferencing. It briefly discusses the underlying principle of extracting 3-D coordinates from imagery through the use of INS/DGPS data and provides an overview of the principles of navigation sensors used for determining the motion of a rigid body in space-time. It also outlines the limitation of the integrated INS/DGPS technology which serves as a starting point for the research.

Chapter 3 describes a design of time-invariant filters to reduce the amount of short-term noise present in the inertial signal prior to mechanization and further processing. Since these methods operate within the spectral band containing no signal but only noise, they are referred to as ‘out-of-band’ filtering techniques. Several methods are presented and compared including a spectral technique for dither spike removal and a class of low-pass Finite Impulse Response (FIR) filters.

Chapter 4 focuses on designing an ‘in-band’ filtering technique which reduces the amount of inertial noise within the band of interest, i.e. between the measurement period of external aiding with GPS and the edge of the motion band. A model for the short-term inertial errors is introduced in the frequency as well as the wavelet domains and a technique for adaptive estimation of the model parameters is described. The actual de-noising is performed in the wavelet domain based on the principle of shrinking the wavelet coefficients of the raw inertial signal. The method presented is then independently evaluated on different types of inertial data.

Chapter 5 studies the integer ambiguity estimation and validation problem when inertial data are available. Rather than drawing conclusions from an analysis of many data sets, the investigation aims at deriving results from knowing only the relative ratio of accuracies between the INS and GPS signals themselves. This is achieved by studying the intrinsic properties of the ambiguity search space which directly relate to the problem of ambiguity estimation and validation. The insight to this somewhat complex problem is gained by deriving an analytical expression to obtain the conditions under which the inertial data improve the ambiguity resolution process and by verifying them by computer simulations.

Chapter 6 presents other important topics which have to be considered when designing an airborne system for direct georeferencing. These topics include sensor placement, effect of vibrations, alignment of the inertial system, sensor synchronization and calibration. This chapter does not provide a detailed study, but rather points out some important practical considerations and some remaining problems whose solutions are suggested.

In Chapter 7, the whole concept of airborne georeferencing by INS/DGPS is tested. The flight scenario and the process of obtaining a reference trajectory is described and the results of direct georeferencing are presented. The purpose of this chapter is twofold. First, to describe in detail the origin of the reference values already used throughout the previous chapter, and second to provide indications of what can be expected once direct georeferencing becomes routinely used by the airborne mapping industry.

Chapter 8 draws conclusions from the research work conducted and also gives recommendations for future investigations.

Some of the material presented in Chapters 3, 4, 5 and also 7 has been either previously published or submitted for publishing. In those cases where the candidate has been either the author or the first co-author of these papers, quotations are not indicated as such, but the works is simply referenced.

CHAPTER 2

GEOREFERENCING BY INS/DGPS

This chapter describes the general concept of direct georeferencing by INS/DGPS, the properties of the individual sensors, and the methods used for combining their output into a multi-sensor system. Since most of the presented material has been described elsewhere, the chapter has the character of an overview.

2.1 The Concept of Georeferencing

To georeference frame-based imagery, the parameters of interior and exterior orientation have to be determined. The interior orientation parameters, i.e. coordinates of the principal point x_0, y_0, the focal length f, and the geometric distortion characteristics of the lens, can be measured in laboratory conditions. These parameters can be considered as more or less constant over a period of time. In contrast, the six parameters of camera exterior orientation (X_0, Y_0, Z_0, ω, φ, κ) are changing quickly and their evolvement has to be tracked by a real-time measurement process to achieve direct georeferencing. In principle, any navigation systems providing position and attitude information with sufficient accuracy can be used for this purpose, provided the following three conditions are met:

- the position and orientation offset between the frames of the navigation and imaging sensors can be determined with sufficient accuracy,
- this offset remains constant or its variations can be modeled,
- the sensors can be synchronized with sufficient accuracy to a common time base.

The term ‘sufficient accuracy’ used above means that the quality of the parameters of measured exterior orientation depends not only on the accuracy of the navigation system itself but also on the accuracy with which offsets and synchronization can be determined.

When the navigation information is provided by an integrated INS/DGPS system, the equation for direct georeferencing takes the form:

$$\boldsymbol{r}_{\boldsymbol{i}}^{\boldsymbol{m}} = \boldsymbol{r}_{\boldsymbol{ins/dgps}}^{\boldsymbol{m}}(t) + \boldsymbol{R}_{\boldsymbol{b}}^{\boldsymbol{m}}(t)\,[\,s_i\,\boldsymbol{R}_{\boldsymbol{c}}^{\boldsymbol{b}}\,\boldsymbol{r}_{\boldsymbol{i}}^{\boldsymbol{c}}(t) + \boldsymbol{a}^{\boldsymbol{b}}\,] \tag{2.1}$$

where

$\boldsymbol{r}^m{}_i$	is a vector of coordinates to be computed in the mapping frame for a specific point (*i*),
$\boldsymbol{r}^m{}_{ins/dgps}(t)$	is a vector containing the coordinates of the INS center in the mapping frame, determined by the INS/DGPS integration,
$\boldsymbol{R}_b{}^m(t)$	is the attitude matrix from the INS body frame to the mapping frame, determined by the INS/DGPS integration,

s_i	is a scale factor between the image and mapping coordinate frames for a specific point (*i*), usually determined by processing the captured imagery in stereo pairs,
$\boldsymbol{R}^b{}_c$	is the rotation matrix (orientation offset) between the camera frame and the INS body frame determined from calibration (see for instance Skaloud et al. (1994) for frame-base optical imagery, El-Sheimy (1996) for digital cameras and Cosandier et al. (1994) for pushbroom scanners),
$\boldsymbol{r}^c{}_i(t)$	is the vector of coordinates (i.e., x, y, -f) observed in the image frame for a specific image (*t*) and point (*i*),
$\boldsymbol{a}^b$	is the vector of the translation offset between the INS and the camera centre in the INS body frame determined by terrestrial measurements as part of the calibration process.

The relations between the components of Equation (2.1) are depicted in Figure 2.1. This formula expresses the fact that the processing chain contributing to the overall performance of an acquisition system is affected by the accuracy of the measured image data, the INS/DGPS position and attitude, the system calibration, the optical properties of the cameras and the effect of image geometry. A first-order error analysis can be developed by taking the partial derivative of Equation (2.1) with respect to each variable affected by a measurement error. The general structure of such an error model has been presented for instance by El-Sheimy and Schwarz (1994). However, detailed analytical studies are usually replaced with

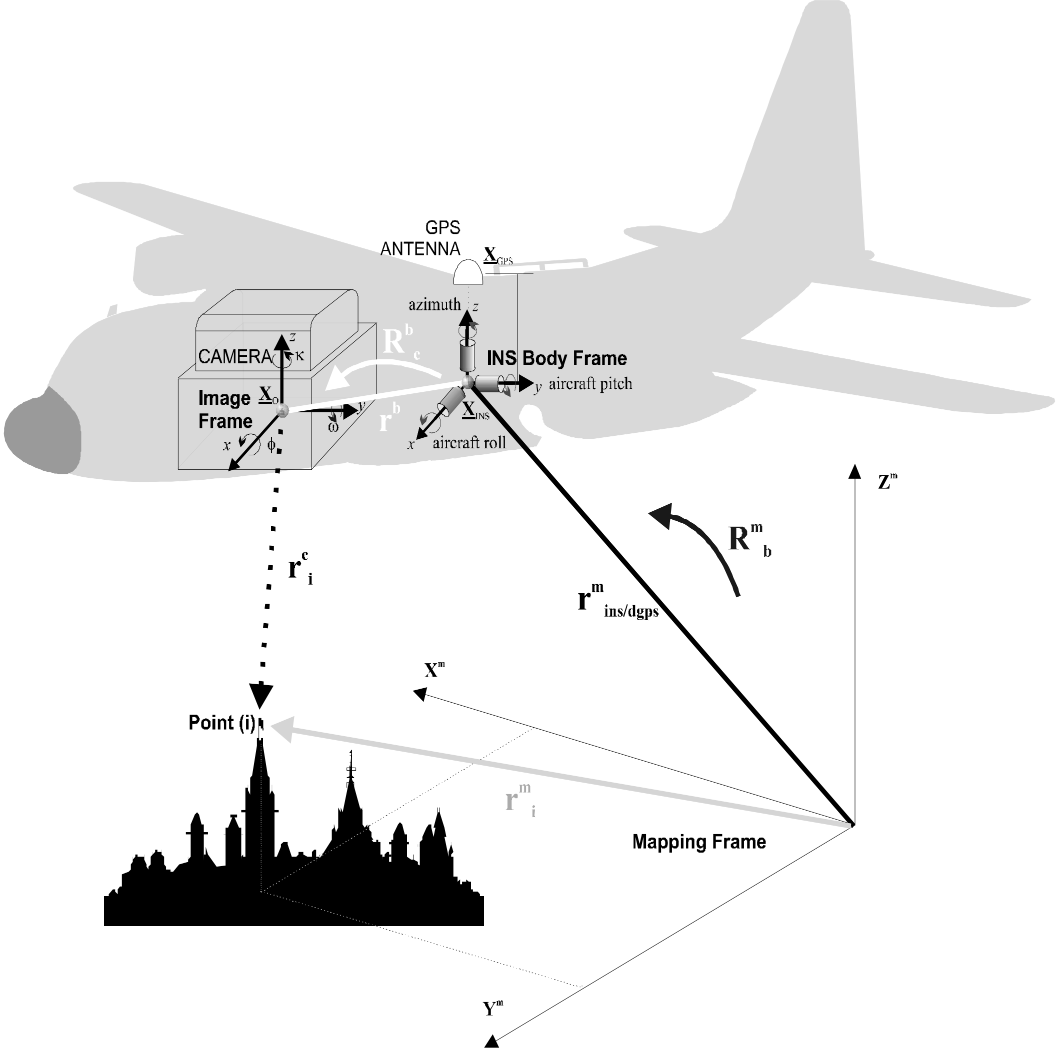

Figure 2.1. Elements of direct georeferencing.

computer simulations due to the functional complexity between the individual variables (Friess, 1986, Mostafa and Schwarz, 1998). The results show that although the structure of the error model remains the same, the significance of each error source is different from one application to the next. This can be intuitively explained as follows: For an airborne carrier, the objects of interest are, in general, further from the imaging sensors than for a land-vehicle carrier. Thus, airborne applications are more sensitive to errors in rotation. For instance, attitude errors of 1-3 arc minutes in the VISAT system introduce a positioning error of 1-2.5

cm at a distance of 30 metres from the cameras considering a perpendicular projection. The same attitude error at a flying height of 1240 metres would misplace an object on the ground by 1 metre. Thus, the same attitude error contributes only about 10% to the total error budget to the first application (El-Sheimy, 1996), while it may be as much as 60-80% in the second application (Skaloud and Schwarz, 1998).

2.2 The Positioning Sensors in Kinematic Geodesy

Considering again the formula of direct georeferencing (2.1), the positioning problem can be defined as observing the vector $\boldsymbol{r}^{m}_{ins/dgps}(t)$ with accuracies specified in Table 1.1 or better.

2.2.1 Main Concepts for $\boldsymbol{r}^{m}(t)$ Determination

Three main concepts for kinematic positioning have been successfully implemented. Ordered chronologically, these are inertial positioning, radio frequency (RF) ranging from ground beacons, and RF ranging from satellites. Their main characteristics are listed in Table 2.1.

Among the positioning concepts listed in Table 2.1, the accuracy superiority belongs to RF ranging from satellites. Although this technology has been devised for the purpose of

Table 2.1. Implemented concepts for kinematic positioning (Schwarz, 1998).

Concept	**Observable**	**A priori known**	**Type**	**Implementation**	
				Current Problems	Systems
Inertial positioning	Specific force Angular velocity	Initial position Earth rotation Gravity field	Global Autonomous Accuracy is time dependent	Error propagation	INS
Resection from known terrestrial points	Ranges (Ranges rates)	Station positions	Local Non-autonomous Low accuracy	Shading Synchronization	Loran-C Omega
Resection from satellites	Ranges (Range rates)	Satellite positions Earth rotation	Global Non-autonomous High accuracy	Target 'visibility'	GPS GLONASS

navigation with accuracy demands still below the positioning requirements of direct georeferencing, positioning uncertainties below 1 m can be achieved by this concept when used in a relative (differential) mode and when the standard range observables are augmented by the precise but ambiguous observations of the signal carrier phase.

Among the concepts listed in Table 2.1, inertial techniques are the only ones that are autonomous. Although their positioning performance degrades quickly with time, their short-term accuracy persists. This feature together with the high data rate makes an INS an ideal system to complement the RF ranging from satellites, such as GPS or GLONASS.

2.2.2 Positioning Methods

Although there are currently two operational Global Navigation Satellites Systems (GNSS), the present receiver technology is considerably more mature for GPS signals. This is especially true in the case of carrier phase observations, which are the vital part of information needed for high accuracy kinematic positioning. Therefore, the further discussion of RF technology using ranging from satellites will be limited to GPS signals.

Relative GPS positioning

A GPS receiver can be considered as an advanced interferometry recorder which performs basic observations by comparing the received signal with its replica generated by the receiver itself (correlation of the code modulation or comparison of the phase). Relative positioning with GPS is achieved by performing simultaneous observations of satellite signals at two (or more) sites (Counselman et al., 1981). When the position of one receiver is precisely known, the common error sources in the observations can be canceled or greatly suppressed by forming the *double differences* (DD) from the data among the satellites and receivers. This concept has been thoroughly analyzed in the literature (see for instance Kleusberg and Teunissen, 1996) and is often referred to as differential GPS or DGPS. The nonlinear observation equation for the difference between the simultaneous phase (Φ) and code (p) measurements between receivers m, n and satellites k, l reads

$$\begin{aligned} \Phi^{k,l}_{m,n}(t) &= \rho^{k,l}_{m,n} - I^{k,l}_{m,n} + T^{k,l}_{m,n} + \delta m^{k,l}_{m,n} + \lambda N^{k,l}_{m,n} + \varepsilon^{k,l}_{m,n} \\ p^{k,l}_{m,n}(t) &= \rho^{k,l}_{m,n} + I^{k,l}_{m,n} + T^{k,l}_{m,n} + dm^{k,l}_{m,n} + e^{k,l}_{m,n} \end{aligned} \tag{2.2}$$

where ρ denotes the true range corrupted by errors due to residual ionospheric (I) and tropospheric (T) delays, signal multipath ($\delta m,dm$) and noise (ε,e). Furthermore, the phase measurements on a carrier phase of wavelength λ are ambiguous by a number of N cycles. In the following, the indices m,n and k,l will be omitted for simplicity. When all residual error sources except the ambiguities are considered as stochastic variables, the linear form of the DGPS observation equation takes the form

$$\begin{aligned} D^T \Phi_{i,j} &= D^T A_i b_i + \lambda_j a_j \\ D^T p_{i,j} &= D^T A_i b_i \end{aligned} \tag{2.3}$$

where i=1,...,k denotes the epoch number and k equals the total number of epochs, j=1,2, vectors Φ_i and p_i contain the m (number of satellites) single difference (SD) carrier phase and code measurements, respectively, D^T is the $(m-1) \times m$ matrix transforming the SD to DD observables at epoch i, A_i represents the $m \times 3$ SD design matrix that captures the receiver to satellite geometry, b_i denotes the vector of three unknown increments in the baseline, λ_1 and λ_2 are the known wavelengths L_1 and L_2 of two signal carriers, and the vectors a_1 and a_2 contain the $(m-1)$ unknown DD ambiguities. The redundancy for the different measurement scenarios, considering two receivers, is given in Table 2.2 below. The coordinates of a kinematic position vector are usually first estimated together with the ambiguities by a least-squares approach implemented in the form of a Kalman filter, followed by a search for integer ambiguity values, and the subsequent correction to baseline coordinates, once the ambiguities are determined (for details, see Kleusberg and Teunissen, 1996).

Table 2.2. The observation redundancy for different DGPS scenarios, where *k* is the number of epochs and *m* is the number of satellites.

	Observation	**Unknowns**	**Redundancy**	**Note**
L1 + C1	2*k* (*m*-1)	3*k* + (*m*-1)	(2*k*-1) (*m*-1) - 3*k*	short baseline, iono delay neglected
L1&L2 + C1&P2	4*k* (*m*-1)	3*k* + (*m*-1)	(4*k*-1) (*m*-1) - 3*k*	short baseline, iono delay neglected
	4*k* (*m*-1)	3*k* +(*m*-1)(k+1)	(3*k*-1) (*m*-1) - 3*k*	long baseline, iono delay siginficant

Positioning with inertial navigation systems (INS)

An inertial measurement unit (IMU) contains a triad of accelerometers and gyroscopes measuring the vectors of specific force ($\boldsymbol{f}_i^b$) and angular velocity ($\boldsymbol{\Omega}_{ib}{}^b$), respectively, with respect to an inertial frame of reference. Together with the knowledge of the Earth rotation rate ($\boldsymbol{\Omega}_{ie}$) and the Earth gravity field ($\boldsymbol{g}$), an IMU provides sufficient information to solve for trajectory parameters in a first-order differential equation,

$$\begin{pmatrix} \dot{\boldsymbol{r}}^{m} \\ \dot{\boldsymbol{v}}^{m} \\ \dot{\boldsymbol{R}}_{b}^{m} \end{pmatrix} = \begin{pmatrix} \boldsymbol{D}^{-1}\boldsymbol{v}^{m} \\ \boldsymbol{R}_{b}^{m}\boldsymbol{f}_{b} - (2\boldsymbol{\Omega}_{ie}^{m} + \boldsymbol{\Omega}_{em}^{m})\boldsymbol{v}^{m} + \gamma^{m} \\ \boldsymbol{R}_{b}^{m}(\boldsymbol{\Omega}_{ib}^{b} - \boldsymbol{\Omega}_{im}^{b}) \end{pmatrix} \tag{2.4}$$

assuming the initial conditions are provided by other means (Britting, 1971). The IMU, the interface and a navigation processor for measurement mechanization including the initial alignment (leveling and gyrocompasing) form an INS. Traditionally, inertial systems have been divided into three groups according to the free-running growth of their position error (Greenspan, 1995):

- the *strategic-grade* instruments (performance ≈ 100 ft/h)
- the *navigation-grade* instruments (performance ≈ 1 nm/h)
- the *tactical-grade* instruments (performance ≈ 10-20 nm/h)

A further classification recognizes two main system groups: stabilized-platform systems and strapdown systems. The distinguishing factor in this case is the isolation of the sensor assembly from rotation movement. The current evolution of inertial technology leads towards strapdown systems of smaller volume, weight and power consumption.

2.2.3 Limitations of Positioning Methods

Relative GPS positioning

There are two types of problems in kinematic GPS positioning. The first has to do with the satellite configuration and observability (i.e. signal blockage, number of satellites in view, baseline to satellite geometry, etc.). The second stems from the accuracy of the observables. In precise positioning, the accurate but ambiguous phase measurements are of prime interest. When the ambiguities can be correctly determined, the residual error sources affecting the baseline accuracy are relatively small, at least for receiver separations of up to 100 km. Table 2.3 indicates that for a baseline length below 10 km, a relative accuracy of better than 10 ppm can often be achieved with good satellite constellation. However, if the ambiguities are

Table 2.3. Residual effects in kinematic relative positioning for baseline length ≈ 10 km (Tiberius, 1998).

	Troposphere (T)	**Ionosphere (I)**	**Multipath (δm)**	**Receiver noise (ε)**	**Orbital errors**
value [m]	10^{-2}-10^{-3}	10^{-2}-10^{-3}	10^{-2}	10^{-3}	10^{-2}

not correctly determined as integers,[1] the relative positioning accuracy is typically at the level of 100 ppm for baselines of this length. For longer baselines, precise post-mission satellite orbits should be used and atmospheric delays should be modeled and estimated. The tropospheric delays due to height differences should be modeled in all cases (for references, see Kleusberg and Teunissen, 1996)

Inertial techniques

The positioning accuracy of an inertial navigation system operated in unaided mode degrades quickly due to time dependent systematic errors. Due to this fact, even the most accurate INS's cannot serve as stand-alone systems for georeferencing applications. However, within a short period of time, during which the error growth can be considered approximately linear, a navigation-grade INS can deliver relative positioning accuracy of DGPS quality. This characteristic led to the idea of INS/DGPS integration which will be discussed later. The behavior of stand-alone inertial sensors is well described in the literature; see for instance Britting (1971) for platform inertial systems, or Savage (1978) for strapdown inertial systems.

---

[1] The problem of ambiguity estimation with inertial aiding is investigated in Chapter 5.

2.3 The Orientation Sensors in Kinematic Geodesy

Considering equation (2.1), the orientation problem can be defined as seeking the rotation matrix $\mathbf{R}_b^l(t)$ with ‘sufficient’ accuracy, where the meaning of the word sufficient varies according to application requirements. The parameters of the orientation matrix can be found by GPS or INS only, or via their integration. A number of technologies have been implemented around both concepts. The following sections give a brief overview.

2.3.1 Main Concepts for $R_b^l(t)$ Determination

Two fundamentally different concepts of determining rotation in space exist in the kinematic environment. They are:

Ranging from satellites to a multiple antenna array

By employing a configuration of several antennas (at least three) mounted on a common rigid platform, their position with respect to each other is accurately established using range differential techniques with carrier phase observations. The orientation parameters are then found by projecting vectors between the antennas on to the local-level frame (Cohen and Parkinson, 1992). Such a projection is possible, since the vectors are determined with respect to the Earth-fixed frame and the orientation of the local level frame is uniquely defined by its origin. The location of the origin (i.e. the position of one of the antennas) is also provided by satellite positioning.

Inertial techniques

A triad of gyroscopes contained in an INS measures directly the vector of angular velocities with respect to an inertial frame of reference. The parameters of $\boldsymbol{R}_b^l(t)$ in Equation (2.1) are then obtained by transforming the angular velocities to the local-level frame and integrating them (Britting, 1971).

The main characteristics of both successfully used concepts are listed in Table 2.4. Different implementations of these methods have given rise to a variety of technologies, an overview of which will be given in the following section.

Table 2.4 System concept for kinematic orientation (Schwarz, 1998).

Concept	**Observable**	**A priori known**	**Type**	**Implementation**	
				Current Problems	**Systems**
Ranging from satellites to multiple target array	Ranges (vectors between antennas)	Satellite positions Initial attitude of antenna array Earth rotation rate	Global Non-autonomous Medium accuracy	Stability of target array Reliability	GPS multi-antenna systems
Inertial techniques	Specific force Angular velocity	Initial position Initial attitude Earth rotation rate Gravity field	Global Autonomous Accuracy dependent on time	Gyro drifts	INS

2.3.2 Technology Profiles

An overview of existing technologies providing measurements necessary for $\boldsymbol{R}_b^l(t)$ determination is given in Figure 2.2. This figure shows a tree of technologies starting with the sensor principle on the left-hand side and then branching out to the actual implementations used in applications of direct georeferencing. Due to the higher noise level in the antenna arrays, the gyro-based technologies are currently more attractive for $\boldsymbol{R}_b^l(t)$

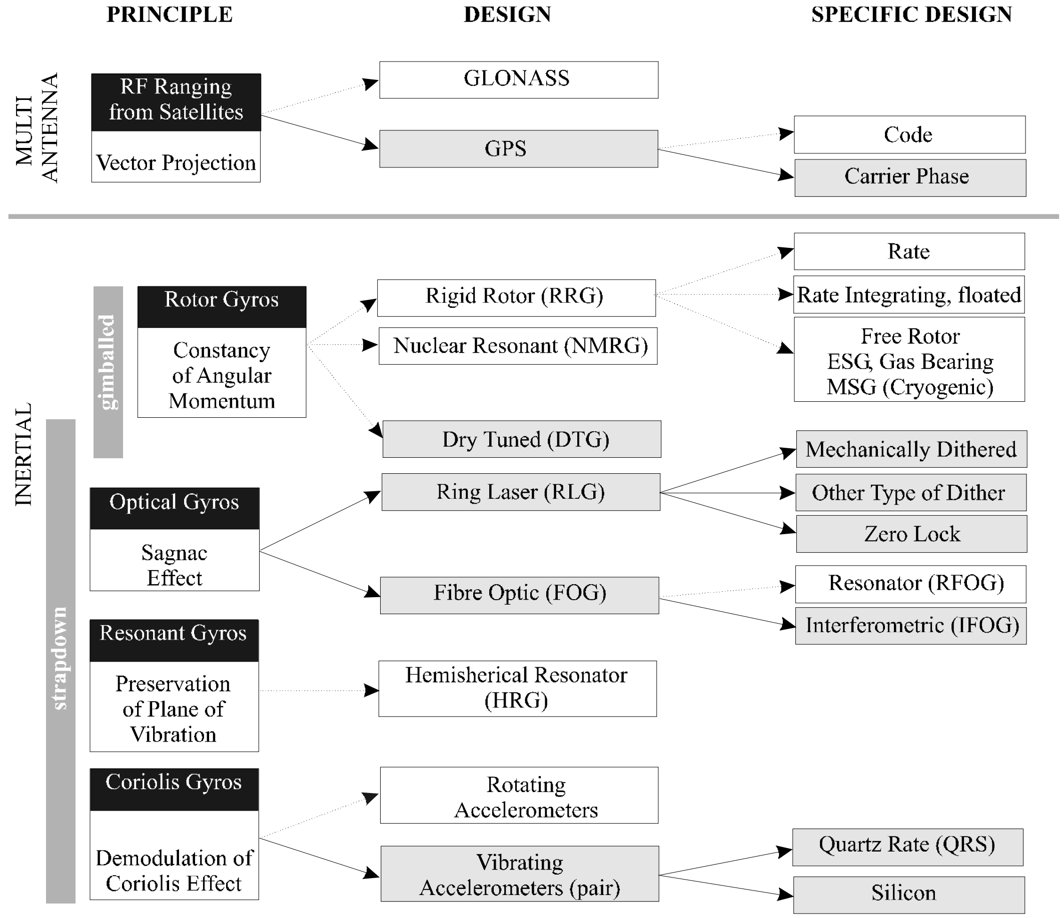

Figure 2.2. Satellite and inertial (gyro) technology for attitude determination. Grey boxes identify the technology to be most likely used in direct georeferencing (partially after Schwarz, in Krakiwsky et al., 1990).

determination in the airborne environment. Figure 2.2 distinguishes among several classes of gyro technologies ordered historically from the top to the bottom. Although the principle of **rotor gyros** is the oldest and still yields instruments of highest accuracy, these sensors are generally not suitable for direct georeferencing[2]. Their disadvantages include a complicated, expensive and bulky design, shorter life span and error behavior sensitive to acceleration. Currently, the most promising gyro technology in terms of cost versus performance is the **optical gyro** technology which has evolved into two main streams: the ring laser gyro (RLG) and fibre optic gyro (FOG). The basic principles inherent in these technologies will be introduced in following paragraphs. The **hemispherical resonant** gyro is generally very accurate but its performance is easily altered by vibrations. Therefore, these gyros are mainly used in space applications. The emerging technology of **Coriolis angular rate sensors** is very attractive because of its low cost and rugged design. When integrated with GPS, the best instruments of its kind can currently be used in georeferencing applications of low accuracy.

Currently, the most promising gyro technologies for direct georeferencing in the airborne environment are RLG and FOG. Both of these technologies are based on the inertia of the speed of light in vacuum, where the change in rotation is observed as a difference of transition time between two beams of light traveling along a closed-optical path in opposite directions. This principle is often referred to as the Sagnac effect. The conceptual difference between them is that the RLG is an active, closed-path oscillator while the FOG is a passive

---

[2] With an exception of DTG which has been used in georeferencing applications when implemented into lightweight strapdown IMU’s.

interferometer drawing its light energy from an external source. Their fundamental principles are summarized in the following.

Ring Laser Gyro (RLG)

The schematic description of the basic operating principles of an RLG are depicted in Figure 2.3. The RLG consists of a closed optical cavity which maintains two beams of coherent light generated by the lasing action of the Helium-Neon gas discharge. These beams travel in opposite directions along the same optical path directed by mirrors. Since the optical path is closed, the beams are also closing on themselves and an integer number of wavelength exists within the cavity. Rotating the block in one direction prolongs the optical path of one beam and shortens the path of the other. Because the speed of the light is not altered by motion and because the beams are closing on themselves, the change in the path length appears as a stretching or shortening of the wavelength, respectively. Letting a small amount of the light

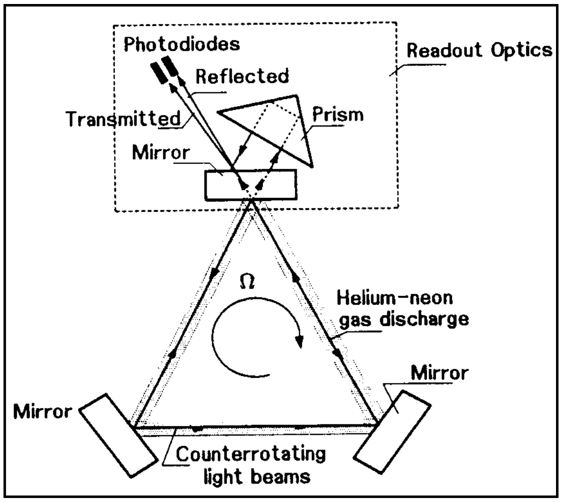

Figure 2.3 Schematic description of ring laser gyro (Merhav, 1996).

pass through one mirror and using a prism to reflect one beam to merge with the other will result in the summation of both beams. If there is a frequency shift between them (i.e. the beams have different wavelengths) their merging creates a fringe pattern. A change in rotation appears as a movement in the fringe pattern which can be detected by a photo diode. Two diodes are required to determine the direction of rotation. The output of the laser gyro is a pulse from the photo diode which is a measure of the angle through which the instrument has turned rather than a measure of the rotation rate as in the case of conventional mechanical gyros.

Fibre Optic Gyro (FOG)

The fiber optic realization of the Sagnac interferometer is depicted in Figure 2.4. A broadband light source (S) sends light through a coupler (C) where it is polarized, split, directed into the two ends of the fiber coil as clockwise (cw) and counter clockwise (ccw) beams and phase modulated (PM). On the return from the coil the beams first pass through the phase modulator and then are combined at the splitter. At this point, the counter rotating

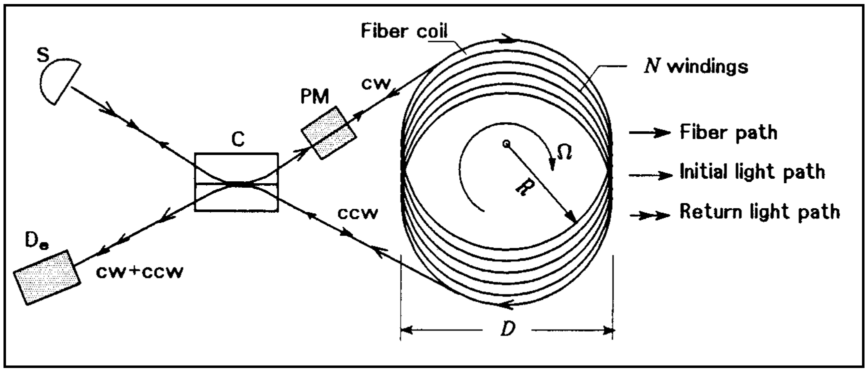

Figure 2.4 Schematic description of fiber optic gyro (Merhav, 1996).

beams are displaced in time with a phase shift proportional to the rotation rate. The combined beams travel to the photo detector (D) where they are converted into electrical power. The gyro output signal is the variation in the amount of power corresponding to the phase shift induced by the rotation rate.

2.3.3 Technology Limitations

Each method for orientation determination has its accuracy limitations. This section describes first the weaknesses of the main concepts in general, and then, in more detail, the limitation of optical gyros.

Ranging from satellites to multiple antenna array

The accuracy of GPS derived orientation parameters is limited by antenna separation, level of noise, signal multi-path and by relative motion between antennas (unmodeled wing flex, torsion in ship structure etc). The reported values in marine applications range from $1'$ to $3'$ (Lu, 1995) depending on actual vessel size and structure stability. The reported values in airborne applications are in the range of $6'$~$30'$(Cohen and Parkinson, 1992; El-Mowafy, 1994) and cannot compete with those derived from a strapdown INS/DGPS as will be discussed later. Furthermore, due to the limited data rate, the use of a GPS multi-antenna system is restricted to relatively low dynamic environments. Overall, the use of a GPS multi-antenna system does not meet in general the requirements for direct georeferencing in airborne applications (viz Table 1.1). Since this system does not experience drifts, an integration with a low-cost inertial system seems to be a promising approach (Zhang et al., 1995). However, the recent decrease in the price of high quality inertial hardware may make this alternative less appealing in comparison to a single antenna INS/DGPS system.

Strapdown inertial techniques

The attitude errors of a strapdown INS can be described as a combination of initial alignment errors, integrated gyro errors and deflections of the vertical (modeling errors in the gravity field). The well known analysis of misalignment errors shows a periodic, bounded influence on attitude determination, often referred to as Schuler oscillation (Britting, 1971). On the other hand, the problems associated with non-perfect output of a gyro vary according to the physical principle of angular rate observation and the quality of the sensor used. Generally, any type of gyro drift, as well as the random or weakly correlated errors in the gyro output, cause attitude divergence (Britting, 1971; Schwarz and Wei, 1995). The unbounded growth of this type of error can be dampened by integration with GPS position and velocity.

Optical gyros

Since the optical gyros are most likely to be used as primary orientation sensors for direct georeferencing in the near future, their properties are presented in more detail.

Generally, two main groups of gyro errors can be distinguished as shown in Table 2.5. The first group represents the limitations due to the physical principles employed while the other

Table 2.5 Error sources in optical gyroscopes.

<table>
<tr><th>FUNDAMENTAL</th><th colspan="2">TECHNICAL IMPERFECTIONS</th></tr>
<tr><td rowspan="3">wavelength of light source (resolution)
photon shot noise
polarization wander</td><td colspan="2">axis non-orthogonality
quantization noise</td></tr>
<tr><td>RLG</td><td>FOG</td></tr>
<tr><td>gain/losses in the laser cavity
optical seals leakage
thermal gradients
optical scatter -> lock in
lock in compensation</td><td>electrical & magnetic fields
index of refractions variations
power losses</td></tr>
</table>

is due to imperfections in the manufacturing process. The combined behavior of all error sources is usually rather complex and its characteristics are described by stochastic models (for an overview, see Erickson, 1993). The main features of the detailed stochastic models presented by Savage (1978) for RLG and by Bielas (1994) for FOG, can be expressed as follows:

$$d\boldsymbol{\omega}_{ib}^{b} = \boldsymbol{N}_{\omega}\boldsymbol{\omega}_{ib}^{b} + \boldsymbol{S}_{\omega}\boldsymbol{\omega}_{ib}^{b} + \boldsymbol{d}_{\omega} + \boldsymbol{\mu}_{\omega} + \boldsymbol{\delta}_{\omega} \tag{2.4}$$

where $\boldsymbol{\omega}_{ib}{}^{b}$ is the vector of angular velocities between the body frame and the inertial frame and $d\boldsymbol{\omega}_{ib}{}^{b}$ is its error, $\boldsymbol{N}_{\omega}$ is a skew-symmetric matrix describing the non-orthogonality of the axes defining the INS body frame, $\boldsymbol{S}_{\omega}$ is a diagonal matrix of scale factor errors, $\boldsymbol{d}_{\omega}$ denotes gyro drifts, $\boldsymbol{\delta}_{\omega}$ is noise due to quantization effects and $\boldsymbol{\mu}_{\omega}$ includes other type of gyro errors which are difficult to express analytically, e.g. random gyro drifts including correlated errors, random walk and white noise. The gyro bias and scale factors affect the angular determination systematically and are the main components influencing the orientation accuracy of a stand-alone INS. Typical performance ranges of the integrated errors for currently manufactured optical gyros are given in Table 2.6. As will be discussed later, the integration with GPS data reduces the long-term component of the error sources. The remaining error budget is then mainly affected by errors of short-term duration.

Table 2.6 Performance range for currently manufactured optical gyros (Greenspan, 1995).

	RLG	**FOG**
Bias (deg/h)	$10^{-4} \sim 10^{0}$	$10^{-3} \sim 10^{1}$
Scale factor (ppm)	$10^{-1} \sim 10^{1}$	$10^{0} \sim 10^{3}$

2.4 INS/DGPS Integration Approach and Its Limitations

As it has been pointed out in previous sections, both INS and DGPS are, in principle, capable of determining the position/attitude information needed for direct-georeferencing. Unfortunately, neither system can provide all trajectory parameters with an accuracy satisfying the requirements stated in Table 1.1. The main strengths and weaknesses of these technologies are summarized in the top part of Figure 2.5. As can be seen from this figure, the advantages of both systems are rather complementary and their combination yields a navigation system with the desired properties for georeferencing applications (Schwarz et al., 1993).

INS

- high position and velocity accuracy over the **short term**
- **accurate attitude information**
- accuracy decreasing with time
- **high measurement ouput rate**
- **autonomous**
- **no signal outages**
- affected by gravity

DGPS

- high position and velocity accuracy over the **long term**
- noisy attitude information (multiple antenna arrays)
- **uniform accuracy**, independent of time
- low measurement ouput rate
- non-autonomous
- cycle slip and loss of lock
- not sensitive to gravity

INS/DGPS

- **high position and velocity accuracy**
- **precise attitude determination**
- **high data rate**
- **navigational output during GPS signal outages**
- **cycle slip detection and correction**
- **gravity vector determination**

Figure 2.5. Benefits of INS/DGPS integration.

2.4.1 Integration Via Kalman Filtering

Merging INS and GPS data streams has been traditionally implemented via discrete-time optimal linear filtering and smoothing. The underlying theory is Kalman Filtering (KF), after Kalman (1960), and has been thoroughly described in the literature (Gelb, 1974; Maybeck

1979; Grewal and Andrews, 1993). Full scale examples of aiding an INS with position data provided by satellites have already been developed in the early seventies for the purpose of absolute positioning (D'Appolito and Roy, 1971). An extensive literature surrounds this topic (see for instance Farrell, 1976; Maybeck, 1979; Siouris, 1993). The relative positioning counterpart has been evolving since the early eighties (Wong and Schwarz, 1983). Both concepts follow the approach of estimating parameters of a dynamic error state model driven by white or shaped Gaussian noise.

The derivation of an error model to be used in the Kalman filter starts with the construction of a full-scale 'true-error' model, whose order is then reduced based on insight gained into the physics of the problem, covariance analysis, and simulations. Typically, the dynamic model is based upon an error model for the three position errors, three velocity errors, and three attitude errors in an INS (i.e the system error states), augmented by some dominant sensor errors (i.e. the sensor error states), such as accelerometer biases and gyro drifts. If properly done, such a minimal state vector reduces computational burden and accounts for the fact that many of the remaining INS error sources cannot be separated by the measurement information and are best expressed by lumped parameters in the state vector. Hence, models containing 15 to 21 state variables are often appropriate for a high quality strapdown INS. In the case of differential GPS, the sensor error states typically consist of the double differenced ambiguities while the systems states are the position and velocity errors.

Table 2.7. Different forms of Kalman filter implementation.

Implementation	**Advantages**	**Disadvantages**
Open loop	• KF may be run external to INS, suitable for platform INS • Used when only navigation solution from INS available	• Non-linear error model due to large second-order effect • Extended KF needed
Closed loop	• Inertial system errors, linear model is sufficient • Suitable for integration at software level	• More complex processing • Blunders in GPS may affect INS performance
Loosely-coupled (cascade, decentralized)	• Flexible, modular combination • Small KF, faster processing • Suitable for parallel processing	• Sub-optimal performance • Unrealistic covariance • Four satellites needed for a stable solution • INS data not used for ambiguity estimation
Tightly-coupled (centralized)	• One error state model • Optimal solution • GPS measurements can be used with less than 4 satellites • Direct INS aiding throughout GPS outages • Faster ambiguity estimation.	• Large size of error state model • More complex processing

The state vector estimation can be implemented in different ways. The main distinction is made according to the number of filters implemented (tightly or loosely coupled filtering), and whether the estimated sensor errors are fed back to correct the measurements (open or closed loop system). The merits and pitfalls of each concept are briefly summarized in Table 2.7. When properly designed, the closed-loop implementation generally has better performance and is therefore the preferred implementation when using a strapdown INS. The loosely-coupled filtering approach has been highly popular due its modularity and smaller filter size. It has been adopted for instance in the land vehicle based georeferencing application of VISAT (El-Sheimy, 1996) or current products of the Applanix Corporation (Scherzinger, 1997). Although the arguments for choosing either form of the implementation have been very balanced, the tightly-coupled approach is currently gaining more weight mainly due to the rapid increase in computational power. Moreover, some studies have shown that the effect of suboptimality in the decentralized filter architecture can be rather large in INS/GPS integration (Levy, 1996). Another strong argument favoring centralized filtering is its positive effect on the speed of the ambiguity determination; a topic to be closely investigated in Chapter 5.

2.4.2 Integration Limitations

The performance of an integrated INS/DGPS is a complex process depending on a variety of parameters including

- the quality and type of inertial sensors,
- the baseline length,
- operational aspects (e.g. the level of dynamics, sensor placement),
- the validity of error models,
- the estimation algorithm.

When data are collected, the mission parameters and the sensor quality can be considered as given. Therefore, the improvements in trajectory determination are usually sought in the development of better models and estimation algorithms. With the rapid increase of computational power, the trend of finding the most suitable error model for a specific system and specific conditions is being replaced by using a multi-model approach in conjunction with some type of adaptive estimation (Magill, 1965; Maybeck, 1982; Cher et al, 1997).

The other limiting factor of INS/DGPS integration is depicted in Figure 2.6. It shows two frequency bands, one in the lower frequencies where the INS/DGPS integration reduces the overall error, and another in the high frequencies, where the overall error is not reduced. Figure 2.6 shows clearly that the benefits of the integration are band-limited indeed. While the low frequency border of the INS/DGPS error spectrum is mainly determined by the biases in the DGPS observations (e.g., residual atmospheric errors, ambiguity uncertainities, etc.), the upper border is mainly influenced by short-term inertial errors. The limited ability of using DGPS data to reduce the short-term inertial errors is a direct consequence of the

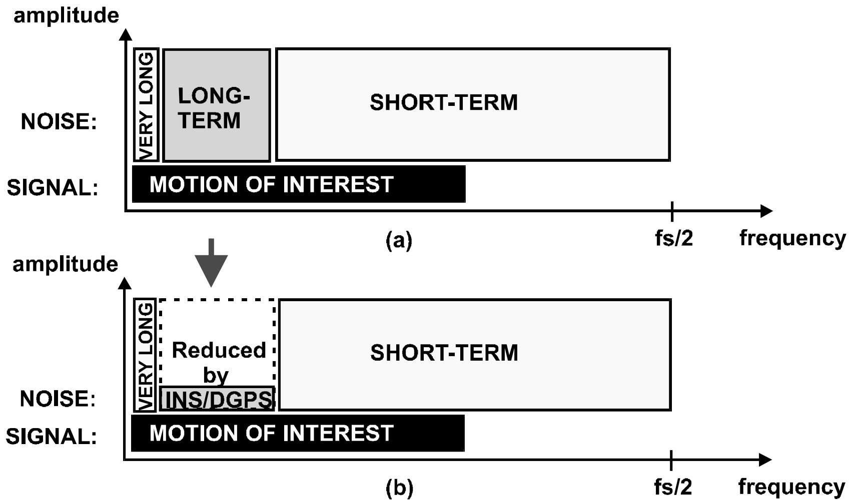

Figure 2.6. Schematic plot of inertial signal in frequency domain: (a) Before filtering, (b) After integration with DGPS observations. Note: Figure is not to scale, *fs* denotes sampling frequency.

sampling theorem. Due to the much lower sampling rate in GPS measurements, the quickly changing errors in the inertial output can be detected by the integration filter only as aliased frequencies after accumulating to a certain magnitude (amplitude). While the threshold of detecting these errors is mainly affected by the accuracy of DGPS ranging, their periodicity is a function of time over which the DGPS measurements can be considered reasonably uncorrelated. In other words, although some GPS receivers can provide measurement rates as high as 10 Hz, the noise on these observables can be considered ‘reasonably’ random only after a much longer period. The prevailing error sources contributing to the short-term inertial error spectrum include errors in quantization, intermittent drifts, errors from dithering motion compensation (for dithered RLG), scale factor errors and correlated noise due to vehicle vibrations.

It should be noted, however, that the long-term inertial errors which are reduced by the integration with DGPS data are usually much larger than the short-term noise. The individual error sources belonging to this category would include the main components of the gyro drift, accelerometer bias, scale factors and errors due to the non-perfect initialization (misalignment errors). The behavior of these errors is typically modeled in the integration process by several state-vector variables. Hence, after a sufficiently long observation period, these errors can be determined within a limit defined by the accuracy of the external aiding. Among other factors, the accuracy of the estimation process strongly depends on the vehicle dynamics, i.e. high vehicle dynamics will usually result in better estimation of the low frequency errors.

Rather than contributing to the optimality of the long-term error estimation, the research presented in the thesis focuses on reducing the error sources over the bandwidth which is not affected by the integration process. It will be shown that minimizing the level of short-term noise in inertial sensors is of great importance, especially for direct georeferencing applications.

CHAPTER 3

BAND LIMITING THE INS SIGNAL

This chapter focuses on designing time invariant filters to effectively band-limit the INS signal prior to its mechanization and further processing. The motivation behind this concept is schematically depicted in Figure 3.1. It shows that band-limiting the inertial signal down to the motion of interest eliminates a considerable portion of the short-term noise. An important assumption made here is that the actual output of the INS is well over-sampled. Considering the rather modest dynamics of surveying applications, such an assumption is reasonable because the sampling rate of the inertial sensors usually exceeds the frequency content of the motion by 10-50 times depending on the system. Since the motion is located in the lower part of the signal spectra the band-limiting corresponds to low-pass filtering. Before addressing the concept of low-pass filtering, the chapter presents a special filtering

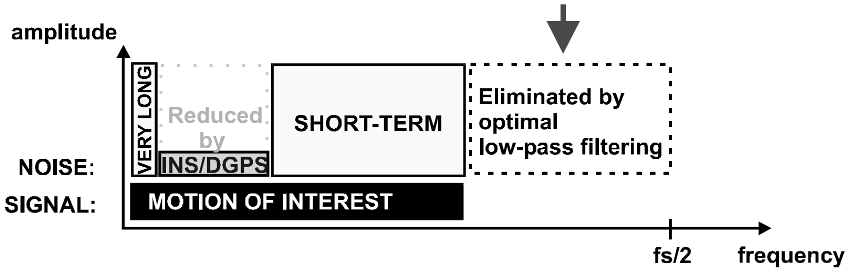

Figure 3.1. Effect of band-limiting on the INS/DGPS spectrum.
Note: Figure is not to scale.

technique developed for strapdown inertial systems with dithered gyros. A substantial part of the material presented in this chapter follows Skaloud and Schwarz (1998).

3.1 Dither Spike Removal

Most of the currently manufactured ring-laser gyros undergo a dithering motion. This motion is usually referred to as ‘gyro dither’ and causes vibrations of the whole sensor block. Although dither stabilizes ring-laser gyro output in the long run, it also adds high frequency noise of relatively large amplitude to its output. Manufacturres usually implement ‘dither-stripping’ methods into their data sampling. These methods are designed to remove the effect of dithering from the data. The dither is usually applied in a frequency range of 400-900 Hz. Since most data acquisition systems operate at much lower sampling rates, the remaining

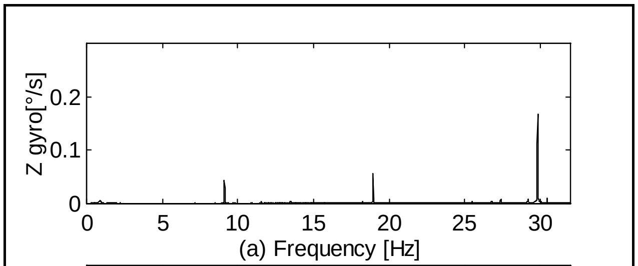

(a) Frequency [Hz]

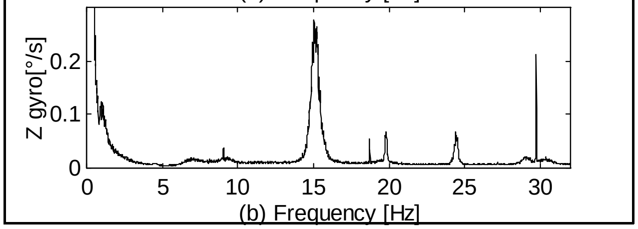

(b) Frequency [Hz]

Figure 3.2. Amplitude spectrum of raw INS signal in (a) lab conditions, (b) flight conditions.

dither frequencies are aliased into the low frequency spectrum limited by the Nyquist frequency. Figure 3.2 shows the amplitude spectrum of the Z-gyro output, sampled at a rate of 64 Hz, in laboratory and flight conditions. Since the laboratory environment is free of vibration, the peaks in Figure 3.2(a) at about 9, 20 and 30 Hz correspond to the 3 aliased dither frequencies. They have a maximum amplitude of 0.2° (~720"). Note that these are the amplitudes after the 'dither-striping' methods have been applied. These peaks are also present in the airborne environment, although other high frequency signals, due to vibrations, can be seen (Figure 3.2b), most prominently the one at 16 Hz which is due to the frequency of propellers running at 1000 RPM.

Czompo (1990) suggested a special frequency filtering method which detects aliased dither spikes in the inertial raw data and reduces their amplitude to the surrounding noise level. Such a gentle intervention into the spectrum does not change the phase and affects the mean only slightly. It changes the probability distribution of the static data from bimodal to unimodal. In other words, after the filtering, the properties of the sensor noise are closer to the white noise model assumed in the Kalman Filter used for INS/DGPS integration. The filtering procedure can be described by the following three steps:

Time to frequency domain conversion: Each channel of raw inertial data is divided into time slices of a certain length. The length should be chosen such that a detailed spectrum can be obtained and the Fast Fourier Transform (FFT) can be applied. In our case, subsets of 8192 points were used, which corresponds to 128 seconds of data considering the 64 Hz sampling rate. Then, the data are transformed by FFT to the amplitude and phase spectra for each sensor. The phase spectrum remains unchanged while the dither spikes in the amplitude spectrum will be reduced in the following step.

Dither spike removal: Due to the aliasing, the dither appears in the amplitude spectrum not as one but as several spikes at different frequencies. The program detects these spikes in predefined windows whose locations are known from the static data analysis. The use of non-overlapping windows is convenient since the frequencies where spikes appear can slightly vary for each data slice, but such variation is small enough to allow construction of well separated frequency windows. Practically, the reduction is performed by first computing the average amplitude (m) and standard deviation (σ) excluding the 10% of data with the highest amplitudes. The amplitudes higher than $(m + 3\sigma)$ are then reduced to m.

Frequency to time domain conversion: After the dither spikes have been removed from the amplitude spectrum, this spectrum and the original unchanged phase spectrum are converted back to the complex spectrum. Then, the inverse FFT is applied to obtain the data in the time domain. The new data with removed dither frequencies are stored and the whole procedure is repeated for the following data subsets.

Czompo (1990) tested such filtering on the INS and INS/DGPS derived positions of a land-vehicle and reported 5-15% accuracy improvement. The reference was provided by means of pre-surveyed control points along its trajectory. Section 3.3 analyses this method for attitude determination in the airborne environment with respect to a ‘true’ reference provided externally by photogrammetry. Before these results are shown, a low-pass filter will be discussed as an alternative to spike removal and noise reduction pre-processing.

3.2 Low Pass Filtering

This section describes the design of low pass filters which are most suitable for the preprocessing of inertial raw data. From a broad class of low pass filters, a sub-class of filters will be selected which reduce the short-term noise in the gyro output while not altering the underlying signal. Restating this objective in ‘filtering language’, we can say that the designed filter should strongly attenuate all frequency components which are not due to vehicle motion while not introducing any changes to the frequency band of interest as schematically shown in Figure 3.1.

The classification of digital filters is usually divided into two major subclasses: recursive, Infinite Impulse Response (IIR) filters, and non-recursive, Finite Impulse Response (FIR) filters. The main difference is that the coefficients of FIR filters operate only on the input data while the IIR filters are also feeding back their own output. As will be explained in the next section, only FIR filters can fulfil the design requirements needed for achieving the best possible results. The input-output relation of an FIR filter can be expressed by the following equation:

$$y_k = \sum_{n=0}^{L} b_n x_{k-n} \tag{3.1}$$

where x_k, y_k denote the filter input and output data and $b_{n=0,\ldots,L}$ are the filter coefficients.

3.2.1 Low Pass Filter Design Constraints

Two constraints will be imposed upon the design methods. The first is that of realizability, or causality. This condition implies that the impulse response, which is by definition the system response to a unit sample input at time $k = 0$, is equal to zero for $k < 0$. Note that this condition is satisfied by the form of Equation 3.1.

The second restriction is that the filter output can have only a linearly distorted phase. The precise determination of rotation angles is very sensitive to any phase distortion below the cut-off frequency. Since it is impossible to design a filter which would have a zero-phase response and at the same time not violate the causality condition, the generated phase distortion must be such that it can be eliminated later on. Since an FIR filter is a linear operation on the data, the desired zero phase response can be achieved by applying the same filter again, but in the reverse direction. Hence, the output of the forward/backward filter leaves the phase of the original data unchanged. Since the linear phase shift corresponds directly to a filter delay, the same effect can also be achieved by delaying the output of a filter by half of the filter order (Oppenheim and Schafer, 1989).

Linear-phase design is not possible in the case of IIR filters. The linear phase response in terms of transfer function implies that $H(z) = H(z^{-1})$. In a causal IIR filter design, perfectly linear phase response is not achievable since the resulting filter would have poles outside the unit circle and would therefore be unstable (Oppenheim and Schafer, 1989). For more details, see the extensive literature on this topic. An example of the negative effect of an IIR filter for attitude determination will be shown later in Section 3.3.

Since all FIR filters are stable by definition, zeros outside the unit circle are of no concern in this case and the condition $H(z) = H(z^{-1})$ can be satisfied by requiring zeros to exist in mirror-image pairs inside and outside the unit circle, e.g. at z_1, $1/z_1$ (Rabiner and Gold, 1975). Expressing this condition in the time domain requires the FIR filter coefficients to be symmetric such that

$$b_n = b_{L-n} \,, \qquad 0 \leq \text{integer}\left(\frac{L}{2}\right) \tag{3.2}$$

If L is even, the total number of coefficients is by definition $L+1$. In this case, there is a central sample $b_{L/2}$ about which the coefficients are symmetric. The condition imposed by Equation (3.2) results in a fixed delay of $L/2$ samples and the corresponding phase response is given by $\theta(\omega) = -\omega(L/2)$, where ω is the normalized frequency in radians. This phase response varies linearly with respect to the frequency.

3.2.2 FIR Design Via the Ideal Low Pass Filter

This section describes the principle of FIR coefficient derivation by formulating an 'ideal' filter response in the frequency domain and then obtaining its time-domain counterpart by a Fourier transform. Restating again the objective, a filter will be designed with a maximum magnitude response of one in the passband and zero elsewhere, and with a phase response which is a linear function of frequency. This can be expressed in terms of the Fourier transform as

$$H_d(e^{j\omega}) = \begin{cases} e^{-j\omega L/2} & 0 < |\,\omega\,| < \omega_c \\ 0 & \omega_c < |\,\omega\,| < \pi \end{cases} \tag{3.3}$$

where H_d is the Fourier transform of the filter coefficients h_d, $\omega_c = 2\pi f_c T$ defines the normalized filter cutoff frequency in radians and corresponds to the delay required to satisfy the causality constraint. The ideal impulse response $h_d(n)$ may be derived by evaluating the inverse Fourier transform of Equation (3.3) which yields:

$$h_d(n) = \frac{\sin[\,\omega_c(n - L/2\,)]}{\pi(\,n - L/2\,)} \tag{3.4}$$

Since the function in Equation (3.4) is symmetrical about L/2, the condition of symmetry is satisfied and linear phase response is achieved.

As defined in Equation (3.4), the impulse response is an infinitely long sequence which has to be truncated in the actual filter implementation as $h_d(n) = 0$ for $n > L$. The truncation results in an oscillatory effect, known as the Gibbs phenomenon, whose magnitude is relatively constant regardless of the filter length (Oppenheim and Schafer, 1989). In addition to the choice of the cut-off frequency ω_c, the designer has also to choose the filter order (L). Increasing the length of an FIR filter designed via Equations (3.3) and (3.4) has four effects, not all of them positive. It

a) reduces the width of the transition bandwidth,

b) increases the frequency of the oscillatory response (Gibbs phenomenon),

c) increases the filter delay,

d) increases the computational burden.

From the point of view of post-mission processing, the effects (c) and (d) are not important since all ‘future’ data are available in post-mission surveying applications and real-time computation is usually not required. The effect (a) is positive for our purpose because less of the undesired signal leaks into the pass band. Thus, the only problem remaining is the Gibbs phenomenon. Since this undesirable response results from the abrupt truncation of the infinite series, different approaches can be taken to alleviate this problem. A few of them are described in the following sections.

3.2.3 Time Domain Window Functions

The simplest approach to dampen the oscillatory effect is to perform a somewhat smoother truncation of the infinite series of filter coefficients. Such a smoothing can be achieved by multiplying the filter coefficients with a window function. This section discusses the properties of window functions commonly used in FIR filter design. The filters resulting from these functions will be tested in Section (3.3) on two sets of inertial data.

The abrupt truncation of an infinite sequence can be expressed as a product of two sequences

$$h(n) = h_d(n)\, w_R(n) \tag{3.5}$$

where $h_d(n)$ are the original filter coefficients derived by Equation (3.3) and $w_R(n)$ is the rectangular window function

$$w_R(n) = \begin{cases} 1 & 0 \le n \le L \\ 0 & \text{elsewhere} \end{cases} \tag{3.6}$$

As has already been mentioned, an improvement in the magnitude response can be expected by using a non-rectangular window with tapered ends. To retain the linear phase characteristics, such a window must also be symmetric about its midpoint. The amplitude spectrum of a desirable window has two key characteristics: a narrow main lobe which results in a smaller transition band; and side lobes that rapidly decrease in energy for

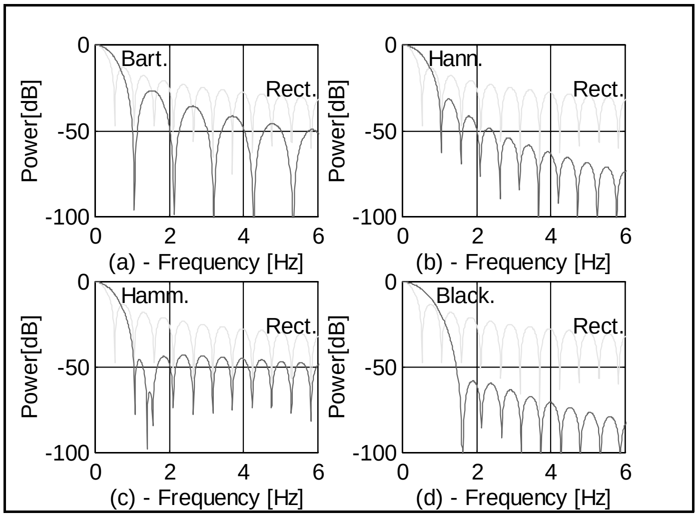

Figure 3.3. Frequency domain characteristics of (a)-Barlett, (b)-Hanning, (c)-Hamming, (d)-Blackman data windows plotted together with the rectangular window for a sampling rate of 64 Hz.

increasing ω, since this results in less oscillatory effect in both the pass-band and the stop-band of the filter.

Figure 3.3 shows the frequency domain characteristics of four of the most commonly used window functions: Bartlett, Hamming, Hanning and Blackman. The formulas for their derivation can be found in the signal processing literature, e.g. Oppenheim and Schafer (1989), and are therefore not shown here. From Figure 3.3 it is apparent that the penalty to be paid for achieving low side lobe levels is the increase of the main-lobe width. It should be noted that the trade-off between main lobe width and side lobe magnitude can be specified when using a Kaiser window (Kaiser, 1974). Thus, rather than having only a few window choices, the designer can tailor parameters of the Kaiser window according to the application needs. The Kaiser window is defined as

$$w_K(n) = \begin{cases} \dfrac{I_o[\beta\sqrt{(1 - [(n-\alpha)/\alpha]^2)}]}{I_o(\beta)} & 0 \le n \le L \\ 0 & \text{elsewhere} \end{cases} \tag{3.7}$$

where $\alpha = L/2$, and $I_o(\cdot)$ represents the zero-order modified Bessel function of the first kind. The Kaiser window has two parameters: the length $(L+1)$ and a shape parameter β. By varying $(L+1)$ and β, the window shape can be adjusted to trade side-lobe amplitude for main-lobe width. Table 3.1 specifies values of β and $(L+1)$ for which the Kaiser window gets the shape of the previously mentioned common window functions. Which of these trade-offs is better for lowpass filtering of the inertial data will be further discussed in Section 3.3.

Table 3.1. Commonly used window functions and equivalent Kaiser window parameters.

Equivalent Kaiser Window	**Rectangular**	**Bartlett**	**Hanning**	**Hamming**	**Blackman**
β	0	1.33	3.86	4.86	7.04
Transition Width	$1.81\pi/L$	$2.37\pi/L$	$5.01\pi/L$	$6.27\pi/L$	$9.19\pi/L$

3.2.4 Optimal FIR Low Pass Filter Design

Although the design of a low pass FIR filter by means of a window function is a very straightforward and powerful approach, this method is sub-optimal in the sense that it is possible to design a lower order FIR filter that has equally good frequency response characteristics. To design an optimal FIR filter requires the definition of an approximation criterion and the derivation of an algorithm which would satisfy such a requirement. The definition of a particular approximation criterion is twofold: the choice of an error measure to be minimized (e.g. maximum absolute error, sum of square errors, etc.) and the choice of a weighting function setting the relative size of the error in different bands.

It is obvious that the choice of the approximation criterion varies according to specific application requirements. In the case of raw inertial data, one is concerned about any changes to the passband. Attenuation variation in the stop-band is not so critical since this part of the spectrum contains a relatively small part of the total signal power.

The two most popular optimal design techniques will be further tested on actual data, because each has a different error measure. The first is based on minimizing the maximum absolute weighted error between the desired and the approximated filter response and is formulated as a Chebyshev approximation problem. A number of rather complex techniques have been devised for obtaining the solution of this problem (Parks and McClellan, 1972). An iteration technique known as the Remez exchange algorithm is used in the following. It has been described in Parks and McClellan (1972b), and has been used for a geodetic application in Hammada (1996).

The other optimal filter tested in the following can be derived by minimizing an error objective function that reflects the weighted mean-square difference between the ideal amplitude response and the amplitude response of the filter. The symmetrical impulse response (*w(n)=w(L-1-n)*) is then obtained in the least-squares sense from a system of linear equations $\boldsymbol{R}\,\boldsymbol{w} = \boldsymbol{p}$. The solution of the linear equations can be rewritten in matrix form as

$$\boldsymbol{w} = \begin{bmatrix} \Phi_{xx}(0) & \cdots & \Phi_{xx}(L) \\ \vdots & & \vdots \\ \Phi_{xx}(L) & \cdots & \Phi_{xx}(0) \end{bmatrix}^{-1} \begin{bmatrix} \Phi_{dx}(0) \\ \vdots \\ \Phi_{dx}(L) \end{bmatrix} \tag{3.8}$$

where $\Phi_{xx}(t)$ and $\Phi_{dx}(t)$ are the correlation and cross-correlation functions of the filter input sequence $\mathrm{x}(t) = \sum_{n=1}^{N} c_n \sin(2\pi f_n t)$ and the desired filter output $d(t) = \sum_{l=1}^{N} a_l c_l \sin(2\pi f_l t + \theta_l)$, respectively. For discrete time intervals, $\Phi_{xx}(t)$ and $\Phi_{dx}(t)$ can be expressed as

$$\begin{aligned} \Phi_{xx}(kT) &= \sum_{n=1}^{N} c_n^2 \cos(2\pi f_n kT) \\ \Phi_{dx}(kT) &= \sum_{n=1}^{N} a_n^2 c_n^2 \cos(2\pi f_n kT + \theta_n) \end{aligned} \tag{3.9}$$

where coefficients a_n and θ_n denote the design response magnitude and phase shift at frequency f_n, respectively, T is the sampling interval and c_n are frequency domain weights that can be used to emphasize certain frequencies over others.

When filtering raw inertial data, amplitude distortion introduced by the filter to the motion bandwidth is a concern. Therefore, the tested least-squares FIR filter was designed with heavy weights in the passband to obtain an almost flat response from zero to the cut-off frequency.

3.3 Analysis of Filter Performance

The performance of the band-limiting methods presented in Sections 3.1 and 3.2 will be evaluated and analyzed under flight conditions in two separate tests.

3.3.1 Attitude Determination

This test analyzes the merits of data prefiltering in attitude determination. For airborne application of direct-georeferencing, this is the vital parameter set to be improved. The external reference was obtained by means of a large scale photogrammetry test, which is described in detail in Chapter 7. The reference attitude at flying altitude was derived from the given control on the ground. The performance of individual filtering methods will be evaluated by the following statistical parameters computed from the disagreement of the azimuthal reference at 75 exposure stations spread over 40 minutes of flight: Mean (*m* =

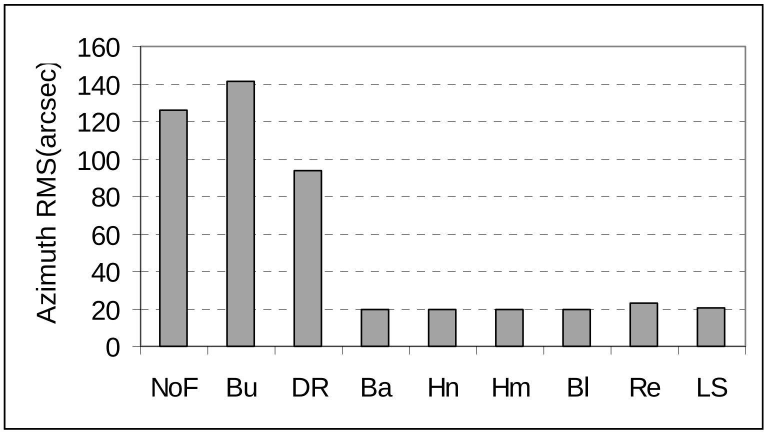

Figure 3.4. Comparison of pre-filtering methods for azimuth determination by INS/DGPS in the airborne environment.

$\Sigma x/n$), Standard Deviation ($STD = \sigma = [\Sigma(x-m)^2/(n-1)]^{1/2}$), Root Mean Square ($RMS = [\sigma^2+m^2]^{1/2}$) and Maximal Deviation from the mean (*MaxDev*). The graphical representation of the RMS values is shown in Figure 3.4. The legend defining the abbreviations for the filter types in this Figure can be found in Table 3.2. Table 3.2 also shows other statistical characteristics and filter design parameters. A detailed comparison of each reference point will be given later in Chapter 7.

Table 3.2. Comparison of filtering methods for azimuth determination by INS/DGPS in the airborne environment. The shown values are computed from a comparison with photogrammetry-derived attitude using 75 points over a 50 minute period.

	Abrev.	**STD** [deg]	**Mean** [deg]	**MaxDev** [deg]	**Filter Order** [# coef]	**Cut-off** [Hz]
No Prefiltering	NoF	0.025	0.025	-0.044	NA	NA
Butterworth	Bu	0.038	0.010	0.166	9	8
Dither Removal	DR	0.021	0.014	0.031	NA	NA
Bartlett	Ba	0.005	0.001	0.013	120	8
Hanning	Hn	0.005	0.001	0.013	120	8
Hamming	Hm	0.005	0.001	0.012	120	8
Blackman	Bl	0.005	0.001	0.012	120	8
Remez	Re	0.006	0.002	-0.010	120	8
LS	LS	0.005	0.001	0.013	120	8

The first bar in Figure 3.4 and the first row in Table 3.2 characterize the accuracy of the azimuth determination by INS/DGPS integration without INS data prefiltering. They are the result of comparing flight data and reference at 75 control points over 40 minutes of flight time. When considering the requirements of the most demanding airborne application (viz Table 1.1), the residual azimuth errors without prefiltering are still too large.

As can be seen from Figure 3.4 and Table 3.2, the comparison of the different low-pass filters shows a rather consistent performance with slightly worse RMS performance of the Remez filter. However, this difference is small and could be possibly caused by the type of ‘RMS’ evaluation which obviously favors the square error minimization. The Remez-exchange algorithm is designed to minimize the maximum absolute error and in this respect delivers the best results. The RMS value computed from the comparison to the reference is 0.005° (19"), which is overall five times better than the INS/DGPS integration without inertial data prefiltering and seven times better than the Butterworth filter which is often applied in commercial designs. Moreover, for all practical purposes the distribution of the residuals has zero mean which indicates that no distortion has been introduced to the passband by the prefiltering process.

Referring again to the statistical comparison in Table 3.2, the dither removal method did only marginally improve the attitude solution. The explanation for the small improvement is, on the one hand, the low signal power (Figure 3.5a) of the dither spikes despite their high amplitude (Figure 3.5c), and the fact that the use of the FFT does not result in a very accurate estimate of the amplitude. In other words, this method will always produce an amplitude spectrum with a standard deviation of 100% of the estimated value, independent of the data length (Kay and Marple, 1981). This means that the amplitude of the dither spikes may not be accurately established. A better accuracy of the amplitude spectra can be achieved by either constructing the spectrum with a finer than needed resolution by using a longer data

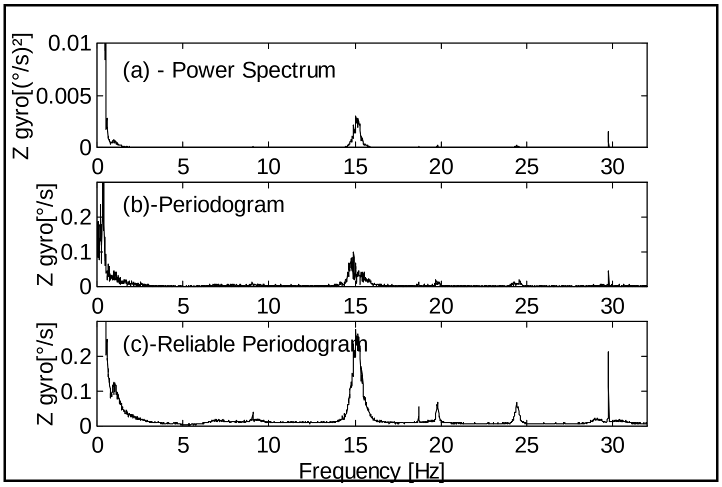

Figure 3.5. Spectra of raw INS azimuth signal in flight conditions, (a)-Power spectrum, (b)-Amplitude spectrum with σ_f= 100% of *E(f)*, (c)-Amplitude spectrum with σ_f= 25% of *E(f)*.

set and then average a certain number of consecutive frequencies, or by combining several spectral estimates from a partitioned data set (Figure 3.5c). Unfortunately, using such alternative methods would create difficulties in the spectrum-to-time domain transformation, although some form of re-scaling could most likely be used. A better choice for removal of dither ‘spikes’ would possibly be a notch filter (Oppenheim and Schafer, 1989) with adaptive selection of the frequencies according to the data analysis. This approach would be especially valuable if noise ‘spikes’ occur within the frequency band of interest. However, when the residual dither frequencies are detected beyond the motion threshold, the low-pass filter can effectively suppress their magnitude together with the noise.

Comparing the different windowing functions, it can be concluded that all methods performed equally well. This is due to the fact that the inertial signal power at the 8 Hz cut-off frequency is rather low and, therefore, a broader transition band is not as critical as achieving good attenuation in the stop band. Although some frequencies in the stop band have significant power (Figure 3.5a), the attenuation of 30-40 dB of the Bartlett window seems to be sufficient in this case. However, if the use of a different aircraft causes stronger vibrations, the application of window functions with better attenuation would be more appropriate (e.g. Blackman 60-80 dB). If aliased frequencies of high amplitude would be closer to the cut-off frequency, then using a higher-order filter can make up for a larger main lobe width to sharpen the transition band, while maintaining approximately the same ripple attenuation. Empirical testing showed that a filter order of approximately 120 yields the best results.

Within the class of optimally designed low-pass filters, the least-squares approach seems to slightly outperform the Remez-exchange algorithm. However, this difference is small and could possibly be caused by the type of ‘RMS’ evaluation which obviously favors the square error minimization. If designed with heavy weights in the pass band, the ‘optimal’ low pass filters work comparably well with respect to the window design approach.

The sensitivity of the inertial data to any phase distortion is illustrated by showing the influence of a non-linear phase IIR Butterworth filter on the attitude determination. This type of filter is often used for INS data filtering prior to the mechanization. As can bee seen from Figure 3.4 and Table 3.2, the use of a Butterworth low-pass filter actually affects the azimuth estimation negatively.

3.3.2 Gravity Field Determination

In this test, the effect of reducing the short-term noise in inertial data by an optimal low-pass filter is investigated for a strapdown airborne gravity system. In this technique, pioneered at the University of Calgary (Wei and Schwarz, 1998), the gravity disturbance magnitude is determined by forming differences between the specific force measured by a strapdown INS and the aircraft acceleration observed by DGPS. Since the power of the gravity signal is very small compared to the power of the system noise, band pass filtering with an extremely low cut-off frequency (usually between 1/30 to 1/90 Hz) has to be applied to the INS/DGPS acceleration differences to extract the gravity information.

The tested data is a subset of a 100 x 100 km airborne gravity survey described in detail in Glennie and Schwarz (1999). Particulary, three flight lines (L) and three turns (T) have been chosen for comparison. The results are depicted in Figure 3.6 which shows the relative improvements in determining gravity disturbances for each data segment when an optimal low-pass filter with *fc*= 8 Hz is used prior to inertial data mechanization. It should be noted that the INS and DGPS data are first loosely integrated to correct GPS cycle slips before computing DGPS accelerations and to estimate accelerometer biases. The results show that although the raw gravity disturbances have been low-pass filtered down to 1/30, 1/60 or 1/90 Hz, respectively, the short-term inertial noise can still harm the accuracy of the system. This is most likely due to the aliasing effect of short-term noise on the estimation of accelerometer

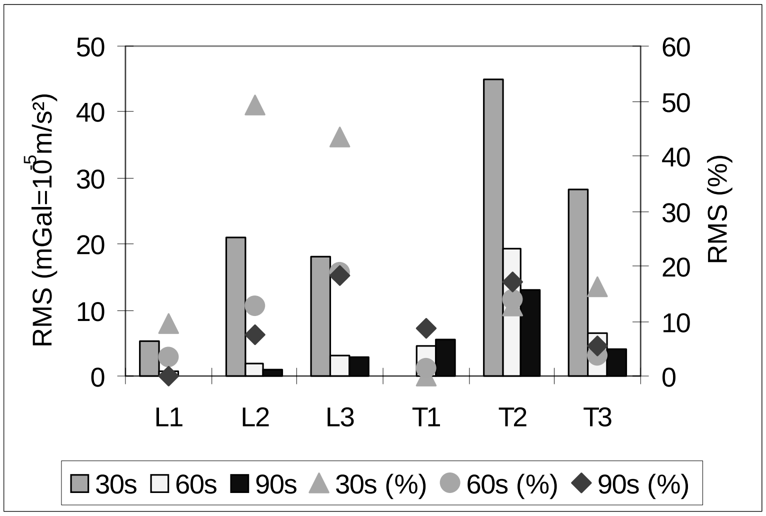

Figure 3.6. Noise level removed in gravity determination due to the inertial data band-limiting. Left y-axis denotes absolute improvements, right y-axis denotes relative improvements. Comparisons are made for three lines (L1-L3), three turns (T1-T3) and three system bandwidths of 1/30, 1/60 and 1/90 Hz.

biases. The changes are more apparent as the system bandwidth gets wider (1/30 as compared to 1/90 Hz), since the power of the noise increases too.

CHAPTER 4

DE-NOISING THE INS SIGNAL

This chapter describes a method which allows the theme of inertial data pre-filtering to be extended further to the frequencies where sensor noise is already mixed with the signal of interest but the integration with DGPS data does not filter it. The frequency band of interest, which is between the measurement period of external aiding with DGPS (typically 1-2 Hz) and the edge of the motion (typically 8 Hz), is schematically depicted in Figure 4.1.

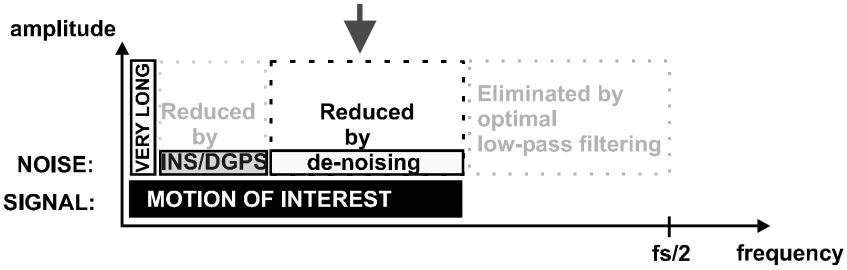

Figure 4.1. Effect of de-noising on the INS/DGPS spectrum.
Note: Figure is not to scale.

Filtering over a frequency band containing both signal and noise requires knowledge of how the noise and/or the signal are distributed with frequency, otherwise filtering may cause unacceptable signal distortion. However, a good prior knowledge of the short-term noise distribution is difficult to obtain due to one or more of the following reasons:

- The level and characteristics of the noise depend on the technologies employed and the manufacturer of the system.
- The level and characteristics of the noise can change as a function of environmental factors such as aircraft vibration, atmospheric turbulence and temperature.
- The noise level of a particular inertial system may change as a function of time (i.e. changes of sensor response with age or during warm-up).

Since good prior knowledge of the short-term signal is even more difficult to attain, a reliable model and estimation method for the noise level and its distribution has to be developed so that the inertial data can be filtered within the band of interest without distorting the inertial signal. Such a method should be applicable to different systems, with the ability to track time varying changes in the power and distribution of the noise. This chapter describes a model and filtering algorithm possessing these qualities. The whole filtering concept can be briefly summarized in three steps (see also Figure 4.2):

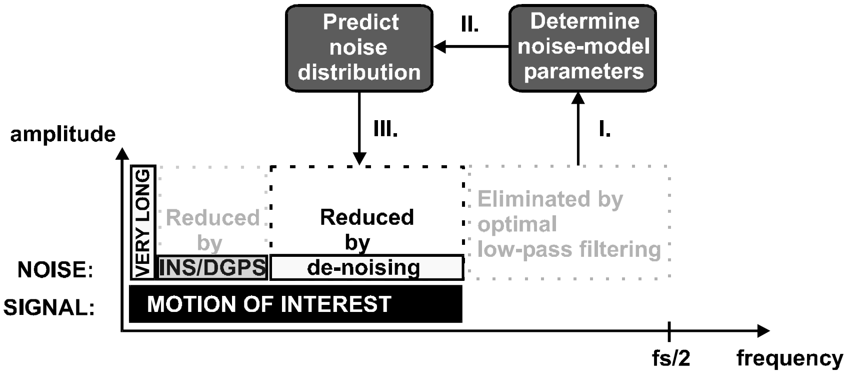

Figure 4.2. Concept of filtering INS short-term noise.
Note: Figure is not to scale.

- Determine the parameters of the model by observing the output of inertial sensors within a bandwidth where only noise is expected.
- Use the noise model to predict the noise distribution of lower frequencies of interest.
- Filter the noise within the frequency band of interest.

This chapter is further organized as follows. First, the general concept of de-noising (in-band filtering) using wavelets is introduced. Second, a model for the short-term errors is presented. The model is defined in the frequency and wavelet domains and a technique for adaptive estimation of model parameters is described. Third, the filtering methodology is tested using strapdown inertial systems from different manufactures. A substantial part of the research presented in this chapter follows the contribution of the first author in Skaloud at al. (1998).

4.1 Wavelet Transform

The advantages of modeling and filtering inertial short-term noise in the wavelet domain will become apparent later. First, the concept of wavelet transform is briefly described. Generally, the wavelet transform of a signal $x(t)$

$$x(t) \Leftrightarrow X_{\nu}^{\mu} \tag{4.1}$$

is defined in terms of projections of $x(t)$ onto a family of functions that are all normalized dilations and translations of a 'wavelet' function $\psi(t)$, i.e.,

$$W\{x(t)\} = X_{\nu}^{\mu} = \int_{-\infty}^{\infty} x(t)\,\psi_{\nu}^{\mu}(t)\,dt$$

where, (4.2)

$$\psi_{\nu}^{\mu}(t) = |\mu|^{-1/2}\,\psi\left(\frac{t-\nu}{\mu}\right)$$

In this notation, μ and ν are the continuous dilatation and translation parameters, respectively; they take values in the range $-\infty < \mu, \nu < \infty$, $\mu \neq 0$. The wavelet theory has been more fully developed for the case of dyadic orthonormal wavelet bases, corresponding to the case of $\mu = 2^{-m}$, $\nu = n2^{-m}$, where m and n are the dilation and translation indices, respectively. The base functions are then all dilatations and translations of a single base function referred to as the *mother wavelet* $\psi(t)$. Particulary,

$$\psi_{n}^{m}(t) = 2^{m/2}\,\psi(2^{m}t-n) \tag{4.3}$$

Then, an orthonormal wavelet transformation of the signal $x(t)$ can be described in terms of the synthesis/analysis equations as

$$x(t) = W_{d}^{-1}\{x_{m}^{n}\} = \sum_{m=-\infty}^{\infty}\sum_{n=-\infty}^{\infty} x_{m}^{n}\,\psi_{n}^{m}(t)$$

(4.3)

$$x_{m}^{n} = W_{d}\{x(t)\} = \int_{-\infty}^{\infty} x(t)\,\psi_{n}^{m}(t)\,dt$$

When transforming a sampled rather than continuous signal between time and wavelet domains, a discrete-time framework of the orthonormal wavelet transform is implemented. The implementation is based upon a bank of discrete-time filters that have essentially halfband lowpass and highpass characteristics with special properties for removing distortion and aliasing (for details, see Strang and Nguyen, 1996). These filters are always critically sampled. That means that in the analysis filter bank, each filtering step is followed by down-sampling while in the synthesis filter bank up-sampling precedes filtering. The structure of the Discrete Wavelet Transform (DWT) algorithm is depicted in Figure 4.3. In the analysis algorithm, the input signal x_n^M of finite length is separated by the pair of filters H_M, L_M at the scale M into 'fine' and 'coarse' coefficients x_n^{M-1} and a_n^{M-1}, respectively. While the coefficients describing the signal details at this scale are retained, the coarse coefficients at the scale $M-1$ are further analyzed by another pair of filters. This scheme is repeated to extract the transform coefficients x_n^m corresponding to successively coarser scales m. The synthesis algorithm is structured in a complementary fashion. The structure of an orthogonal bank is very special in the sense that at corresponding scales the filter pairs are transposes of each other. This property further increases the computational speed. When the length of the signal is $n=2^M$, the computation of filter coefficients is further simplified. Such a case is known as Fast Wavelet Transform (FWT).

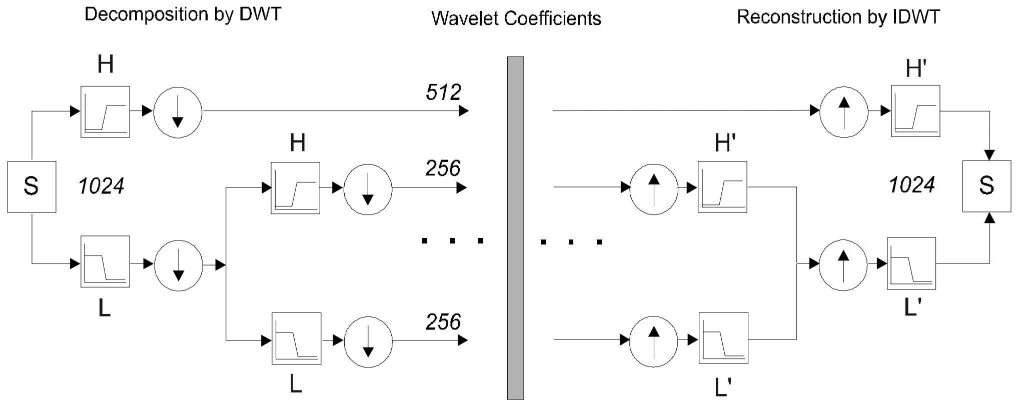

Figure 4.3. The structure of the multi-level wavelet decomposition and reconstruction.

4.2 De-Noising by Wavelet Coefficient Thresholding

This section describes a general method of data de-noising using wavelets as proposed by Donoho and Johnstone (1994, 1995). This method attempts to reject noise by thresholding the wavelet coefficients of the noisy signal and has been successfully applied in many situations where other non-wavelet methods have met only partial success. It is superior to other methods, especially when the signal of interest is of unknown smoothness, as is the case of inertial measurements. The method has three main steps:

1. Apply DWT to the measured data to obtain empirical wavelet coefficients.
2. Apply the soft thresholding non-linearity

$$\eta_t(y) = \operatorname{sgn}(y)(|y| - t)_+ \tag{4.4}$$

   to the empirical wavelet coefficients with a specially chosen threshold, where the function *sgn* returns the 'sign' of its argument and $(\cdot)_+$ gives zero if the expression inside the brackets is negative.
3. Invert DWT to recover the de-noised version of the signal.

Obviously, the choice of the threshold in step 2 is crucial. Considering only white noise, Donoho and Johnstone (1995) introduced near optimal thresholding by an adaptive threshold selection which uses the principle of Stein's Unbiased Risk Estimate (SURE) to select a near-optimal threshold t^s according to:

$$t^{s} = \operatorname{argmin}_{0 \le t \le \sqrt{2\log N}} \mathrm{SURE}(t; \boldsymbol{x})$$

where,

$$\mathrm{SURE}(t; \boldsymbol{x}) = N - 2 \cdot \#\{ i : |x_i| \le t \} + \sum_{i=1}^{N} [\min(|x_i|, t)]^2 , \tag{4.5}$$

‘argmin’ is the minimal argument and # denotes the number of members in a set $\{\cdot\}$. This sophisticated threshold selection detects situations of extreme sparsity of the wavelet coefficients (e.g. low SNR) and uses the upper bound $\sqrt{2\log N}$ as a fixed form of thresholding in such cases. Empirical testing of inertial data showed that this method works well in this case.

The selection of the threshold in Equation (4.5) has been derived by assuming only white-noise *N(0,1)* in the data. When the signal is corrupted by white noise of intensity σ, the wavelet coefficients have to be appropriately scaled (normalized) beforehand. If there is no prior knowledge about the noise power, Donoho and Johnstone (1995) suggested to estimate σ empirically as the median of the wavelet coefficients at the finest scale. When not only white but also correlated noise are present, the normalization of the wavelet coefficients becomes more difficult, since the variation of the noise distribution at each scale has to be determined.

The following section introduces a model for short-term inertial noise that is expressed in the frequency and wavelet domains, and whose parameters can be estimated directly from the data.

4.3 A $1/f^{\gamma}$ Model for Short-Term INS Errors

The prevailing error sources belonging to the category of short-term errors have been described in Chapter 2. The noise model being presented in the following is a compromise between the complexity of individual inertial error spectra, the main features common to different systems, and the number of parameters used. The main model characteristic is the invariance of error distribution with respect to scale. The family of stochastic processes exhibiting scale invariance are called statistically self-similar random processes or $1/f^{\gamma}$ processes. Their power spectra obey a power law relationship of the form

$$PSD(\omega) = \frac{\sigma_x^2}{|\omega|^{\gamma}} \tag{4.6}$$

over the frequencies ω and for some finite and non-zero parameters σ_x and γ. The sample paths of such processes are typically fractals for a constant γ, and multi-fractals (fractals with varying dimension) when γ is a function of frequency. Traditionally, the properties of $1/f^{\gamma}$ behavior have been studied in the framework of fractional Brownian motion; see Mandelbrot and Van Ness (1968). Since then, it has been demonstrated that a tremendously varied collection of natural phenomena exhibit or $1/f^{\gamma}$ type behavior (Stewart, 1989). These include optical path variation, such as polarization wander causing bias instabilities in the FOGs (Bielas, 1994), or instabilities in the RLG output as supported by empirical observations presented here and by Li and Schwarz (1995).

4.3.1 A 1/f$^\gamma$ Model in the Frequency Domain

A visual indication that a power-law relationship similar to Equation (4.6) approximates short-term inertial noise well is shown in Figure 4.4. This figure displays short-term inertial noise in a time series (a), as well as its amplitude spectrum on a normal (b) and logarithmic scale (c), respectively. Using Equation (4.6), the parameter γ can be expressed by the ratio of the logarithm of the signal spectrum with respect to the logarithm of its frequency. Hence, an empirical estimation of the parameter γ is possible directly from the last two plots in

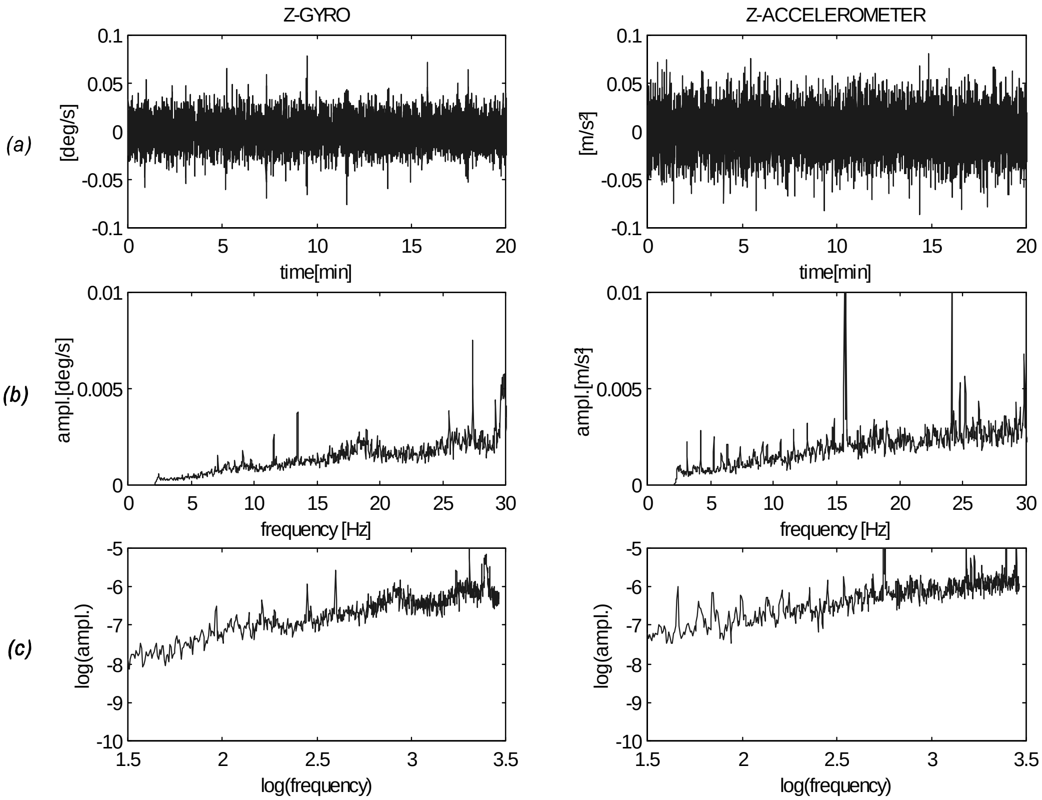

Figure 4.4. Raw signal (noise) from the vertical channel of a stationary strapdown INS in time domain (a), and frequency domains (b), (c).

Figure 4.4 by computing the slope of a line fitted to the data points[1]. Although such a method gives a good indication of the presence of scale-correlated noise, it lacks robustness when broadband noise is present in the data. Since the signal from inertial sensors usually contains broadband noise of some power, this should also be reflected in the model. A model which considers both the self-similarities and broadband noise in short-term inertial errors has the following form

$$PSD(\omega) = \frac{\sigma_x^2}{|\omega|^{\gamma}} + \sigma_w^2 \tag{4.7}$$

where σ_w^2 characterizes the amplitude of the white noise floor in the inertial data, and where the parameters σ_x and γ account for the noise self-similarities. Hence, the parameter set which needs to be estimated is

$$\boldsymbol{\theta} = (\gamma, \sigma_x^2, \sigma_w^2) \tag{4.8}$$

The following section describes the wavelet-based characterization of the model (4.7) and the advantages stemming from this transformation.

---

[1] In the case of using amplitude spectra instead of PSD, $\gamma/2$ is obtained.

4.3.2 A $1/f^{\gamma}$ Model in the Wavelet Domain

Wornell and Oppenheim (1992) introduced a wavelet-based model for $1/f^{\gamma}$ processes accompanied by an additive stationary white noise component. Since the white noise is assumed to be independent of the $1/f^{\gamma}$ process, the wavelet coefficients of both processes are also independent. Then, the resulting wavelet coefficients of the noise model in Equation (4.7) can be modeled as zero-mean random variables having negligible correlation:

$$r_n^m = x_n^m + w_n^m \, . \tag{4.9}$$

They obey a variance progression of the form

$$var(r_n^m) = \sigma_m^2 = \sigma^2 \, 2^{-\gamma m} + \sigma_w^2 \, . \tag{4.10}$$

In turn, the *synthesis filter* is defined as

$$x(t) = W_d^{-1}\left\{ (\sigma 2^{-\gamma m/2} + \sigma_w) \, W_d \{ v(t) \} \right\} \tag{4.11}$$

where *v(t)* is a wide-sense stationary white noise process. The inverse of this filter yields a corresponding *whitening filter* for the $1/f^{\gamma}$ noise model. Hence the parameter set fully describing the original noise model (4.7) in the wavelet domain is

$$\boldsymbol{\Theta} = (\gamma, \sigma^2, \sigma_w^2) \, . \tag{4.12}$$

A preliminary investigation of the properties of wavelet coefficients is undertaken in the following. The wavelet coefficients are computed from the z-gyro noise and the empirical variance is computed for each scale, using the same data displayed in Figure 4.4. As shown in Figure 4.5(a), a line fitted to the variances of the wavelet coefficients from scale to scale obeys a geometric progression consistent with a $1/f^{\gamma}$ process for which $\gamma \approx -1.8$. Had the data been generated by a pure $1/f^{\gamma}$ process, the progression of the log-variances would be asymptotically linear, i.e it would follow the line fit. Apart from random noise, the estimate of the variances is also affected by the scale. Since the number of samples available for the estimate doubles at each successively finer scale, the standard deviation of the estimated

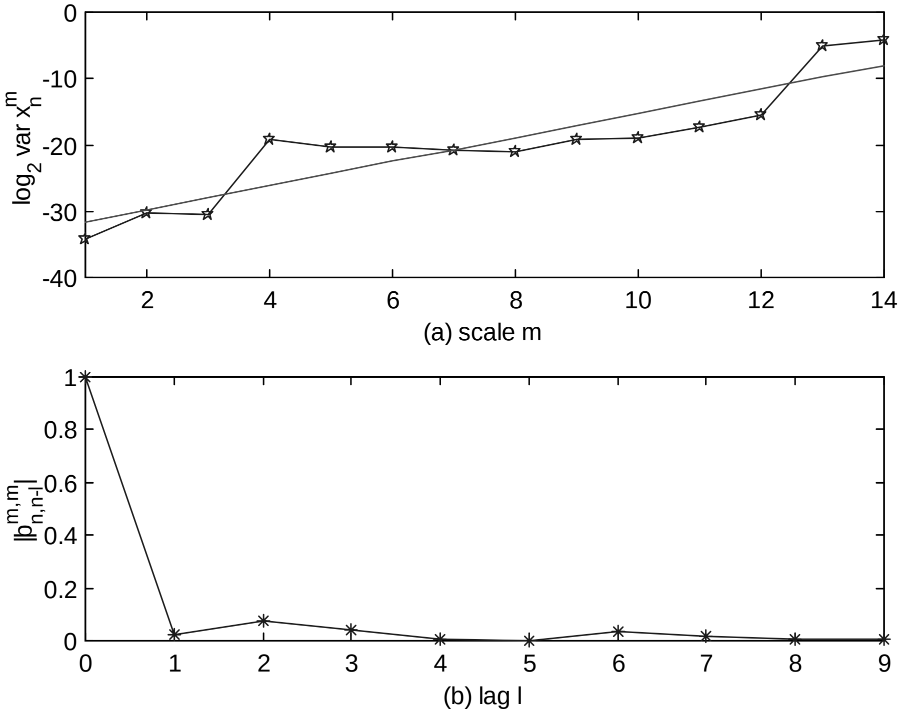

Figure 4.5. Wavelet analysis of vertical gyro signal in static environment using a 12-th order Daubechies wavelet basis. (a) Scale-to-scale wavelet coefficient sample-variance progression. (b) Average magnitude of the normalized along-scale sample-correlation between wavelet coefficients.

variance decreases by a factor of $\sqrt{2}$ for each successive increase in m. Figure 4.5(b) shows that the average along-scale sample-correlation among wavelet coefficients is rather weak. Adjacent coefficients have a correlation of less than 7 percent, and more widely separated coefficients have a correlation of less than 2 percent. Such a behavior is also consistent with a $1/f^{\gamma}$-type model for the data.

Formulating the noise model in the wavelet domain has several benefits. The first advantage is the fast and robust method of model parameter estimation which will be described later. Second is the simple noise normalization needed for de-noising. Considering the wavelet based model for short-term inertial noise (4.10), such scaling is rather simple. Prior to thresholding, the empirical wavelet coefficients are divided at each scale m by a constant σ_m computed as $\sigma_m = \sqrt{\sigma^2 2^{-\gamma m} + \sigma_w^2}$, where the necessary parameters γ, σ, σ_w have been determined by the procedure described in the following section. Such scaling removes the correlation between the scales and also normalizes the white noise. Hence, the remaining noise has a distribution of $N(0,1)$ and the de-noising algorithm can be applied.

4.4 Estimation of Noise Parameters

This section describes a method for determining the short-term noise parameters by analyzing the content of the inertial signal above the bandwidth of the motion. An important assumption is that the actual output of the INS is well over-sampled. As has been already mentioned in Chapter 3, such an assumption is reasonable for civilian applications where the sampling rate of the inertial sensors usually exceeds the frequency content of the motion by 10-50 times depending on the system. This provides a sufficiently broad bandwidth (number of frequency scales) which contain only noise and can be used to estimate the noise model parameters. Once the noise-parameter set is known, model (4.10) is used to predict the magnitude of the noise in the band that contains both noise and motion. Subsequently, a de-noising algorithm can be applied in this band. Hence, the signal used for noise-parameter estimation is the ‘pure’ inertial noise at frequencies higher than the actual vehicle motion. Such signal can be obtained from the raw inertial data by high-pass filtering[2] with a frequency cut-off that depends on the dynamics of the vehicle which for most civilian applications will be 10 Hz at most.

Considering the inertial noise with $1/f^{\gamma}$-type behavior, the parameter set to be determined follows from Equation (4.10) as $\boldsymbol{\Theta} = (\gamma, \sigma^2, \sigma_w^2)$. Although a variety of estimators exists for the parameters describing $1/f^{\gamma}$ noise (e.g. Pilgram and Kaplan, 1998), a method introduced by Wornell and Oppenheim (1992) will be used for the following reasons:

- It employs Maximum Likelihood (ML) estimation which results in a robust solution, even for a low signal-to-noise ratio (SNR),

---

[2] Design of filter coefficient is as described in Chapter 3, except the pass and stop bands are interchanged.

- It exploits the wavelet-based characterization for the $1/f^{\gamma}$ noise model which is closely linked to the filtering methodology that is applied once the signal parameters have been estimated,
- It allows fast computation via the Fast Wavelet Transform (FWT) and ML estimation in the wavelet domain.

The most important of these properties is robustness, because the noise parameters are going to be determined from data which are limited in both time and resolution. Also, unlike some other estimation techniques, it is not corrupted by broad band noise sources, often dominant in inertial data.

4.4.1 Algorithm Derivation

The main steps of the noise estimation algorithm are outlined below. The observations *r(t)* are the inertial data after high-pass filtering. They are assumed to be products of a zero mean $1/f^{\gamma}$ process *x(t)* embedded in zero-mean additive white Gaussian noise *w(t)* that is statistically independent of *x(t)*. The computationally efficient DWT is applied to a segment of data yielding coefficients r_n^m with a finite set of available scales $\mathbf{M} = \{1, 2, ..., M\}$ and a set of available coefficients for each scale $\mathbf{N}(m) = \{1, 2, ..., N_o 2^{m-1}\}$, where N_o is a constant that depends on the length of the wavelet filter. Following Wornell and Oppenheim (1992), the log-likelihood function of the parameter set $\boldsymbol{\Theta}$ (Equation 4.12) can be expressed as

$$L(\boldsymbol{\Theta}) = \ln p_{\boldsymbol{r}}(\boldsymbol{r};\boldsymbol{\Theta}) = -\frac{1}{2}\sum_{m\in \mathrm{M}} N(m)\left\{\frac{\hat{\sigma}_m^2}{\sigma_m^2} + \ln(2\pi\sigma_m^2)\right\} \tag{4.13}$$

where $\hat{\sigma}^2$ are the **M** sample-variances computed from the data as

$$\hat{\sigma}_m^2 = \frac{1}{N(m)}\sum_{n\in N(m)} (r_n^m)^2 \ . \tag{4.14}$$

Differentiating $L(\boldsymbol{\Theta})$ with respect to γ, σ^2, and σ_{w}^2 maximizes the likelihood functions and provides the stationary points of $L(\boldsymbol{\Theta})$ as solution to the equations

$$\begin{aligned} \sum_{m\in \boldsymbol{M}} T_m &= 0 \\ \sum_{m\in \boldsymbol{M}} 2^{-\gamma m} T_m &= 0 \\ \sum_{m\in \boldsymbol{M}} m 2^{-\gamma m} T_m &= 0 \end{aligned} \tag{4.15}$$

where

$$T_m = \frac{N(m)}{\sigma_m^2}\left[1 - \frac{\hat{\sigma}_m^2}{\sigma_m^2}\right] \tag{4.16}$$

Except in special cases, the system of equations in (4.15) is difficult to solve. An iterative ‘estimate-maximize’ (EM) algorithm (Laird et al., 1977) is therefore used. The essential steps in this algorithm are summarized in the Appendix A. A detailed development of the algorithm can be found in Wornell (1996). This reference also discusses the properties of the estimators and shows that the EM algorithm iterates toward the ML parameters unless the starting value of one of $\hat{\gamma}, \hat{\sigma}^2, \hat{\sigma}_w^2$ is chosen to be exactly zero. A later study by Ninness (1998) presented an analytical proof demonstrating that for $\gamma>1$ the algorithm converges to the wrong estimate when the power of broad-band noise reaches a certain threshold. This property is intuitively understandable, since in such a case most of the signal power is located in the low frequency region which is poorly observable because of the finite data length. However, this drawback practically does not apply when dealing with raw strapdown data, since some form of differential spectrum ($\gamma<0$) can be expected for this signal (Li and Schwarz, 1995). In other words, for $\gamma<0$ most of the signal power is distributed over the high frequency band which is essentially used for the noise parameter estimation. Should the power of broad-band noise prevail in this frequency band, the algorithm correctly estimates $\hat{\sigma}_w^2 » \hat{\sigma}^2$, and subsequently the model (4.7, 4.10) predicts only the white noise in the lower frequency band.

4.4.2 Algorithm Validation

Monte Carlo simulations were performed to assess the performance of the noise parameter estimation algorithm described in Section 4. The $1/f^{\gamma}$ processes were generated using a model introduced by Kasdin (1995). This model was chosen because its nature is fundamentally different from the wavelet based synthesis and therefore provides an independent reference for algorithm verification. The method generates the $1/f^{\gamma}$ signal by filtering a white-noise sequence with an Infinite Impulse Response (IIR) filter. Although a number of $1/f^{\gamma}$ models are based on white noise modulation, most of them approximate this process only to a certain level. However, this IIR implementation truly preserves the scale-invariance over a frequency band of arbitrary size.

Twenty runs with a data length of 2^{15} (32768) were simulated for a specific γ varying from -2 to 2. Then the model parameters were estimated and compared to the actual ones. From these discrepancies, the mean and the root mean square (RMS) errors are computed. Figures 4.6 and 4.7 display the accuracy of estimating γ as a function of the window length. It shows that γ can be estimated with an RMS of 0.1 or better for the interval $\gamma \in [-1,1]$ when using a window of 2^{12} (4096) or longer. This suggests that for a 64 Hz data sequence, the eventual changes in γ can be tracked over a period of one minute. When the absolute value of γ approaches 2, the accuracy of the estimate decreases about two times, but its mean value is

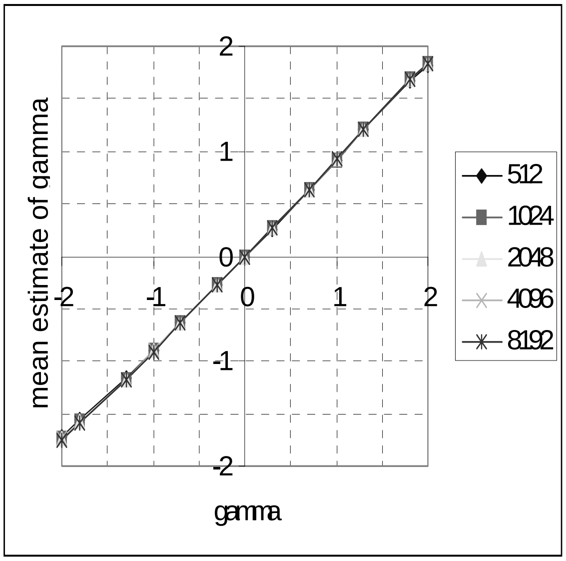

Figure 4.6. Mean estimate of γ as a function of data length.

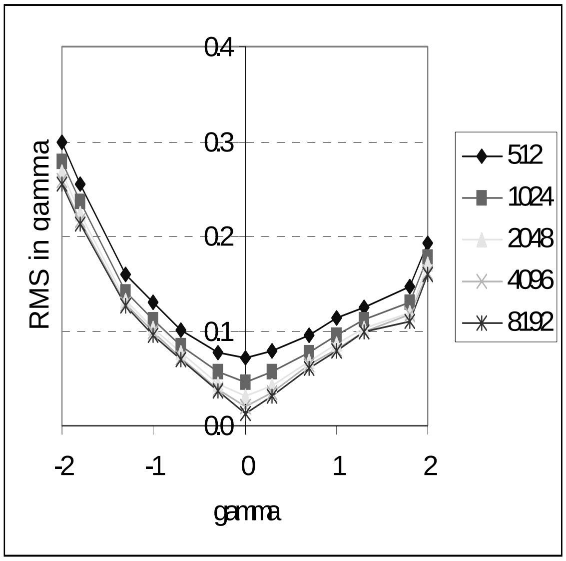

Figure 4.7. RMS error of the estimates of γ as a function of data length.

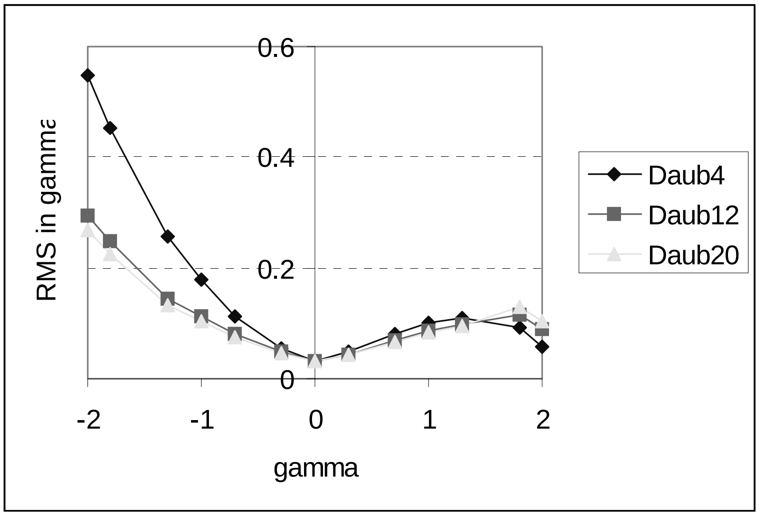

Figure 4.8. RMS error in the estimates of γ as function of the choice of wavelet smoothness.

not affected much. It should be noted, however, that these somewhat larger discrepancies may be caused by the errors in the simulation algorithm. This algorithm has been derived within the framework of fractional Brownian motion which provides the useful model construction only when spectral exponents are in the range $-1< \gamma< 1$ and $1< \gamma< 3$. On the contrary, the wavelet based model for *1/f*-type behavior does not posses such a restriction (Wornell, 1996).

The dependence of algorithm performance on wavelet order is depicted in Figure 4.8. The estimation of γ seems to be relatively insensitive to the wavelet smoothness especially within the positive region of γ. These results are fairly consistent with those presented in Wornell and Oppenheim (1992). Further details about the performance of the algorithm, including its dependence on the SNR, can be found in Wornell (1996).

4.5 Analysis of De-Noising Performance

The noise detection concept and the filtering methodology will be validated in two main steps:

- The noise structure in specific navigation-grade inertial systems of different brands will be studied.
- The whole methodology including the de-noising will be tested in a dynamic environment and compared to an independent attitude reference.

4.5.1 Detection of Short-Term Noise

This section analyzes the signals from two navigation-grade inertial systems of different manufacturers, namely the Honeywell LASEREF III and the Litton-90-100. Both data were collected in an airborne environment, but different planes and flying patterns were used. The LASEREF III data was collected for an airborne gravity survey using a strapdown INS/DGPS mounted in a CESSNA Conquest turbo prop airplane (Glennie and Schwarz, 1999). The other data set was collected in a smaller aircraft called the Partenavia P68C, which is commercially used for aerial surveys. In this case, the INS/DGPS system was providing position and attitude data with sufficient accuracy for georeferencing aerial imagery collected simultaneously without the costly establishment of ground control points. For a detailed description of the test, see Chapter 7. The missions started with alignment periods of 15 and 20 minutes, respectively.

The noise analysis is performed on the signals after high-pass filtering as described in Section 4.4. The noise parameter set (γ, σ, σ_w) is continuously estimated using a moving window of 4096 data points (~1 minute) with a step size equal to 1/4 of its length. Figures 4.9 and 4.10 display the evolvement of (γ, σ, σ_w) in the *y* and *z* gyros of both systems. The general noise behavior is very interesting. Although the power of the noise is stronger in the *y*-channels, its prevailing structure is similar in both systems and channels. Since $\gamma \approx -2$ most of the time, the analyzed signal essentially consists of white-noise and its derivative. The noise in the *z*-channel of the LASEREF III exhibits only small changes between the alignment and the actual flight. The same is true also for the vertical gyro of the LTN-90-100 system, except that an increase in the noise magnitude from the alignment period is obvious. This difference is due to the fact that the alignment of the LTN-90-100 system was performed with engines off, while the LASEREF III was aligned with aircraft engines running. A rapid increase of the white noise floor in the *y* (roll)-channel during the take-off is apparent in both systems. The oscillations of noise magnitude in this channel are generally smaller during the flight, but its power remains 5 to 10 times larger than for the *z* (azimuth)-channel. This indicates considerable differences between the magnitude of engine-induced vibrations with respect to the horizontal and vertical axis of the aircrafts. In one case, the structure of the noise in one sensor does not fit the general pattern observed in the others. During the alignment of the LTN-90-100, the magnitude of γ is ≈ -0.5 in the *y*-gyro. This is

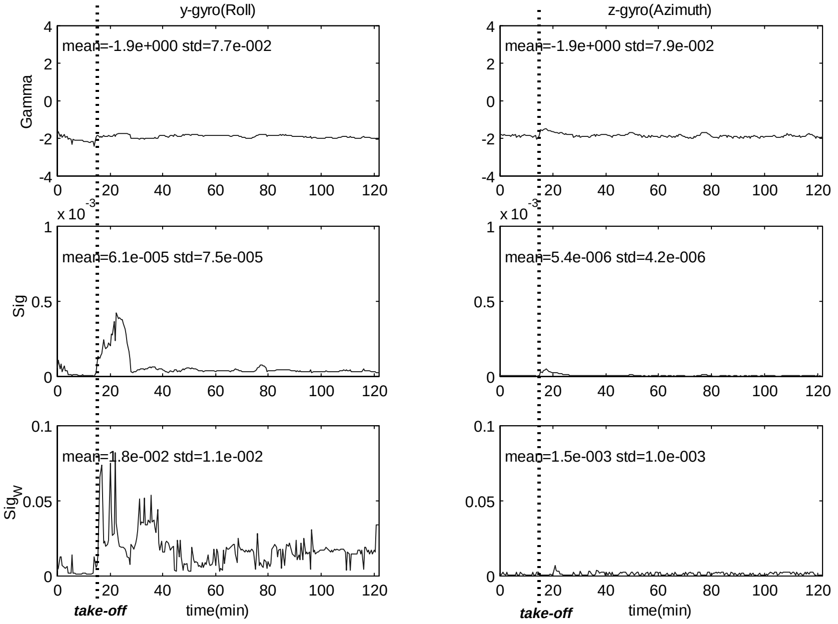

Figure 4.9. Evolution of short-term noise parameters (γ, σ, σ_w) in the Honeywell LASEREF III mounted in a Cessna Conquest (15 min of alignment with the engines ON followed by take-off).

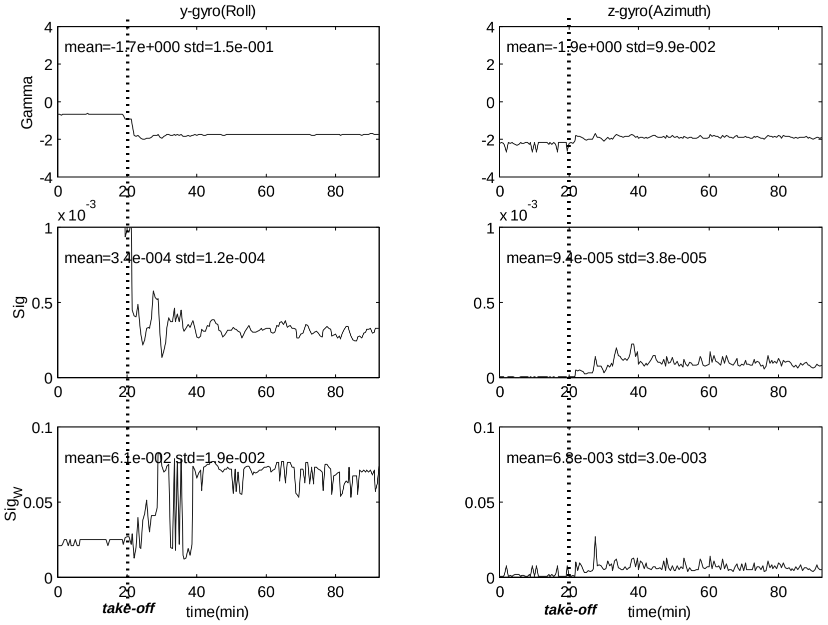

Figure 4.10. Evolution of short-term noise parameters (γ, σ, σ_w) in the Litton LTN-90-100 system mounted in P68C (20 min of alignment with the engines OFF followed by take-off).

different from all other cases including the *x*-gyros and accelerometers (not shown), which all oscillate about *-2*. Since no external vibrations were present during the alignment, this may indicate a problem in this particular sensor.

4.5.2 De-Noising Results with a Navigation-Grade INS

The whole noise detection/filtering scheme was tested for an LTN-90-100 data set where an independent attitude control was available during the flight at 75 discrete points (for a detailed test description, see Chapter 7). Since there is some variation in the noise parameters during this flight after take-off (Figure 4.10), the noise model was defined by taking the mean values of the parameters over the cruising period. The de-noising algorithm used a modified SURE soft-thresholding as described in Section 4.2 and the signal was decomposed using the Daubechies wavelet of order 20. Figure 4.11 displays the STD values computed from the discrepancies between the observed and control values in azimuth. It compares the quality of the azimuth determination by INS/DGPS integration for the cases where

- no band limitation was performed on the raw data,
- data were band-limited using an optimal low-pass filter (Chapter 3),
- in-band filtering was performed on already band-limited data using the method presented here.

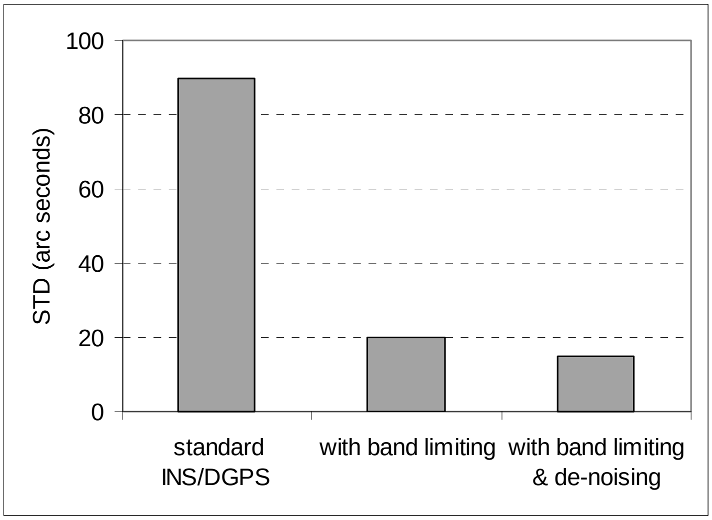

Figure 4.11. Attitude accuracy gain through in-band filtering of short-term inertial noise.

The overall improvement is remarkable. Its major component (of about 75%) is due to optimal band limitation which performs noise reduction over a substantially wider bandwidth than the de-noising component. Also, since $\gamma<0$, the power of the noise increases with the frequency and thus more of a short-term noise can be reduced by the band limitation than by in-band filtering. However, the application of the de-noising algorithm with correctly estimated noise parameters further reduces the inertial short-term noise by about 20%.

4.5.3 De-Noising Results with a Tactical-Grade INS

The use of a tactical-grade INS/DGPS for direct-georeferencing represents an attractive option for applications with lower accuracy requirements. The system to be tested is the C-

MIGITS II which belongs to a family of miniature integrated INS/GPS tactical systems developed by Rockwell International Autonestics and Missile Systems Division. Its tightly coupled configuration contain a five channel Coarse/Acquisition (C/A) code, L1 frequency GPS engine and a Digital Quartz Inertial (DQI) Measurement unit. The DQI is a strapdown IMU built by Rockwell around a low-cost inertial sensor assembly manufactured by Systron Donner and containing three vibrating quartz accelerometers (VQA) and three quartz rate sensors (QRS) and their associated drive and analog-to-digital conversion electronics. For a more detailed technical description, see Macdonald et al. (1996) or Rockwell (1996).

Although the C-MIGITS II provides the INS/GPS[3] navigation solution in real-time, post mission processing has been employed to investigate the effect of short-term noise reduction by band-limiting and de-noising with respect to attitude determination. The recorded 100 Hz raw data has been mechanized and integrated with differential code and phase measurements of the Ashtech Z12 receivers using a 15-state decentralized KF. The reference was provided by the output of a navigation-grade INS (LTN-90-100) with DGPS aiding using the same pair of receivers. The C-MIGITS II was mounted on top of the LTN 90-100 frame with a known spatial offset between the IMUs and the GPS antenna common to both systems. The presented analysis uses a first data set collected to evaluate the C-MIGITS II attitude accuracy in the operational environment of a small aircraft (Cessna 310) as described in

---

[3] This unit can also deliver INS/DGPS solution if differential C/A corrections are provided in the real-time.

Skaloud et al. (1997). A thorough analysis of the whole test will be presented in Bruton et al. (1999b).

The test was of approximately 20 minutes duration and consisted of the take-off, a heading maneuver (a figure eight pattern), a short flight under a constant azimuth and the touch down. Since the high noise level in the C-MIGITS II prevents the static alignment of the system, the initial orientation was supplied by the LTN-90-100 (for discussion on dynamic alignment see Section 6.4). The evolution of the attitude differences between both inertial systems is depicted in Figure 4.12. Since the LTN-90-100 with DGPS aiding can provide attitude with

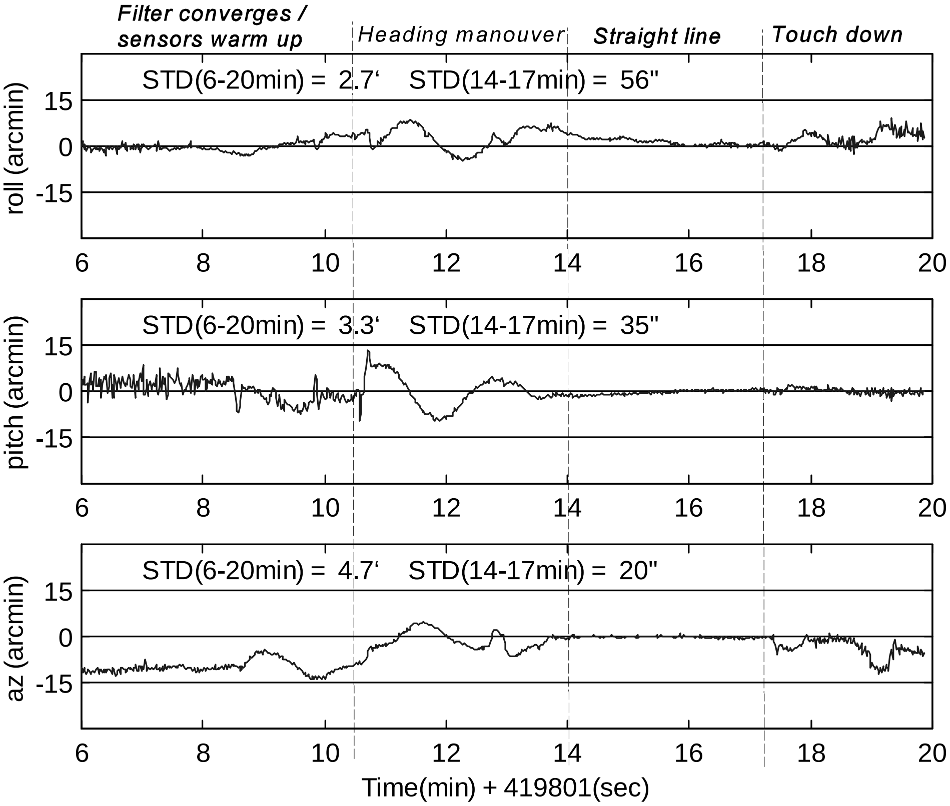

Figure 4.12. The differences between the attitude of LTN-90-100 and C-MIGITS II after integration with the same DGPS code and phase measurements.

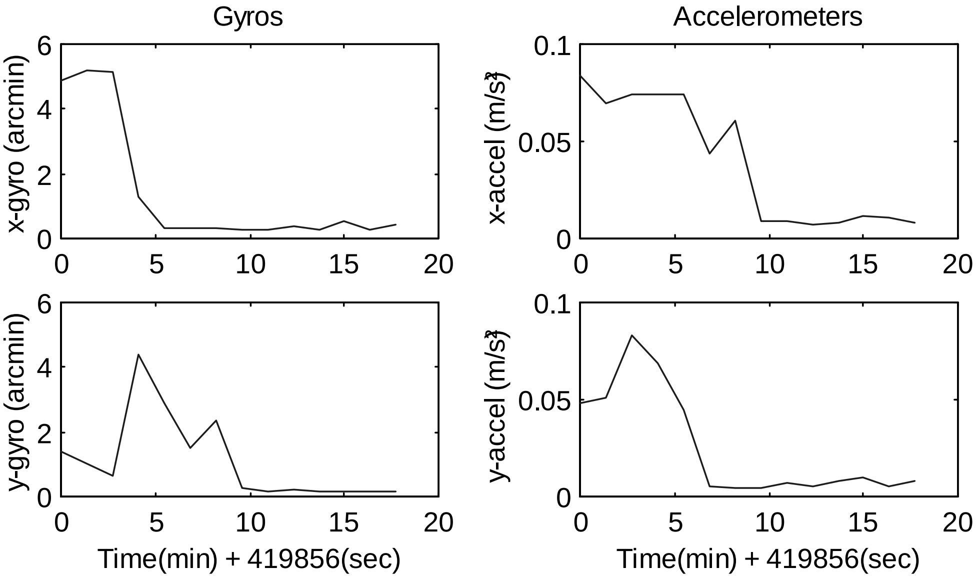

Figure 4.13. Estimation of the white-noise intensity in the C-MIGITS II *x*,*y* sensors.

an accuracy of 10-20 arc second (1σ) (see Chapter 7) these differences can be considered as the orientation errors in the C-MIGITS II. As can be seen from the figure, the errors consist of short and long-term components. Only the former will be reduced by inertial data preprocessing.

A substantial error source in the QRS is the high noise level. Although the $1/f^{\gamma}$ noise has not been reported in these sensors, the noise model (4.7) is applicable also to represent broad band white noise. Hence, the noise-model parameters can be estimated in the same fashion as outlined in Section 4.4. Figure 4.13 depicts the evolution of its intensity estimated from the high-pass filtered 8 Hz signal for the *x* and *y* channels. As can be seen from this figure, the intensity of the noise varies considerably during the system warm-up period (up to 10 minutes) and then settles around 0.5 arc minutes and 1-2 cm/s^2, respectively.

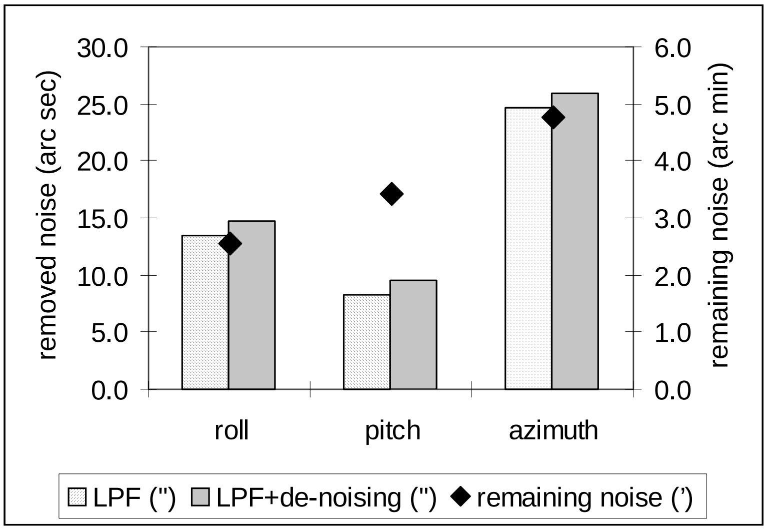

Figure 4.14. Noise reduction in tactical-grade INS/DGPS attitude determination by raw data pre-filtering.
Left y-axis: absolute noise level removed,
Right y-axis: absolute error remaining.

The effect of pre-filtering the C-MIGITS data is shown in Figure 4.14 with respect to attitude determination for the case of band-limiting at 8 Hz and then de-noising by means of SURE soft-thresholding with decomposition using the Daubechies wavelet of order 20. The absolute noise level removed is 15, 10 and 26 arc seconds for roll, pitch and azimuth, respectively. Although there is some improvement due to inertial data band-limiting and de-noising, the remaining orientation errors are still several times higher than the noise removed. This is shown in the last set plotted in Figure 4.14. These errors have low frequency characteristics and are most likely caused by the residual random drifts in the gyro output and variations of the scale factors which have not been estimated in the integration process. These errors are expected to become smaller when a KF with scale-factor states is used. Optimizing the KF configuration would, however, require more extensive testing. To at least partially decouple between the errors due to scale-factors and the short-term noise, the contribution of pre-filtering is studied in detail only during the flight period of constant velocity and azimuth. This is shown in Figure 4.15 for the case of pitch errors. As can be seen from the upper left plot of this figure, the errors in this channel can be described as a combination of short-term noise and drift with a slope character (fitted line) over this time period. When this drift is removed (upper right plot) the remaining orientation errors are at the level of 18 arc second. The data band-limiting and subsequent de-noising reduce these errors to about 2/3 of their original magnitude, but do not correct the low-frequency drift or

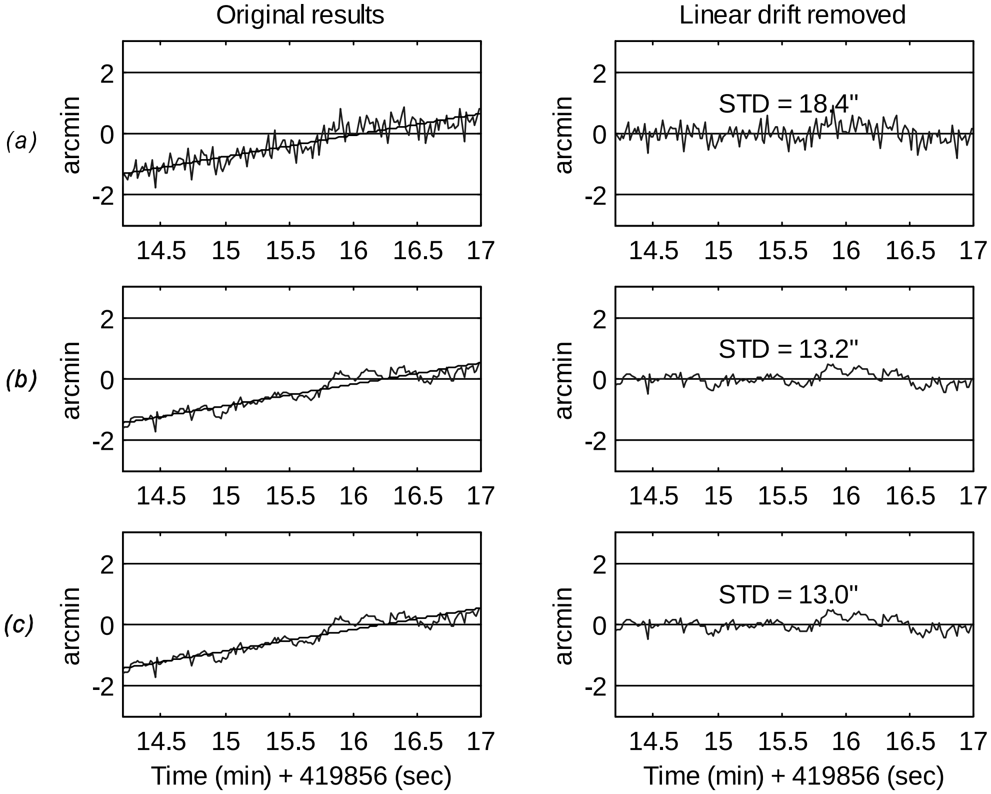

Figure 4.15. A detailed plot of pitch errors during a flight of constant velocity and azimuth. (a) original data, (b) data with band limiting, (c) data with band limiting and de-noising.

additional correlated noise of a spectral signature below the cut-off frequency of the low-pass filter.

CHAPTER 5

GPS AMBIGUITY ESTIMATION WITH INERTIAL DATA

Correct determination of the GPS carrier phase ambiguities is a prerequisite for accurate kinematic positioning, as schematically shown in Figure 5.1. This chapter investigates the possibility to increase the reliability of ambiguity estimation and validation by inertial measurements. The research diagnoses the two most popular INS/DGPS integration methods, the tightly and the loosely coupled integration, with respect to the on-the-fly (OTF) ambiguity search. The motivation for this study is to determine:

- which integration method allows, in general, the ambiguity to be determined over shorter time spans and with fewer satellites,
- whether or not the reliability of the process improves with the quality of the inertial system used.

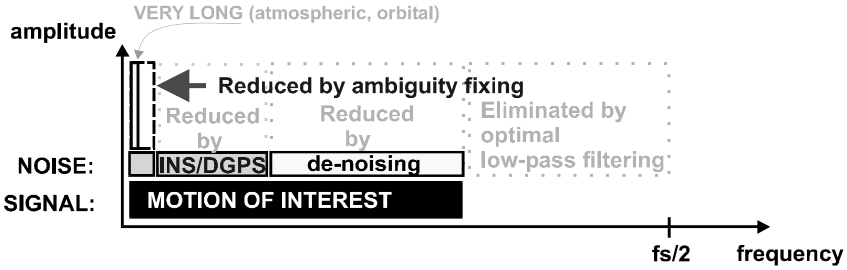

Figure 5.1. Effect of correct ambiguity determination on the INS/DGPS spectrum. Note: Figure is not to scale.

Answering these questions will result in making a better decision on the quality of an inertial system and the integration method used for a specific georeferencing application.

Although the process of ambiguity determination is a complex procedure depending on many factors related to the actual data, its core part can be analyzed by knowing only the relative ratios of the data accuracies. Moreover, Teunissen (1997) has shown that the problem of ambiguity estimation and validation is directly related to the properties of the ambiguity search space and provides closed formulas for evaluating its intrinsic characteristics with respect to different measurements (e.g. phase only, code and phase, dual frequency phase, etc.). This analysis continues in this spirit and provides analytical expressions for the case when inertial data are present. The derived expressions give an insight into how inertial measurements influence the ambiguity search space. They also serve as a tool for evaluating the benefits of different inertial systems without the need for physical testing.

The structure of this chapter is as follows. First, a summary of the ambiguity resolution problem with GPS single frequency and code observables is given in analytical form. Then, the observation model is extended to include inertial data and the closed form formulas characterizing the ambiguity accuracy are derived. Lastly, several simulated scenarios for navigation and tactical grade inertial systems are presented and these results are confirmed by an experimental study. The majority of the material presented in this chapter follows Skaloud (1998).

5.1 GPS Ambiguity Resolution Over Short Baselines

The capabilities of the state-of-the art ambiguity resolution algorithms are usually indicated by the observational time span over which the ambiguities can be resolved for the given receiver separation, satellite configuration and the set of observables (phase-only versus phase and range, single versus dual frequency), see for instance AFM (Counselman and Gourevitch, 1981), LSAT (Hatch, 1990), FARA (Frei, 1991), optimized search using Cholesky decomposition (Euler and Landau, 1992), LAMBDA (Teunissen, 1993), and DIAS (Wei and Schwarz, 1995). Under modest dynamics, successful ambiguity resolution is reported for single frequency phase and range measurements over time spans of tens of seconds to several minutes for a baseline up to 30 km using at least 6 satellites. Successful resolution can be achieved over longer baselines when dual frequency data is available. Conceptually, however, there is no difference between short and long baseline ambiguity resolution except for using more adequate models of the systematic errors in the measurements (e.g. tropospheric and ionospheric delays, orbital parameters)[1]. Considering this fact, the relative comparison between GPS only and INS/GPS ambiguity determination can be evaluated when considering only short baselines and single frequency measurements. The observation Equation (2.3) can therefore be rewritten as

$$\begin{aligned} D^T \Phi_i &= D^T A_i b_i + \lambda a \\ D^T p_i &= D^T A_i b_i \end{aligned} \tag{5.1}$$

---

[1] Practically, correct modeling of such errors represents a significant challenge.

where, again, the vectors Φ_i and p_i contain the m (number of satellites) single differenced (SD) carrier phase and code measurements respectively, D^T is the $(m-1) \; x \; m$ matrix transforming the SD to DD observables at epoch i, A_i represents the $m \; x \; 3$ SD design matrix that captures the receiver to satellite geometry, b_i denotes the vector of three unknown increments in the baseline, λ is the known wavelength, and the vector a contains the $(m-1)$ unknown DD ambiguities. Considering kinematic epochs $i=1, ..., k$, the system in Equation (5.1) has $3k+(m-1)$ unknowns, assuming no cycle slips, and thus the vector a remains an invariant. The system is theoretically observable in one epoch if $m \geq 5$ and k epochs give a redundancy of$(2k-1)(m-1)-3k$ (see Table 2.2). For k epochs, the system in Equation (5.1) can be rewritten in a more compact form as

$$y = Aa + Bb \tag{5.2}$$

where the y-vector denotes the differences between the anticipated and actual measurements, the b-vector contains the corrections to the baseline coordinates, the a-vector consists of the unknown carrier-phase ambiguities, and A and B are the corresponding design matrices. Considering that the measurements entering Equation (5.2) are corrupted by random errors, the solution to a and b can be sought as

$$\min \| y - Aa - Bb \| \quad a \in Z, b \in R. \tag{5.3}$$

However, the *integer* constraint on the ambiguities prevents the use of a classical least-squares (LS) estimator to obtain a one-step solution. Therefore, the solution to (5.3) is usually broken up into three steps (Kleusberg and Teunissen, 1996):

$$\begin{array}{ll}1.\ \min \| y - Ab - Bb \| \quad a, b \in R & \Rightarrow \hat{b}, \hat{a}, Q_{\hat{a}}, Q_{\hat{b}\hat{a}} \\ 2.\ \min\, (\hat{a} - a)^T Q_{\hat{a}}^{-1} (\hat{a} - a) & \Rightarrow \check{a} \\ 3.\ \check{b} = \hat{b} - Q_{\hat{b}\hat{a}} Q_{\hat{a}}^{-1} (\hat{a} - \check{a}) & \end{array} \tag{5.4}$$

where the symbol ‘ ˆ ‘ denotes the outcome of the first step, which is often referred to as the *float* solution (i.e. *float* baselines, *float* ambiguities), and the symbol ‘ ˇ ‘ is reserved for denoting the parameters after the ambiguities have been *fixed* to some integer. The third step is a straightforward computation following the solution of the first two steps. To obtain the solution of the first step, the LS approach is usually taken if no unmodeled effects have to be considered and the residual errors are assumed to be normally distributed.

To solve the second step, various ‘search’ methods have been developed and a number of them have already been mentioned. For comparisons of the most widely used ones, see Han (1997) or Hein and Werner (1995). One of the most sophisticated and well-documented approaches is the LAMBDA method introduced by Teunissen (1993). This method is not only effective computationally, but also guarantees that the second condition in the Equation system (5.4) is satisfied. It should be noted that the LS solution of Equation (5.3) will *always exist* but may not be of acceptable *quality*. To decide upon acceptance, an ambiguity validation process has to take place. Since the probability density function of the integer ambiguities is unknown, some empirical testing usually involving the *ratio* between the two best candidates is performed instead. In order to have the *ratio* sufficiently peaked around one solution, the *float* ambiguities must be of good accuracy. In other words, the successful validation mainly depends on the precision of the ambiguities described by the variance matrix $Q_{\hat{a}}$, which is a function of satellite geometry and the cofactor matrices of the observables. On the other hand, the vector $\hat{a}$ depends entirely on the data itself and the ratio of their cofactors. Later it will be shown how the inclusion of INS observables affects both $\hat{a}$ and $Q_{\hat{a}}$. Prior to that, the concept of appraising the ambiguity accuracy by a simple measure will be introduced.

Teunissen (1997b) presented an invariant called 'ambiguity dilution of precision (ADOP)' which is a uniquely defined scalar measure reflecting the accuracy of *float* ambiguities. ADOP is related to the square root of the determinant $|Q_{\hat{a}}|$ by

$$\text{ADOP} = \sqrt{|Q_{\hat{a}}|}^{\frac{1}{n}} \tag{5.5}$$

where n is the order of the ambiguity variance matrix. In a physical sense, the ADOP measures the volume of the ambiguity search space and thus is invariant for the whole class of admissible ambiguity transformations (e.g. the choice of the reference satellite, the de-correlating transformation in the LAMBDA method, etc.). Generally, ADOP depends on

a) satellite redundancy,
b) measurement accuracy,
c) observation epoch redundancy,
d) measurement type redundancy.

In the case of a single frequency carrier phase and code measurements, the covariance matrix for one epoch $Q_{\hat{a}}$ is expressed as (Teunissen, 1997a)

$$Q_{\hat{a}} = \frac{\sigma_{\Phi}^{2}}{\lambda^{2}} D^{T} [I_{m-1} + \frac{\sigma_{p}^{2}}{\sigma_{\Phi}^{2}} Q] D \,, \tag{5.6}$$

where Q will be defined later in Equation (5.14) and σ^{2}_{Φ} and σ^{2}_{p} represent the variances of phase and code measurements, respectively. The determinant of expression (5.6) can be found in closed form as

$$|Q_{\hat{a}}| = m \left(\frac{\sigma_{\Phi}^{2}}{\lambda^{2}} \right)^{m-1} \left(1 + \frac{\sigma_{p}^{2}}{\sigma_{\Phi}^{2}} \right)^{3} . \tag{5.7}$$

As can be seen from the above equation, the volume of the ambiguity search space does not depend on the receiver to satellite geometry. Generally it can be concluded that if a new type of observation relevant to the navigation solution is considered, the size of this determinant and thus also the ADOP will decrease while the chances for a successful ambiguity validation will increase. The following sections study how and under what conditions this is true when using inertial measurements.

5.2 INS/DGPS Ambiguity Resolution Over Short Baselines

Considering only the positioning component in Equation (2.4), an inertial system is a self-contained device which can deliver three-dimensional position as follows:

$$x = x_o + v_o t + \Delta x \tag{5.8}$$

where x_o and v_o are the vectors of the initial position and velocity, respectively, and Δx represents the three-dimensional coordinate differences measured by the INS. Δx thus expresses also the remaining dependence on the initial orientation as well as on the acceleration and angular rate observations made by the system along the vehicle trajectory.

5.2.1 Observation Model with Inertial Data

If Equation (5.8) is expressed as a correction to the observables for the current epoch and added to Equation (5.1), a common system of equations for the code, carrier-phase and inertial observation is obtained and given by

$$\begin{aligned} D^T \Phi_i &= D^T A_i b_i + \lambda a \\ D^T p_i &= D^T A_i b_i \\ \delta_i &= b_i - v_o t . \end{aligned} \tag{5.9}$$

where $\delta_i = \Delta x\text{-}\Delta x^0$, i.e. the discrepancy between the measured and approximate coordinate differences. The redundancy number for this system is $(m\text{-}1)(2k\text{-}1)\text{-}3$ which is $3(k\text{-}1)$ times larger than in the Equation (5.1).

When solving for b in the original system (5.1), code data are used and therefore the LS estimate of $\hat{b}$ and its variance matrix will be independent of the phase data and takes the form

$$\begin{aligned} \hat{b}_p &= N^{-1}A^T P\, p \\ Q_{\hat{b}_p} &= \frac{1}{q_p} N^{-1} \end{aligned} \tag{5.10}$$

where q_p denotes the weight of code measurements chosen as a reciprocal variance $q_p=1/\sigma_p^2$, $N=A^TPA$ symbolizes the system of normal equations and P is an orthogonal projector. Knowing the structure of the matrix D, the projector P can be expressed explicitly as

$$P = D(D^TD)^{-1}D^T = I_m - \frac{1}{m}e_m e_m^T \tag{5.11}$$

where e_m is a m-vector having only unit elements.

In the cases when information about v_o is unavailable, the inclusion of inertial data will have no influence on the location of the *float* parameters estimated from system (5.9). In other words, the estimation of $\hat{b}$ for this system will be identical to the solution (5.10). However, the knowledge of v_o and its variance can be obtained using different types of GPS observations, namely range-rate and phase-rate measurements. Since these measurements are not ambiguous, they are available from the receiver as long as phase lock is maintained and can be used to obtain velocity information; see Bruton et al. (1999a). Combining these measurements with the inertial data results in a smoother estimate of v_o with an accuracy that is generally a function of vehicle dynamics. Moreover, in the case of land-vehicle applications, this information is perfectly known when a vehicle stops ($v=0$). Thus, considering some a priori knowledge about v_o, the LS estimate for the *float* baseline $\hat{b}$ from the system of Equations (5.9) can be expressed as:

$$\begin{aligned} \hat{b}_{p,\delta} &= [N^{-1}A^{T}Pp\,q_{p} + (\delta + v_{o}t)q_{\delta}]/(q_{p} + q_{\delta}) \\ Q_{\hat{b}_{p,\delta}} &= [N^{-1}q_{p} + I_{3}q_{\delta}]/(q_{p} + q_{\delta})^{2} \end{aligned} \tag{5.12}$$

where $q_p=1/\sigma^2_p$, $q_\delta=1/\sigma^2_\delta$ essentially represent the weights of the measurements. Once the ambiguities are *fixed*, the *fixed* baseline solution $\check{b}$ and its variance matrix are given by:

$$\begin{aligned} \check{b}_{p,\delta} &= \frac{N^{-1}A^{T}P[(\Phi - \lambda\check{s})q_{\Phi} + p\,q_{p}] + (\delta + v_{o}t)q_{\delta}}{q_{\Phi} + q_{p} + q_{\delta}} \\ Q_{\check{b}} &= [N^{-1}(q_{\Phi} + q_{p}) + I_{3}q_{\delta}]/(q_{\Phi} + q_{p} + q_{\delta})^{2} \end{aligned} \tag{5.13}$$

where $\check{s}$ is a vector containing the SD ambiguities which are related to the integer DD ambiguities by $\check{a} = D^{T}\check{s}$.

5.2.2 The Shape of the Ambiguity Search Space

All the necessary information about the ambiguity search space is captured by the covariance matrix Q_a. In the following, Q_a will be derived for the case of GPS code measurements combined with coordinate differences from INS.

Once the *float* baseline has been computed, the least-square ambiguities follow by applying the error propagation to the first equation of system (5.9), which results in

$$\begin{aligned} \hat{a} &= \frac{1}{\hat{\lambda}} D^T (\Phi - A\hat{b}_{p,\delta}) \\ Q_{\hat{a}_{p,\delta}} &= \frac{1}{\hat{\lambda}^2} D^T \left[\frac{1}{q_\Phi} I_{m-1} + \frac{q_p}{(q_p + q_\delta)^2} Q + \frac{q_\delta}{(q_p + q_\delta)^2} AA^T \right] D \end{aligned} \tag{5.14}$$

where Q is an orthogonal projector defined as $Q=A(A^TPA)^{-1}A^T$. If only GPS observations are available, the above expression for the ambiguity covariance matrix collapses to Equation (5.6) as expected.

5.2.3 The Volume of the Ambiguity Search Space

Recall that in Section 5.1 it was mentioned that the success of the ambiguity resolution process strongly depends on the accuracy of the *float* ambiguities, which is described by Q_a.

Also, the concept of characterizing this accuracy by an invariant which corresponds to the determinant of Q_a (Teunissen et al., 1996; Teunissen, 1997b) was presented. To gain some insight on how the accuracy of the ambiguities is affected by the inclusion of inertial observables, a closed-form expression for the determinant of Q_a is derived in the following. Starting with Equation (5.14), the determinant of Q_a can be expressed as

$$\begin{aligned} \left|Q_{\hat{a}_{p,\delta}}\right| &= \left|\frac{1}{\lambda^2} D^T \left[k_1 I_m + k_2 Q + k_3 A^T A\right] D\right| \\ &= \left(\frac{k_1}{\lambda^2}\right)^{m-1} \left|D^T D\right| \left|I_{m-1} + \frac{k_2}{k_1} D^+ [QD + \frac{k_3}{k_1} A^T AD]\right| \end{aligned} \tag{5.15}$$

where the coefficients k_1, k_2, k_3 correspond to the reciprocal weights of the measurements, and $D^+ = (D^T D)^{-1} D^T$ is the pseudo-inverse of *D*. The matrix $D^T D$ has main diagonal elements equal to 2 while all other entries are 1. A matrix of this type having the size of *(m-1)(m-1)*, has one eigenvalue equal to *m*, while all other *(m-2)* eigenvalues are equal to 1. Hence, $|D^T D| = m$. Using the 'matrix swap' relation $|I + MN| = |I + NM|$, one obtains

$$\begin{aligned} \left|Q_{\hat{a}_{p,\delta}}\right| &= m\left(\frac{k_1}{\lambda^2}\right)^{m-1} \left|I_{m-1} + \frac{k_2}{k_1} QP + \frac{k_3}{k_1} AA^T P)\right| \\ &= m\left(\frac{k_1}{\lambda^2}\right)^{m-1} \left|I_{m-1} + \left[\frac{k_2}{k_1} A(A^T PA)^{-1} + \frac{k_3}{k_1} A\right] A^T P\right| \end{aligned} \tag{5.16}$$

considering that $DD^+ = P$ and $Q = QP = PQ$ for orthogonal projectors. By applying the 'matrix swap' relation again, we obtain

$$
\begin{aligned}
\left|Q_{\hat{a}_{p,\delta}}\right| &= m\left(\frac{k_1}{\lambda^2}\right)^{m-1}\left|I_3+\frac{k_2}{k_1}I_3+\frac{k_3}{k_1}A^TPA\right| \\
&= m\left(\frac{k_1}{\lambda^2}\right)^{m-1}\left(\frac{k_1+k_2}{k_1}\right)^3\left|I_3+\frac{k_3}{k_1+k_2}A^TPA\right| \qquad (5.17) \\
&= m\left(\frac{\sigma_\Phi^2}{\lambda^2}\right)^{m-1}\left(1+\frac{q_p\,q_\Phi}{(q_p+q_\delta)^2}\right)^3\left|I_3+\frac{q_\Phi q_\delta}{(q_p+q_\delta)^2+q_p q_\Phi}N\right|
\end{aligned}
$$

where the normal equations $N=A^TPA$ express the dependence on the receiver-satellite geometry. If the weights of the inertial measurements decrease toward zero after some time, the geometry-dependent term vanishes in the limit and the expression (5.17) reduces to equation (5.7). Denoting the scalar term in front of the matrix N as K in Equation (5.17), this expression can be rewritten as

$$
\left|Q_{\hat{a}_{p,\delta}}\right| = m\left(\frac{\sigma_\Phi^2}{\lambda^2}\right)^{m-1}\left(1+\frac{q_p\,q_\Phi}{(q_p+q_\Phi)^2}\right)^3 \cdot \left(aK^3+bK^2+cK+1\right) \qquad (5.18)
$$

where $a=|N|$, $b=(n_{11}n_{33}+n_{22}n_{33}+n_{11}n_{22})$, $c=Tr(N)$, and $K=q_\Phi q_\delta/[(q_p+q_\delta)^2+q_p q_\Phi]$.

Generally, this relation shows that the volume of the ambiguity search space decreases by including the inertial measurements as long as the accuracy of these observables is not significantly poorer than the accuracy of the GPS observables. The expression (aK^3+bK^2+cK+1) is a 3rd order polynomial, which reaches its maximum or minimum when

$3aK^2 + 2bK + c = 0$. The coefficients in the matrix N are essentially a linear combination of the known structure of the matrix P (expression 5.11) and the direction cosines of the matrix A which are within the interval $[0,1]$. By choosing coefficients a, b, c for extremely good and bad cases of the GPS satellite configuration, the maximum and minimum of expression (5.18) can be found.

5.3 A Simulation Study

The substitution of Equation (5.18) into (5.5) defines the ADOP for the INS/DGPS observation model (5.9). To obtain a relative comparison with the 'DGPS only' ADOP, where $|Q_a|$ is defined by Equation (5.7), only the measurement accuracies (i.e., weights q_p, q_Φ, q_δ) need to be known. The accuracy of GPS code and phase observations can be considered more or less time invariant, while the weights of the inertial measurements exhibit a rather complex-time dependent structure. However, since the general structure of the INS error model is usually well known (e.g., Britting, 1971, Farell, 1976), these weights can be computed by covariance propagation. In the following, computer simulations were conducted to display the volume of the ambiguity search space over time in different scenarios and different inertial systems.

The two inertial systems to be considered in the simulations are a navigation-grade and a tactical-grade IMU, respectively. The parameters used in the 15-state dynamic error model are shown in Table 5.1. Figures 5.2 and 5.3 display the development of ADOP in time for a configuration of 5 satellites when using both systems in comparison to GPS only. For a fixed set of error model parameters, the accuracy of the INS navigation output strongly depends on the vehicle dynamics. Therefore, the values of ADOP in Figures 5.2 and 5.3 are plotted for 3 different values of vehicle acceleration from 0.01 to 1 m/s^2. In all cases, the function of ADOP is also plotted for the maximal and minimal values obtained from the dependence on the satellite to baseline geometry.

Table 5.1. Error model for GPS and INS observations.

Parameter		**Navigation-Grade IMU**	**Tactical-Grade IMU**
DGPS Observable Accuracy (1σ)	Code	0.6 m	
	Phase	0.003 m	
INS Initial Uncertanities (1σ)	Position	0.4 (DD GPS, float amb.)	0.6 (DD GPS, float amb.)
	Velocity	0.02 m/s (Doppler)	0.02 m/s (Doppler)
	Attitude	0.03°	0.35°
	Accel. Bias	50 µg	200 µg
	Gyro Drift	0.01°	1°
Spectral Densities	Position	0.0 m/√Hz	0.0 m/√Hz
	Velocity	0.001 m/s/√Hz	0.01 m/s/√Hz
	Attitude	0.001 °/h/√Hz	0.05 °/h/√Hz
	Gyro Drift	4e-06 °/h/√Hz	0.1 °/h/√Hz
	Accel. Bias	3e-06 °/h/√Hz	4e-03 °/h/√Hz
Correlation Time	Gyro Drift	2 h	60 s
	Accel. Bias	2 h	60 s

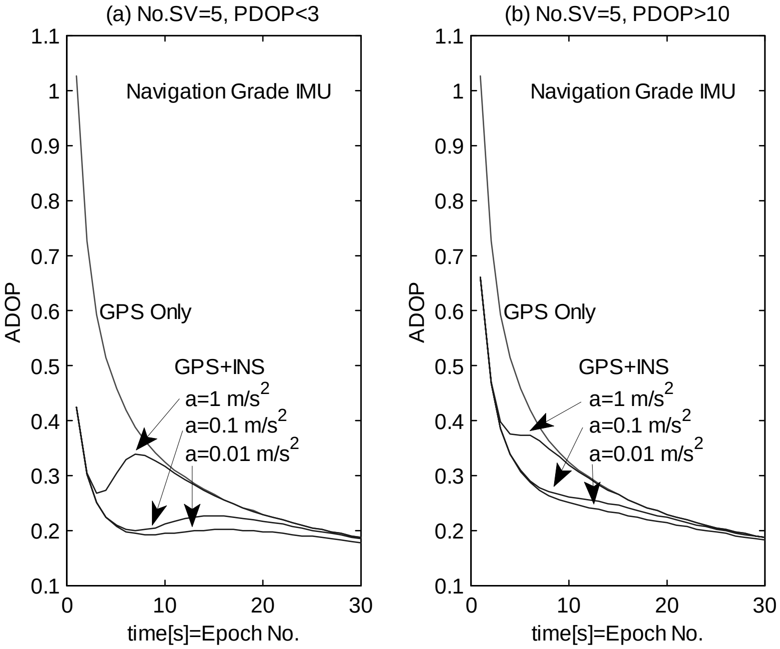

Figure 5.2. The ADOP without and with a navigation-grade INS in different dynamics and (a) good geometry, (b) poor geometry.

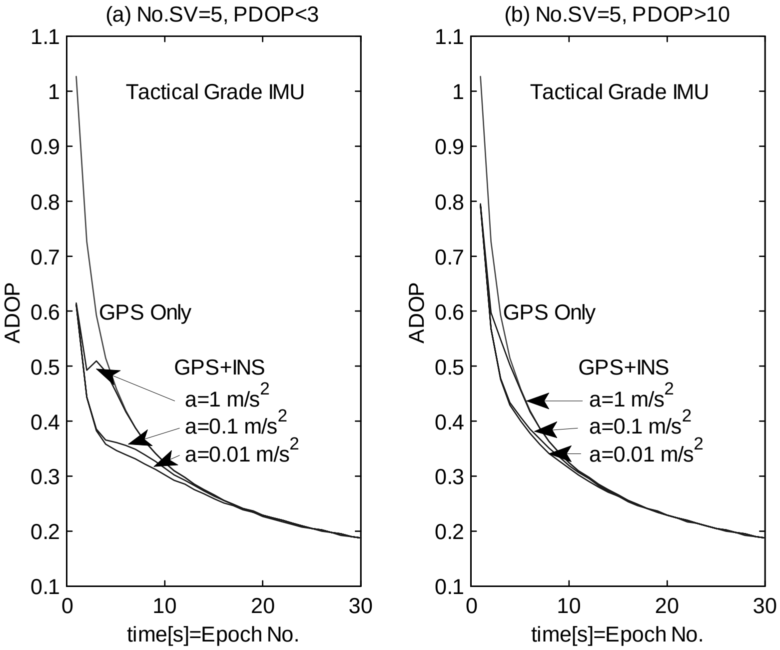

Figure 5.3. The ADOP without and with a tactical-grade INS in different dynamics and (a) good geometry, (b) poor geometry.

Figures 5.2 and 5.3 clearly demonstrate the effect of including INS data for ADOP reduction which corresponds directly to a better accuracy of the *float* ambiguities. The improvements are considerably more pronounced for the navigation-grade system than for the tactical-grade IMU where only marginal improvement can be obtained. In general, a navigation-grade system can deliver coordinate differences that are superior to those obtained from GPS measurements with unknown (float) ambiguities over a time periods of up to 30 seconds. Their inclusion into the estimator reduces the ADOP significantly. This, in turn, has a positive effect on the ambiguity validation problem, since the resulting *float* ambiguities are of a better accuracy and the chances of finding a peaked solution improves.

Although the final validation procedure requires actual data for evaluating the norms $(\hat{a}-a)^T Q_a^{-1}(\hat{a}-a)$, the relative benefits of improving the accuracy of float ambiguities (i.e., reducing the cofactors in Q_a) can be explained as follows. Consider for an instance a case where ADOP = 0.3 is a sufficient value for validating the ambiguities. Following the scenario in Figure 5.2-a, 12 epochs of GPS data are needed to achieve this value. When using also the observations from a navigation-grade IMU, the same result can be obtained in 3 seconds when a favorable geometry exists. For the case of poor geometry, about 6 seconds of data and rather benign dynamics are sufficient for ambiguity validation (Figure 5.2-b). On the other hand, incorporating observations from a tactical-grade IMU would not speed up the validation process for this particular situation (i.e., Figure 5.3).

Appendix B contains figures of two more scenarios for the navigation-grade IMU and cases where 4 and 6 satellites are in view, respectively. It should be noted that with the availability of a high quality inertial system, it is possible in theory to determine the ambiguities by observing only 4 satellites. However, as shown on Figure B.1, the likelihood of a successful validation is relatively small due to existence of large ADOP values.

Another possibility of expressing the improvements due to the inclusion of inertial measurements is to compare the absolute volumes of the ambiguity search spaces for both observation models. Figure 5.4 shows the relative reduction of the GPS ambiguity search space when using a navigation-grade IMU and different levels of dynamics. As can be seen from this figure, the inclusion of inertial data reduces the volume of the search space about

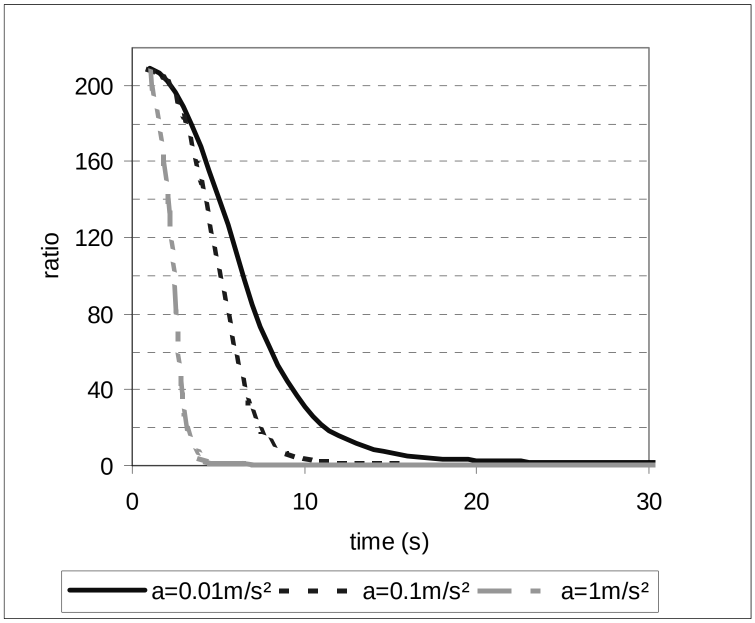

Figure 5.4. Reduction in the volume of the ambiguity search space due to inclusion of a navigation-grade IMU as a function of dynamics and time for 5 satellites in view.

50 times over three seconds even for the worst scenario considered. After approximately 30 seconds, the ratio approaches unity and the volume of the ambiguity search space (and thus also the ADOP) becomes more and more driven by the GPS measurements only, although a small improvement due to the inertial data will always remain.

In the tightly coupled INS/DGPS integration, the data are processed similarly to the observation model (5.9) analyzed in the simulations. Therefore, the results presented can also be interpreted as the advantages of the centralized over the decentralized filtering with respect to the process of ambiguity determination. Summarizing these results, the level of this improvement strongly depends on the quality of the inertial system, the accuracy of the initial velocity and the level of dynamics, while the dependence on receiver-to-satellite geometry is less significant. Since the improvements are most significant over short time intervals, the applications mostly benefitting from the inclusion of INS data are those requiring instantaneous or near instantaneous ambiguity resolution. This will always be the case in real-time mapping applications.

CHAPTER 6

OPERATIONAL ASPECTS

This chapter discusses additional topics to be considered when designing an airborne georeferencing system. Although the nature of these problems is more practical, their solution provides considerable challenges at the operational and hardware levels. The subjects to be discussed are:

- sensor placement,
- sensor synchronization,
- system calibration,
- initial alignment.

In many cases, the significance of the ‘practical’ issues listed above may equal or exceed the importance of software development for optimal trajectory estimation. However, the goal of this chapter is not to provide an exhaustive study of these subjects, but to rather demonstrate their importance in particular cases for which data sets are available.

6.1 Sensor Placement

The optimal placement of all sensors in an airborne carrier is a non-trivial task. A poor sensor mount is most likely to alter the performance of the whole system and errors of such type may be very difficult to correct for. The requirements on sensor placing are usually motivated by two objectives:

- to minimize the effect of calibration errors on lever-arm corrections
- to avoid any differential movements between sensors.

Addressing the first objective, short distances between sensors reduce the impact of uncertainties in the lever-arm corrections (El-Sheimy, 1996). This especially affects the positioning component of direct-georeferencing. On the other hand, small differential movements mainly alter the attitude performance.

Considering first the lever-arm correction problem, the constraints on placing the sensors in airborne carries are more restrictive as compared to land vehicles. For instance, the mount used in the VISAT system (El-Sheimy, 1996) fixes all sensors next to each other on the roof of the vehicle. Such a configuration is not quite possible to be adopted in an aircraft, since the imaging component has to be oriented to look downward while the GPS antenna has to be mounted on top of the fuselage. Hence, a somewhat larger distance between these two devices will always exists and can be minimized only by placing them underneath each other.

An optimal place for an inertial system would then be somewhere between these two devices, but most likely directly on the top of the camera for the reasons discussed in the following.

Of the problems of lever arm corrections and differential movements between the sensors, the latter is the more difficult to overcome. Rigidly mounting the camera and the inertial system to a solid and common structure solves this problem only partially, because the sensors in either of these devices may not be rigidly connected to their chassis in order to dampen vibrations (i.e., to prevent the blur of the imagery in an aerial camera). However, the dampening responses are the most likely ones to differ between devices, thus causing inevitable attitude errors in a vibrating environment such as an aircraft. The seriousness of this problem has been realized in the first commercially available product for direct georeferencing POS/DG (Position and Orientation System for Direct Georeferencing, Applanix™) in which it was solved by mounting a small, tactical-grade IMU directly to the body of the camera (Figure 6.1). Although this solution seems to give satisfactory results,

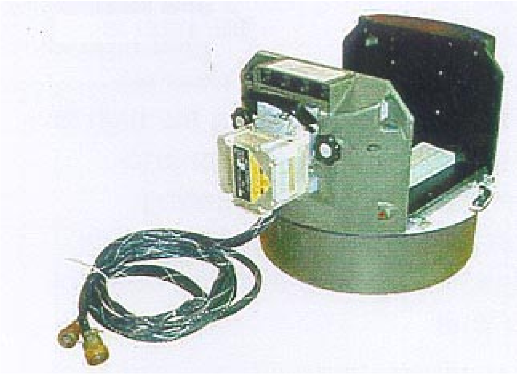

Figure 6.1. RC 20 Aerial Camera with POS/DG (Applanix™ advertisement)

using the same approach to accommodate heavier navigation-grade systems would most likely exceed the permissible load of the camera holder.

Another possible solution is to design a solid structure, isolate it from vibrations and mount both devices to its frame. This approach has been taken by Mostafa et al. (1998) when designing a holder for a digital camera and a navigation-grade strapdown INS. Since data sets were collected with and without a vibration dampener while using the same INS and the same type of an aircraft, the effect of vibration on the inertial output can be quantified. Figure 6.2 depicts the velocity noise from the *x* and *y* accelerometers during a 10 minute cruising period. As can be seen from this figure, the noise level is about 1.5 to 2 times smaller when

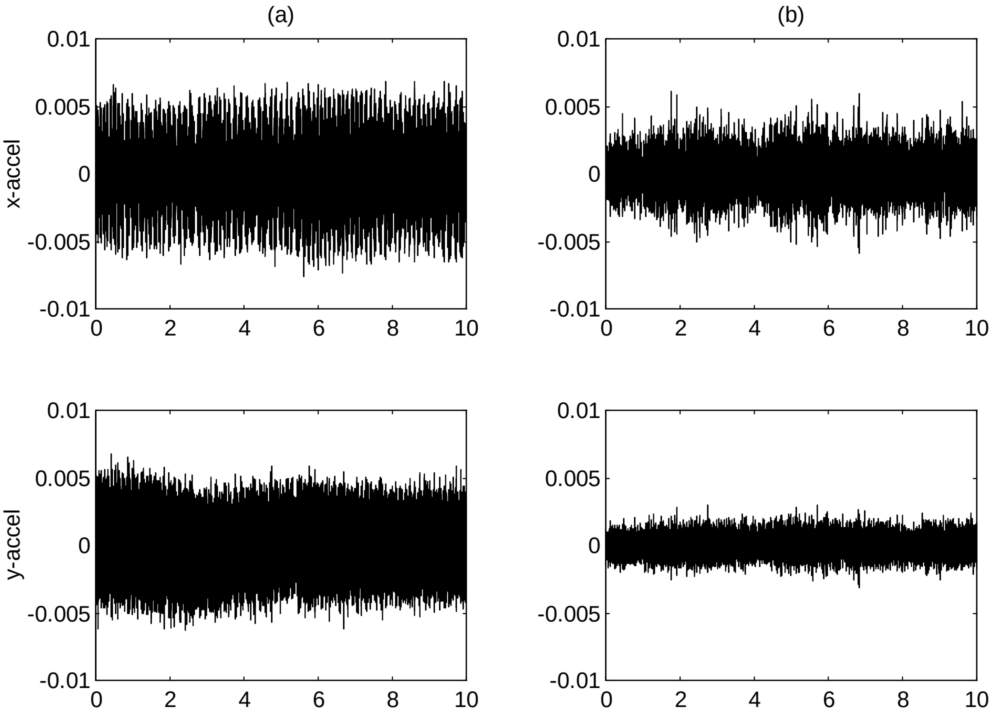

Figure 6.2. Comparison of the velocity noise in the *x* and *y* channels of the LTN 90-100 (a) without and (b) with vibration dampening using a special mount.

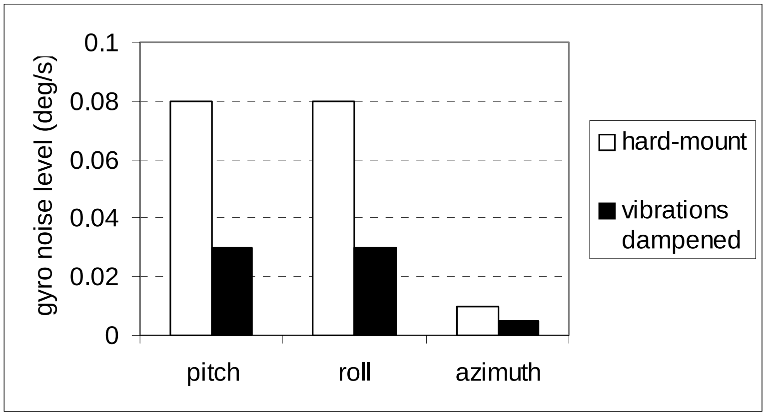

Figure 6.3. Comparison of the gyro noise level in the LTN-90-100 with and without vibration dampeners.

the vibration dampener is used. Using the noise estimation approach as described in Chapter 4, the level of the noise in the gyro output was estimated in both cases. The results are plotted in Figure 6.3. Again, the noise level is approximately twice as small when vibration dampeners are used.

6.2 Sensor Synchronization

The requirements for time synchronization between the INS, the GPS and the imagery data streams increase with accuracy requirements and vehicle dynamics. If not handled properly, they will be a serious source of errors. Considering Equation (2.1) for direct georeferencing, errors in the synchronization directly affect the determination of the vehicle trajectory in the translation vector $\boldsymbol{r}^{m}_{ins/gps}(t)$ as well as the rotation matrix $\boldsymbol{R}_{b}^{m}(t)$. Since the severity of this error source increases with the platform speed and dynamics, its mitigation is important

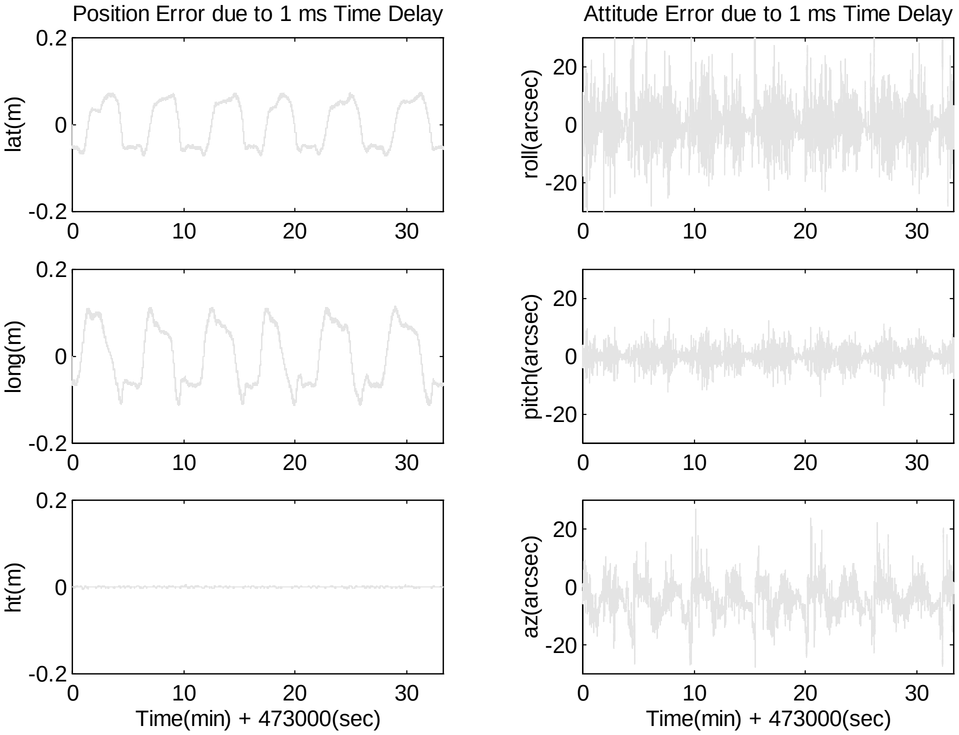

Figure 6.4. Error in navigation parameters due to synchronization error of 1 ms. (Test data as described in Chapter 7).

especially when using airborne carriers. A practical demonstration of this fact is given in Figure 6.4 where the effect of a 1 ms (milisecond) delay is projected on aircraft position and orientation, respectively. As can be seen from the figure, the 1 ms synchronization error jeopardizes both position and attitude parameters during the survey mission. The along-track position error can be easily obtained by multiplying the delay by aircraft velocity (i.e., a 1 ms delay causes a 10 cm along track position error for the aircraft velocity of 360 km/h). Its influence on height determination is rather negligible once cruising altitude is reached. Although the orientation dynamics lack a simple pattern, the impact of a delay on the attitude parameters can again be quantified by multiplying the delay by the rotation rate. Hence, considering a 10 deg/s rotation rate, a 1 ms delay causes an orientation error of 36".

The effect of imperfect synchronization seems to be less critical for airborne gravity surveys by strapdown INS/DGPS. Typical accelerations are about ±1000 mGal/s (1 mGal = 10^{-5} m/s^2) with extreme values of about ± 3000 mGal/s (Glennie, 1999). That means that a time delay of 1 ms between the INS and GPS data streams causes a 1 mGal error which in most cases is below the system noise level.

El-Sheimy (1996) analyzed the synchronization errors when using a decentralized hardware configuration consisting of an INS, a GPS receiver, digital cameras and a data logging computer. The error sources can be divided into three main categories as described in Table 6.1 below.

Table 6.1. Time synchronization error sources.

General Error Source	**Specific Error Source**	**Possible Mitigation**
Internal hardware delay	A/D conversion	Specified by the manufacture A constant delay may be calibrated
	Internal DSP processing	
	Transmission to communication ports	
Data transmission delay	Communication board/protocol	A constant delay may be calibrated
Registration delay	Computer clock reading	Low level coding with real time clock Multi I/O timing board
	Computer IRQ priorities	

In general, airborne applications require a centralized synchronization approach via a multi I/O timing board to keep the registration delay under the 1 ms level. When such hardware is implemented, the quality of the synchronization is then mainly affected by the delays due to transmission and processing before measurements are registered.

Addressing first only inertial systems, a constant value of the system delay (i.e., time difference between a measurement occurrence and actual measurement output) is usually provided by the manufacturer. Such a number accounts for all internal processing delays due to A/D conversion, filtering, data transmission etc., and its value can be rather large (e.g. 50-60 ms for the LTN90-100). Also given as a constant, it may vary in time if some form of adaptive filtering is implemented. The transmission delay needs to be calibrated.

The GPS data stream presents less of a problem, because these measurements are already time-tagged internally by the receiver clocks.

Synchronization errors in camera exposure epochs can vary greatly. Even if the registration of the shutter pulse is performed internally by the GPS receiver, the transmission delay will always be present. Moreover, the event marked as an exposure may correspond to different stages of shutter opening or closing. This problem may be quite significant especially for cameras of older design where the shutter marker has been installed subsequently. Nevertheless, as long as the delay in registering camera exposure remains a constant it may be estimated within the calibration procedure as described in the following section.

6.3 System Calibration

The calibration of all sensors used in the integrated system is an essential step prior to a survey mission. System calibration can be divided into two parts: calibration of individual sensors and calibration between sensors. The calibration of the individual sensors may include the calibration for parameters of interior orientation, INS calibration for constant drifts, biases or scale factors, GPS antenna multipath calibration, etc. An extensive literature exists on each of these topics. Calibration between sensors involves determining the relative location and orientation between the camera and the navigation sensors as well as the constant synchronization offset due to data transmission and internal hardware delays. Some practical issues concerning this subject will be discussed in the following.

The calibration for relative location and orientation between sensors has been previously described for digital cameras and land-vehicle applications by El-Sheimy (1996), for frame-based imagery in the airborne environment by Skaloud et al. (1994), and for pushbroom scanners by Cosandier et al. (1994). Although each of these cases differ in details, the main concept remains the same. Considering Equation (2.1) of direct georeferencing, the translation offset ($\boldsymbol{a}^b$) between sensors is measured by conventional survey methods and the orientation offset ($\boldsymbol{R}_c^{\,b}$) is determined by comparing $\boldsymbol{R}_b^{\,m}$ and $\boldsymbol{R}_c^{\,m}$ where the latter is computed from photogrammetric triangulation using overlapping imagery and ground control points. Since the parameters $\boldsymbol{a}^b$ and $\boldsymbol{R}_c^{\,b}$ are directly used in this equation, they need to be determined with an accuracy that at least matches the one specified in Table 1.1. The determination of the vector $\boldsymbol{a}^b$ presents less of a problem, since an accuracy of a few centimeters is usually sufficient and can be achieved by using a total station for instance. In contrast, determination of $\boldsymbol{R}_c^{\,b}$ is a tedious process, because it requires the determination of $\boldsymbol{R}_c^{\,m}$ with the same accuracy as $\boldsymbol{R}_b^{\,m}$ in order to fully exploit the quality of the navigation sensors. It should be noted that, especially for digital cameras, this may become the limiting factor for the overall accuracy when transforming INS/DGPS attitude to the camera-frame. The following discussion gives some suggestions on how to improve the accuracy of $\boldsymbol{R}_c^{\,b}$ using INS/DGPS and a given photogrammetric block with ground control points.

1. The formula for obtaining $\boldsymbol{R}_c^{\,b}$ should have the form:

$$\boldsymbol{R}_{\boldsymbol{c}}^{\boldsymbol{b}}(t_i) = \left[\boldsymbol{R}_{\boldsymbol{l}}^{\boldsymbol{c}}(t_i)\,\boldsymbol{R}_{\boldsymbol{b}}^{\boldsymbol{l}}(t_i)\right]^T \tag{6.1}$$

   where t_i corresponds to the exposure epoch of an image contained in the block. Assuming a constant misorientation, an average value of this matrix can be used for the transformation of the attitude data. Since the parameters of exterior orientation are better estimated in the middle of the block, only those images should be used to determine the values. It should be noted that expressing the differential rotation matrix in the body frame (as in Equation 6.1) rather than in the local-level frame, assures its independence from the aircraft attitude. Should it be otherwise, the differential rotation matrix would appear to be time-varying in the local-level axes, as a function of aircraft orientation.

2. Although the photogrammetric model is flexible with regard to the choice of a coordinate system, the chosen map projection has to represent a system of curvilinear geographic coordinates and also has to be conformal to assure compatability with the INS/DGPS attitude. A Transverse Mercator (TM) projection with a choice of the central meridian in the middle of the flight area fulfills this condition and also minimizes the azimuthal correction due to meridian convergence. However, the azimuthal correction has to be applied in order to transfer $\boldsymbol{R}_c^m$ to $\boldsymbol{R}_c^l$. When the sequence of rotations is reversed in the bundle adjustment (i.e., κ-φ-ω), the azimuthal correction can be directly subtracted from κ (i.e., the rotation about the z-axis).

3. If GPS ambiguities can be fixed, the INS/DGPS derived position of the camera perspective center should be used in the bundle adjustment. Fixing the camera perspective center in space provides de-correlation between the parameters of exterior orientation which subsequently results in a better estimate of $\boldsymbol{R}_c^l$ and thus $\boldsymbol{R}_c^b$. Moreover, it also allows to refine the calibration of the camera focal-length at the same time.

4. Since the accuracy of $\boldsymbol{R}_b^l$ also directly affects the determination of $\boldsymbol{R}_c^b$ in Equation (6.1), the inertial system should be well aligned prior to acquiring the first strip of images of the photogrammetry block. The problems related to the initial alignment are described in the following section.

The method of calibrating $\boldsymbol{R}_c^b$ as described above can also be used to estimate a constant synchronization error between the navigation data and the camera exposure. The matrix $\boldsymbol{R}_b^l(t)$ is substituted into Equation (6.1) as $\boldsymbol{R}_b^l(t+\Delta)$, where Δ is varied in small steps up ±100 ms. Then, the standard deviations of the $\boldsymbol{R}_c^b$ orientation angles are evaluated for each Δ and the maximal correlation shift is computed. An example of this is plotted in Figure 6.5, where the relative synchronization error between the imagery and navigation data streams is found to be 85 ms.

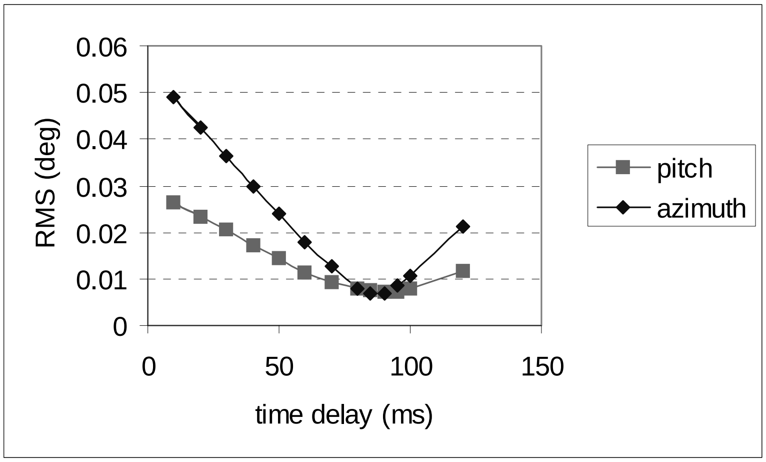

Figure 6.5. Estimation of the relative synchronization error by means of differences between $\boldsymbol{R}_b^l(t)$ (INS/GPS) and $\boldsymbol{R}_c^l$ (photogrammetry).

6.4 Initial Alignment

The alignment process determines the initial orientation matrix $\boldsymbol{R}_b^l$ of an inertial system. It precedes the survey mission and is generally done in two stages: coarse and fine alignment. Considering a stationary environment, the coarse alignment estimates the attitude parameters approximately using the raw sensor output and the assumption that nothing but Earth rotation and gravity are sensed. This information is then refined in the fine alignment using a Kalman filter with 'misalignment states' and zero velocity as updates. This procedure usually takes 10-15 minutes for a navigation grade IMU to achieve about 1'-3' accuracy in azimuth and 30"-60" accuracy in roll and pitch (Liu, 1992). In an integrated system, the alignment uncertainties are further refined during the kinematic periods using GPS position and velocities as external measurements. Among other factors, the level of improvement during these periods mainly depends on the level of platform dynamics.

From an operational point of view, the 10-15 minute period of static alignment is quite impractical. Moreover, if executed with the aircraft engines running[1], its accuracy deteriorates due to vibrations. Furthermore, inertial systems of poorer accuracy (i.e., tactical-grade INS) cannot be aligned in static mode, because the level of sensor noise in these systems completely masks the needed signal coming from Earth rotation. All of these arguments speak for a dynamic alignment which can be executed quickly, and which

---

[1] Since the power for an inertial system is usually drawn directly from the aircraft, its engines have to be started prior to the initialization of the inertial system.

guarantees a sufficient accuracy level prior to the georeferencing process. The following discussion will show that dynamic alignment is feasible if aircraft maneuvers are executed in such a way that accelerations in all channels result.

To illustrate the motivation for introducing aircraft maneuvers for obtaining better alignment accuracy, the equation for velocity errors in the local-level frame will be discussed in detail. It is of the form

$$\begin{aligned} \delta\dot{v}_e &= f_z\varepsilon_n - f_n\varepsilon_z + b_e \\ \delta\dot{v}_n &= -f_z\varepsilon_e + f_e\varepsilon_z + b_n \\ \delta\dot{v}_z &= f_n\varepsilon_e - f_e\varepsilon_n + b_z \end{aligned} \tag{6.2}$$

where the subscripts *e*, *n*, *z* denote east, north and up components, *f* is the specific force measurement, ε is the misalignment error and *b* is the accelerometer bias. Equation (6.2) indicates that the velocity error in a particular channel is generated by misalignment errors coupled with specific force measurements in the other two channels. Since f_z is always large, due to gravity, the velocity errors due to ε_e and ε_n can be observed continuously. In contrast, f_e and f_n have nonzero values only when the aircraft is accelerating in the horizontal plane. Thus, the accuracy of determining ε_z and the separation of errors in the different channels mainly depends on the extent of horizontal maneuvers. Overall, if aircraft maneuvers provoke sufficient horizontal acceleration, the misalignment uncertainties become quickly observable through the velocity errors and can be estimated by a filter using DGPS velocity updates. An example of this effect will be shown in the following.

Figure 6.6 depicts a flight trajectory with heading maneuvers indicated by the arrows. On board the aircraft were two INS/DGPS systems: a navigation-grade LTN-90-100, loosely integrated with a geodetic GPS receiver, and a tactical-grade IMU, C-MIGITS II, tightly integrated with a C/A code GPS receiver. The performance of the latter was to be tested while the navigation-grade INS/DGPS system served as a reference (for a detailed analysis and test description, see Skaloud at al., 1997). The flight started with the static alignment of the LTN-90-100 whose attitude was then transferred to the C-MIGITS II[2]. After take-off, a first figure-eight pattern was flown to improve the 'transfer' alignment of the C-MIGITS II, since a small orientation difference exists between both systems due to uncertainties in their housing. Two flight lines were then flown. After that, the C-MIGITS II was re-initialized and a dynamic alignment was performed while executing two figure-eight maneuvers to provide

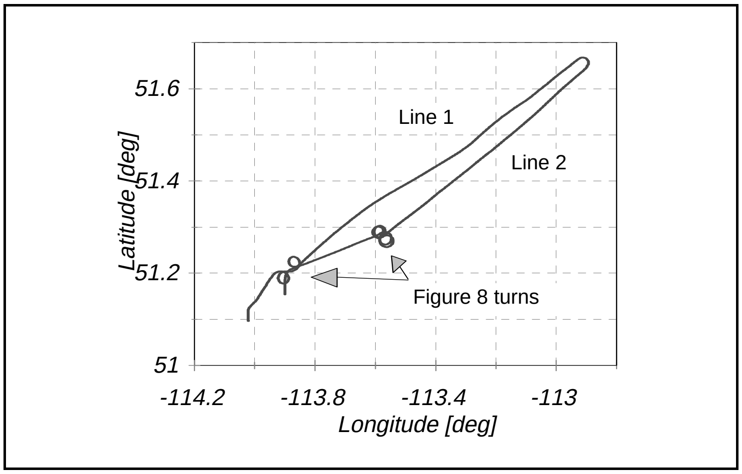

Figure 6.6 Test flight trajectory with maneuvers to provoke horizontal acceleration of the aircraft.

---

[2] The high noise level of the C-MIGITS II IMU prevents a static alignment.

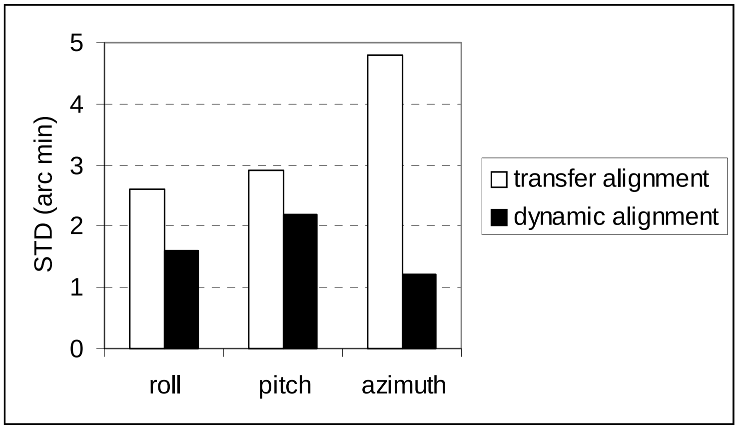

Figure 6.7. Comparison of alignment accuracies.

horizontal aircraft acceleration. Figure 6.7 depicts the C-MIGITS II attitude errors before and after the dynamic alignment using the LTN-90-100 as reference. Comparing the statistics before and after the in-flight alignment, it is apparent that the attitude performance is considerably improved with respect to the transfer alignment. This is especially obvious for the azimuth where according to Equation (6.2) the largest improvement should be expected. This also suggests that repeating the in-flight alignment regularly after flying at constant speed and azimuth for longer periods of time results in better attitude accuracy. The overall orientation performance achieved in this test corresponds to the attitude quality delivered by a tactical-grade inertial system with quartz rate sensors.

It should be noted, however, that although the INS/DGPS integration never stops refining the initial alignment, the accuracy of this process is limited by other factors apart from the dynamics. Two such limitations are directly apparent from Equation (6.2). First, the estimation process depends on the accuracy of the GPS velocity. Hence, for applications with high accuracy requirements the determination of GPS velocity needs to be handled with special care (for a comparison on filtering methods for high precision GPS velocity determination, see for instance Bruton et al., 1999a). Second, the tilt error is coupled with the accelerometer bias. In other words, the quality of the accelerometers indirectly affects the attitude accuracy, and therefore, their quality should correspond to the quality of the gyroscopes. An additional limiting factor comes from the uncertainties in the anomalous gravity field which appears as a disturbing signal in the accelerometer output. Although such an error source could be negligible at some geographical locations, a rough gravity field may cause substantial attitude errors (Figure 6.8) and limit the accuracy of the georeferencing process in such an environment.

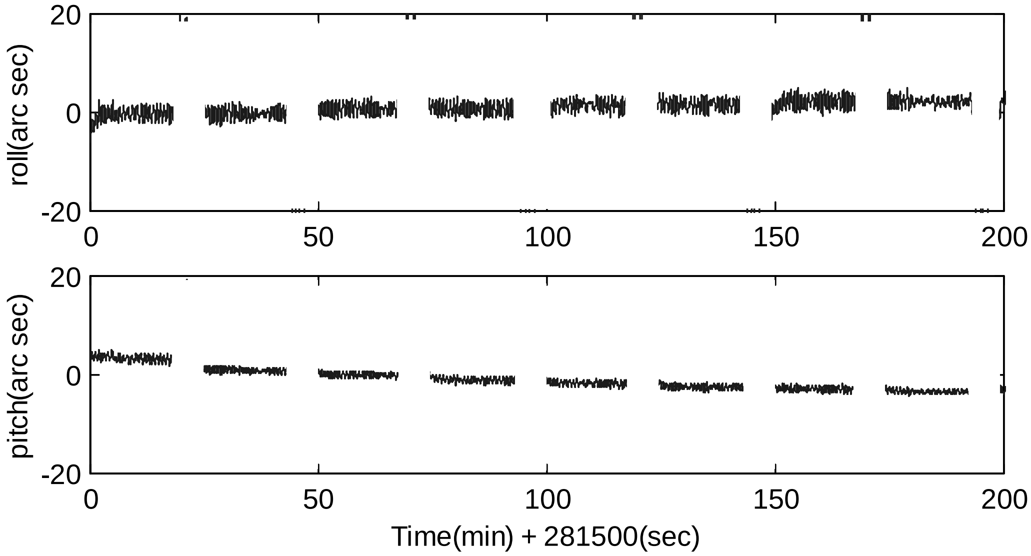

Figure 6.8. Attitude errors induced by anomalous gravity field in Rocky Mountains. Aircraft turns eliminated (Glennie, 1999).

The subjects discussed in this chapter should be carefully considered when designing an airborne survey system. The importance of sensor placement, synchronization, system calibration and alignment accuracy is as important as a proper filtering process. Inadequate decisions on these operation aspects can seriously affect overall system accuracy.

CHAPTER 7

DIRECT GEOREFERENCING OF AIRBORNE IMAGERY BY INS/DGPS - EXPERIMENTAL RESULTS

In this chapter, the mapping performance of an airborne data acquisition system consisting of a strapdown INS, a pair of geodetic GPS receivers and an aerial camera (Figure 7.1) is analyzed. The objective is twofold: first, to provide a detailed description of the 'dynamic' attitude reference which has been used in Chapters 3 and 4 for filter evaluation; second, to test the entire concept of georeferencing by INS/DGPS using the aerotriangulation without ground control as an application.

Preliminary results achieved by this system have been presented in Skaloud et al. (1996), which is believed to be the first publication reporting decimeter level mapping accuracy using aerotriangulation *without any* ground control. Since then, a number of independent experiments have been carried out with more or less comparable success in terms of mapping accuracy (see

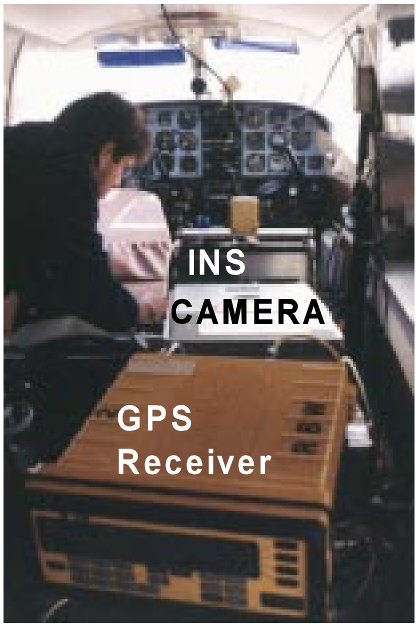

Figure 7.1. Equipment for Direct Georeferencing

for instance, Abdullah, 1997; Reid et al., 1998; Grejner-Brzezinska and Toth, 1998; Cramer and Haala, 1998). It should be noted, however, that small performance variations among these systems cannot be directly interpreted as variations in the quality of the INS/DGPS data, unless similar operational conditions are used (e.g. camera type and quality, image scale, image processing and operational aspects as described in Chapter 6). Nevertheless, although mapping accuracy achieved in a single test may not be considered ‘statistically significant’, these data provides a direct and independent tool for evaluating the relative merits of the algorithms developed for this purpose.

The organization of this chapter is as follows. First, the test flight scenario and the accuracy of trajectory parameters obtained by photogrammetric means is described. Second, the discrepancies between INS/DGPS exterior orientation and the reference values are presented in detail and the improvements due to the band-limiting (Chapter 3) and de-noising (Chapter 4) filter algorithms are evaluated. Last, the coordinates of pre-surveyed check points on the ground are determined by georeferencing independent models, with exterior orientation provided by INS/DGPS.

7.1 Test Flight Scenario and the Accuracy of the Reference Trajectory

A well-defined photogrammetric test field close to Cologne, Germany, has been used for the purpose of in-flight calibration and for the evaluation of the mapping accuracy. The test area has an extension of about 4 x 2 km and is normally used to determine the ground movement of the overburden dump in an open pit mining area. Therefore, about 160 points are marked permanently on the ground and their coordinates are measured in regular time intervals using GPS-supported aerial triangulation. For this test flight, a subset configuration of 47 ground control points in the area has been chosen in such a way that camera orientation parameters can be derived from them with the highest possible accuracy by means of photogrammetry. The 3-D coordinates of 16 control points were determined by adjusting a network of GPS static baselines with a relative positioning accuracy of 1 part per million (1 ppm). In addition, 31 vertical control points were established by leveling and their ellipsoidal heights were determined by adding geoid undulations. To unify the reference systems, the vertical control points had to be transformed from the local German datum using the Bessel ellipsoid to the WGS-84 datum. For reasons explained in Section 6.3, the curvilinear geographical coordinates of all control points given in WGS-84 datum were projected on a plane using the Transverse Mercator projection with the central meridian located in the middle of the flight area at λ=6.46° east of Greenwich. The same projection was also used for transforming the INS/DGPS trajectory.

The GPS receivers selected for the test is a pair of dual frequency receivers Ashtech Z12. The base station was located close to the middle of the test field, about 35 km away from the airport. The inertial navigation system was a Litton LTN-90-100 strapdown system with gyro drift rates of about 0.03 deg/hour. The photogrammetric camera installed in the twin-engine

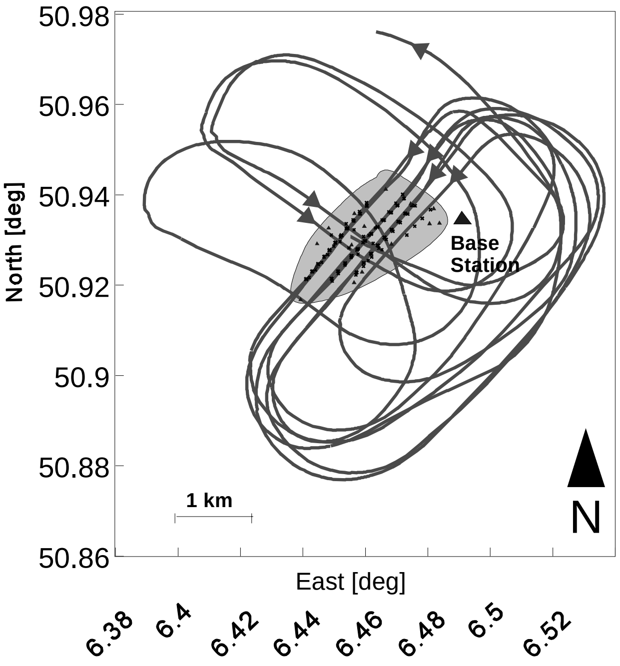

Figure 7.2. Test Flight Scenario.

Partenavia P68C aircraft is a Zeiss RMK A aerial camera with a shutter pulse output being recorded by the receiver in GPS time. The time synchronization with other on-board sensors is realized via a data collection computer receiving raw INS output and GPS data together with a receiver providing the precise 1 pulse per second (PPS) signal.

Eight photogrammetric strips, three of them repetitive, were flown over the test area in early July 1995 (Figure 7.2). The length of the strips differs from approximately 1 to 4 km. From the total number of 168 photographs, a subset of 75 centrally located images was chosen. Together, they form a photogrammetric block with 80% forward and 60% side overlap. The average flying height of about 900 m and the 15 cm camera focal length resulted in a photo scale of 1:6000.

Table 7.1. Observation summary of the photogrammetric block

	Photos	**Tie Points**	**GCP**	**TOTAL**
Observations	0	2378	2068	**4446**
Unknowns	456	192	174	**822**
Degrees of Freedom				**3624**

Due to the large overlaps the photogrammetric block is determined with high redundancy (Table 7.1). The accuracy of the perspective centres of the photographs is estimated by traditional block adjustment using all ground control points. The average position accuracy of the perspective centres is about 3.5 cm (1 σ) in the horizontal and 2 cm (1 σ) in the vertical directions (Figure 7.3). The standard deviations (1 σ) of the orientation angles are depicted in Figure 7.4. Their average values are about 8 arc seconds (σ=0.002 deg) in roll and pitch and 3 arc seconds (σ=0.001 deg) in azimuth. Hence, the parameters of exterior orientation are determined with an accuracy which is at least two times better than that expected from

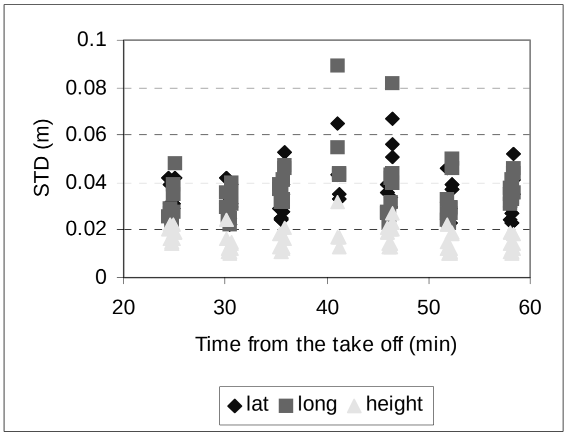

Figure 7.3. Camera positioning accuracy as predicted by the bundle adjustment.

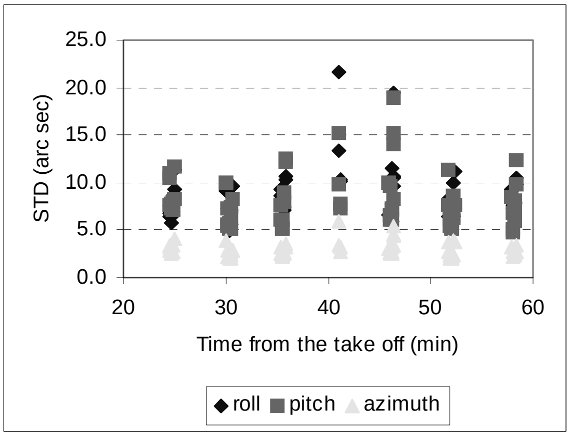

Figure 7.4. Camera orientation accuracy as predicted by the bundle adjustment.

the tested attitude/positioning system. They can therefore be used as a reference and for the purpose of evaluating the orientation displacement between the camera and the inertial system.

7.2 Accuracy of INS/DGPS Exterior Orientation

This section compares the parameters of exterior orientation as independently provided by photogrammetric means and the INS/DGPS system after correcting for the displacement between the sensors (i.e., the vector $\boldsymbol{a}^b$ and the matrix $\boldsymbol{R}_c^b$). While the spatial displacement $\boldsymbol{a}^b$ has been measured by conventional survey methods prior to the mission, the orientation matrix $\boldsymbol{R}_c^b$ has been derived from Equation (6.1) using the values of $\boldsymbol{R}_l^c$ and $\boldsymbol{R}_b^l$ at the first image. The subsequent exposure stations were then used for accuracy evaluation.

The INS/DGPS data has been processed by KINGSPAD (KINematic Geodetic System for Position and Attitude Determination), an integration software package developed at the University of Calgary over the years. This program adopts a decentralized Kalman filtering scheme and has recently been extended to be adaptive in terms of measurement and process noise (Mohamed, 1999). Prior to integration, the inertial signal is first band-limited and de-noised according to the methodology presented in Chapter 3 and Chapter 4. Problematic GPS data, containing either a number of cycle slips or having more than one loss of lock or poor satellite geometry, were processed first in wide-lane mode applying a frequent kinematic OTF ambiguity search. By using the two frequencies for widelaning, a noisy but unbiased flight trajectory was established, which then served for final single frequency processing. During time periods when only four satellites were visible, the INS data was the only source to assist in cycle slip detection. The 64 Hz program navigation output was linearly interpolated to obtain position and attitude for the camera exposure times. The position differences are reflected in Figure 7.5 and have RMS values of 15 cm horizontally and 20 cm vertically using all 70 reference points. The standard deviations for each flight line are

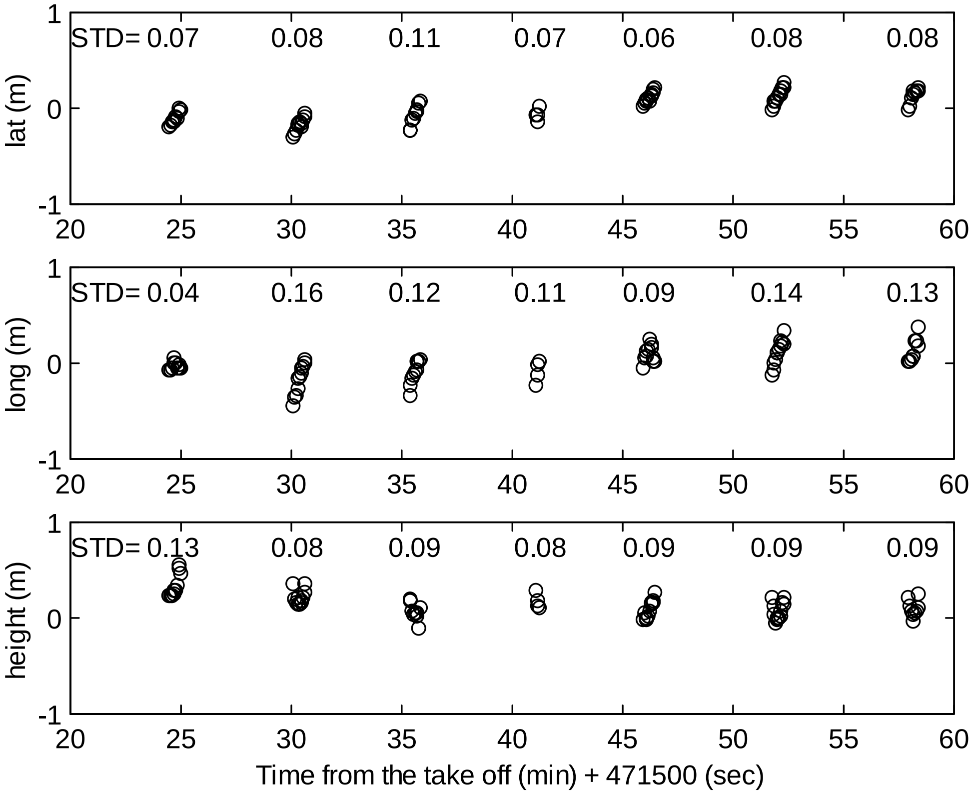

Figure 7.5. Variation in INS/DGPS - camera position.

also displayed in this figure. Their values are smaller, typically about 10 cm or better. The differences between smaller standard deviations for individual flight lines and the total RMS values are attributed to the poor satellite configuration. In order to achieve reasonable geometry, low elevation satellites had to be included into the processing. Even with an elevation mask as low as 10 degrees, only 4 to 5 satellites were simultaneously tracked by the receivers. Moreover, the position drift is apparent in several flight lines especially in the longitude (e.g. flight lines 2,3 and 6). This may be caused by incorrectly estimated ambiguity values for one or more satellites.

The orientation differences for pitch and azimuth are depicted in Figure 7.6 while the variations in roll will be analyzed separately in the following section. As can be seen from the first plot in Figure 7.6, the agreement in pitch is free from biases and the standard

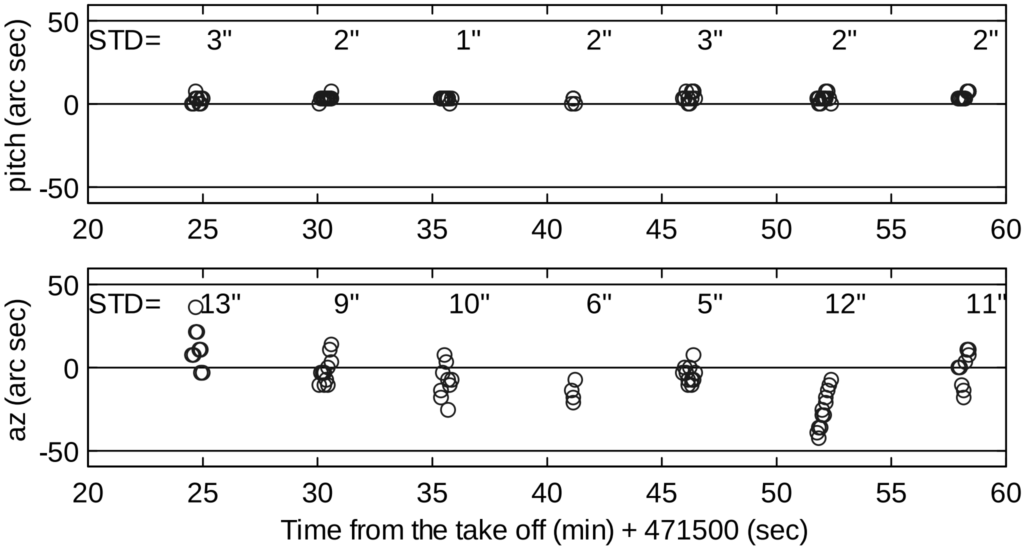

Figure 7.6. Variations in INS/DGPS - camera orientation in pitch and azimuth.

deviations of 1-3 arc seconds are actually lower than the predicted accuracy of the reference (i.e., 8 arc seconds, see Figure 7.4). The azimuth differences have random character within the individual flight lines with mean standard deviations of about 10 arc seconds. However, although a drift is not apparent during the whole test period, the mean of these differences tends to vary between the flight lines with values up to ±20 arc seconds. The total RMS in azimuth is 15 arc seconds.

The orientation improvements due to band limiting and de-noising inertial data will be discussed in detail for azimuth determination. The reasons for choosing this channel are threefold. First, the accuracy of the reference is better in the azimuth (e.g. 3 arc seconds as compared to 8 arc seconds in roll and pitch). Second, the agreement with pitch is already at the resolution of the inertial system. Third, the determination of roll seems to be not reliable in this particular test due to one of the reasons presented in Section 7.3.

The accuracy gains obtained from the band limiting and de-noising techniques are summarized in Figure 7.7 using either integration by means of a conventional Kalman filter (CKF) or its adaptive counterpart (AKF), recently developed by Mohamed (1999). As can be seen in this figure, there is a major improvement (about 70%) either due to inertial data band limiting for the case of the CKF, or the use of the AKF when processing the raw data. Also, it is interesting to observe that after the band limiting and de-noising is applied on the raw data, both KF methods yield approximately the same results. The following discussion analyzes this outcome in detail and clarifies the contributions of each filtering method.

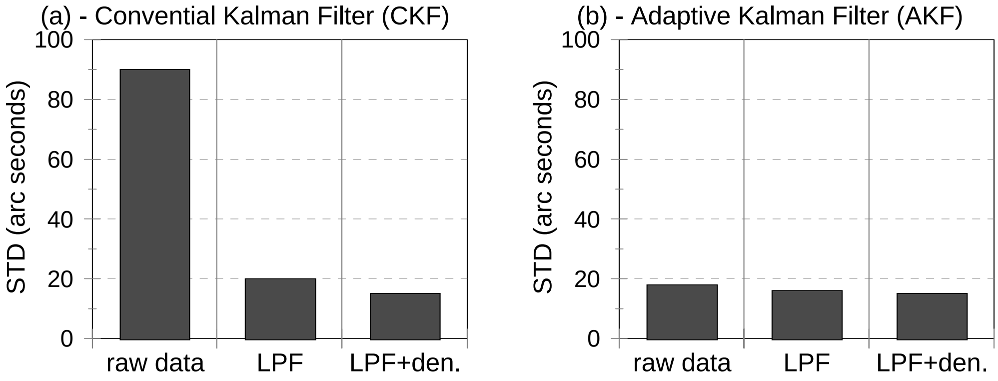

Figure 7.7. Comparison of various filtering approaches with respect to azimuth determination. (a) Conventional Kalman filter, (b) Adaptive Kalman filter. Legend: LPF = Low pass filtering, LPF+den.= Low pass filtering and de-noising. Note: STD = RMS in this case since the mean is zero.

Referring again to Figure 7.7, the improvement due to inertial data band limiting is about 70% for the case of CKF, while it is only 10% when using AKF. Additional improvement of 5-10% on the average is due to de-noising for either case. The results achieved by the AKF correspond more to what is expected from the analysis of short-term noise. This analysis shows that the white-noise component in the *z* (azimuth) channel varies only between 15-25 arc seconds during the whole flight duration as depicted in Figure 4.10. Since some of this noise is already suppressed by data mechanization (i.e., integration acts as a low-pass filter, although with a sub-optimal response), the effect of band limitation is expected to be at the level of 10-30%. This is indeed the case when the AKF is used. Therefore, it could be argued that the differences between the CKF and AKF results are due to errors with signature at lower frequencies such as misalignment errors. Although better estimation of misalignment errors is generally expected from the AKF, this argument explains only the large improvement when processing unfiltered data. In other words, the

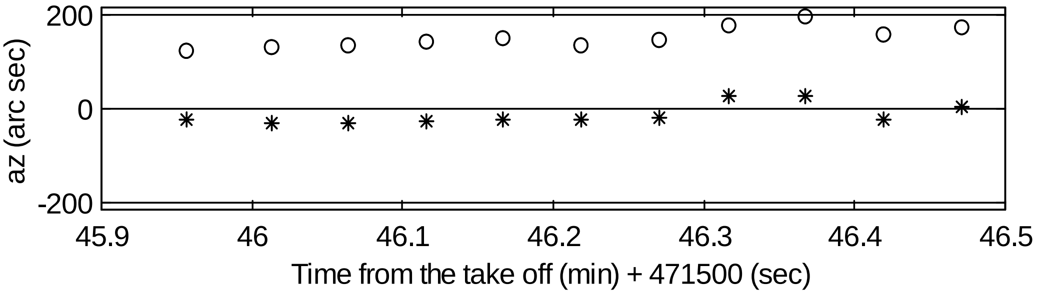

Figure 7.8. Errors in azimuth during the second flight-line.
Data processed were processed by CKF with (*) and withouth (o) band-limitation.

same reasoning does not clarify the substantial improvement achieved by processing the band limited data using CKF, because the reduction of the high frequency noise is not correlated with the orientation errors due to the misalignment. Therefore, the factors beyond these discrepancies are most likely related to the following causes: the influence of gyro noise on INS attitude, and the advantages stemming from Kalman filter adaptation. A brief explanation of this problem is given in the next paragraphs.

Schwarz and Wei (1995) provided an analytical proof that random errors in the gyro output cause attitude divergence with modulation depending on the rotation rate. In other words, the process of integration translates the noise in the gyro output into a random attitude bias whose magnitude increases with the rotation rate. A detailed illustration of this effect is depicted in Figure 7.8, which compares the azimuth errors in the second flight line when using CKF on raw and low-pass filtered data, respectively. As can be seen from the figure, the actual error oscillation is quite similar apart from a bias existing between both solutions. Since the flight line is of short duration with little orientation dynamics, the gyro noise does not translate into an obvious bias during this time span. However, the bias ‘builds up’ during the longer time period between the flight lines with rapid heading changes in the turns. On the other hand, if the noise level is substantially reduced prior to the integration, by means of low pass filtering or de-noising, such attitude divergence does not develop.

Similar reasoning can be used for explaining the differences between CKF and AKF results when using unfiltered data as an input. The attitude divergence caused by integrating the noise has most likely a signature similar to misalignment errors, at least during short periods of time. While the CKF considers the misalignment states well estimated after a certain period of time, the AKF can observe such changes indirectly by analyzing its residuals. Therefore, the AKF has the ability to ‘re-estimate’ these states by adjusting the spectral densities and/or the measurement noise. At the same time, if the noise level is substantially reduced prior to the data integration, the differences between CKF and AKF are less apparent as it would be in this case.

In a summary, the conceptual difference between the methodology proposed in this thesis and the AKF with respect to short term inertial noise is as follows. The first approach reduces the short-term noise in the inertial data directly, with relatively small latency (e.g. 1 to 2 seconds) and independently from the GPS signal. The AKF reduces the integrated effect of the short-term noise on the estimated trajectory with a larger latency (typically about 20 seconds) and a performance that depends on filter chosen and the GPS data used.

7.2.1 Analysis of Roll Performance

The attitude differences between the roll provided by INS/DGPS and by photogrammetry are depicted in Figure 7.9. As can be seen from this figure, the time evolution of these differences does not indicate a drift, but the overall variation is considerably larger than that in pitch or azimuth. Indeed, the standard deviations are consistently at the level of 2 arc minutes per flight line with large deviations existing even between successive images. On the other hand, the mean values are consistent between flight lines. Moreover, these variations maintain similar characteristics when different data processing schemes are applied as in the previous section.

In principle, the INS/DGPS navigation system should provide the roll and pitch with a comparable accuracy. Since the accuracy of the reference orientation is also similar in these angles, the larger than expected variations are most likely due to one or all of the following reasons.

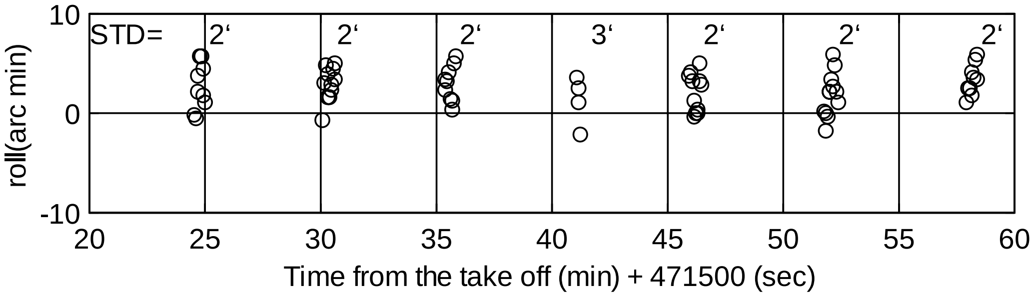

Figure 7.9. Variations in INS/DGPS - camera orientation with respect to roll.

First, the most likely factor causing such large deviations is instability of the camera mount with respected to the inertial system. Due to the time constraints and concerns of the aircraft provider, no firm mount accommodating both devices could be installed in the airplane. Although the inertial system was firmly bolted to the aircraft body and the aerial camera clamped to its holder, the stability of the camera holder with respect to the inertial system is rather questionable. In other words, the response of the camera mount to the motion of the aircraft may cause oscillations of the INS/camera orientation differences along the roll axis. Such oscillations will not exhibit a time dependence, i.e. a drift-like error, but have a stable mean value. Large oscillations with constant mean have been detected in these data.

Second, the oscillatory movement between the camera and the inertial system may be induced by aircraft vibration especially along the roll axis. The level of vibrations along the roll axis is about ten times stronger as compared to pitch or azimuth as can be detected from the two bottom plots of Figure 4.10[1]. This figure shows that the white noise level is 3.6 arc min (~ 0.06°) in the mean with a 1σ uncertainty of 1.2 arc min (0.02°). These values agree well with the 2-3 arc min standard deviations computed for each flight line (Figure 7.9).

Third, the y-gyro in the LTN-90-100 may be experiencing some problems in this particular test. Such suspicion arises again from the analysis of the short-term noise shown in Figure 4.10. During the initial alignment, the level of noise detected in pitch and azimuth is about 1-2 arc seconds and consists of a white noise component and its derivative ($\gamma \approx -2$). In

---

[1] The noise characteristics of pitch and azimuth are very similar.

contrast, the level of noise in roll is considerably larger, above 1 arc min, and has a different character ($\gamma \approx -0.5$). This is rather strange, considering the fact that the inertial system was powered from the batteries and therefore the aircraft engines were not running during this time period.

To conclude this discussion, it should be noted that neither of the reasons mentioned above can be ruled out with sufficient confidence. At the same time, either of them can be solely responsible for the large discrepancies in roll.

7.3 Direct Georeferencing

Once all unknowns in Equation (2.1) have been determined, the target points in the imagery can be directly georeferenced without the need for ground control. In this case, the parameters of interior orientation as well as the displacement between on board sensors are known from calibrations and the parameters of exterior orientation are resolved via INS/DGPS integration. To evaluate the overall performance of direct georeferencing, coordinates of 50 control points were recomputed by means of Equation (2.1) and compared to their reference values. Practically, the computation was performed by using the calibration parameters of interior orientation to correct the measured image coordinates and running the bundle adjustment with *no ground control* and *fixed* parameters of exterior orientation as derived from INS/DGPS. The three dimensional position residuals on all check points are

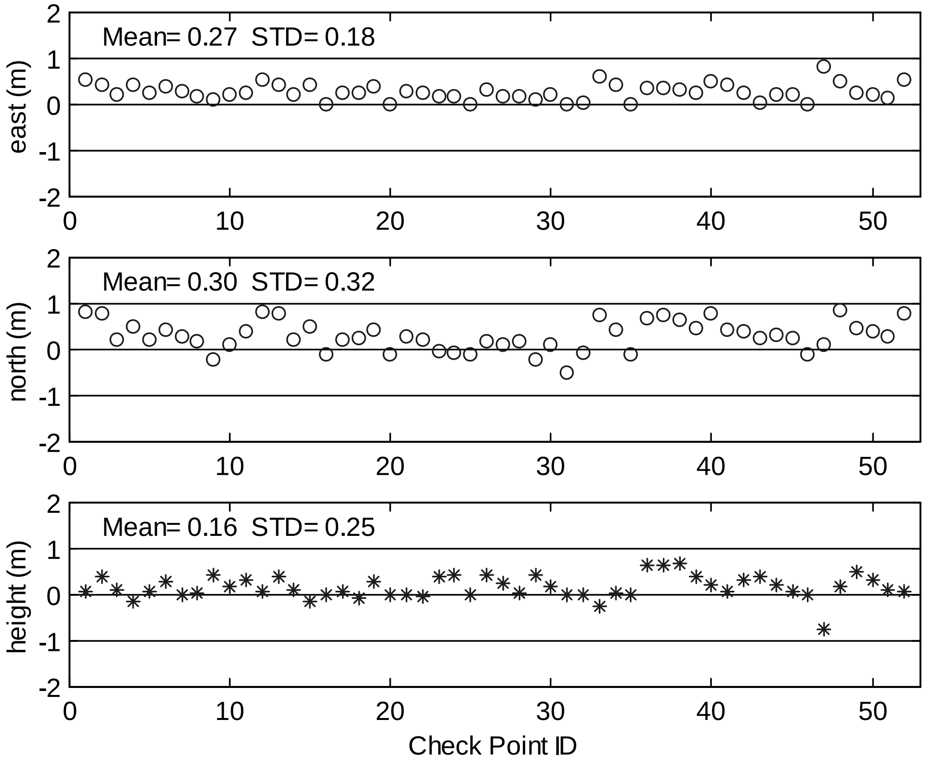

Figure 7.10. Errors in direct georeferencing with respect to ground control points.

depicted in Figure 7.10. The empirical standard deviations computed from these differences are 0.18, 0.32 and 0.25 metres in east, north and height, respectively. Although the maximal deviations are at the sub-metre level, the coordinates of the control points are shifted towards east and north by a mean value of about 30 cm. Since the camera position and orientation were considered as known parameters in the adjustment, errors in their determination are directly propagated into the derived ground coordinates. The non-zero mean values are most likely attributed to biases in the DGPS trajectory caused by the inevitable inclusion of low orbiting satellites. On the other hand, the somewhat larger than expected error spread is very likely caused by the orientation errors. The analysis in the preceding section showed that the attitude information may be contaminated by a relative angular movement in roll between the INS/DGPS and the camera. In this respect, the potential of this particular navigation system most likely has not been fully exploited and the estimate of its mapping accuracy is rather conservative. Should the roll be determined with the accuracy of pitch (i.e., 2-3 arc seconds) it could be concluded that the quality of the attitude component in this particular test is sufficient to achieve mapping accuracy of 10-15 cm. In such a case the major error source would come from the DGPS positioning. However, it remains for future investigation to confirm this potential for longer flight lines and at areas remote from the calibration test field. Nevertheless, the results presented would satisfy all but the most demanding engineering applications.

CHAPTER 8

SUMMARY, CONCLUSIONS AND RECOMMENDATIONS

8.1 Summary

The main objective of this thesis was to scrutinize the method of direct kinematic georeferencing by INS/DGPS with respect to airborne applications. The research led to the following major results:

1) the development of a multi-step filtering algorithm which considerably enhances the well established method of INS-DGPS data integration by means of Kalman filtering,
2) an analytical proof that demonstrates in which cases data integration by means of a centralized filter provides considerable advantages over its decentralized counterpart with respect to the OTF GPS ambiguity estimation,
3) the analysis of system integration and operational procedures, resulting in strategies minimizing the errors in the direct georeferencing process,
4) the practical application of the method to a set of airborne data and the demonstration that decimeter-level accuracy in airborne mapping can be achieved with direct strapdown INS/DGPS georeferencing and without the use of ground control.

The following conclusions and subsequent recommendations can be drawn from this research with respect to individual aspects of this investigation.

8.2 Conclusions

1 a) Minimizing the level of high frequency noise in the inertial signal prior to the integration with GPS data is a vital step for accurate attitude determination in the airborne environment. This can be effectively achieved by combination of band limitation and de-noising using wavelets.

1 b) The band limitation of inertial data by means of low pass filtering removes all noise above a defined threshold. However, since this process is not localized in time the cut-off frequency has to be set well above the motion level to avoid signal distortion. Since inertial data are very sensitive to changes introduced by the filter to the pass-band, it is important to design a filter with minimum phase distortion. This has been accomplished by investigating optimal and sub-optimal designs of FIR filters. Empirical testing showed comparable performance between a number of these filters. The level of improvement in orientation accuracy achieved by band limitation varies considerably according to the power of noise in the stop-band and the type of filter used for integration (i.e., conventional KF versus adaptive KF). The analysis of

available data sets detected attitude improvements of 10-70% depending on a particular system and conditions.

1 c) Testing showed that the spectral method of ‘dither spike removal’ specially designed for strapdown inertial systems with dithered ring-laser gyros does not affect attitude determination in the airborne environment where aircraft vibration is the prevailing short-term noise in the inertial signal.

1 d) The de-noising by wavelet coefficients thresholding can be used either as an alternative to signal band-limitation or better, as its complement. The major advantage of this method is its ability to provide considerable noise reduction without further limiting the signal bandwidth. Therefore, this method is particulary useful in higher dynamics or in other cases when the motion sampling is close to the critical sampling. Another advantage of this approach is the time localization of signal characteristics. This allows to account for variations in the noise structure or its power by adapting the parameters of the noise model. Moreover, this method also makes the suppression of noise with a fractal structure (i.e., $1/f^{\gamma}$) possible. This type of noise has been detected in ring-laser and fibre-optic gyros. The algorithm allowing such filtering has been presented and tested. In summary, if the parameters of a noise model correspond well to reality, the noise reduction achieved by shrinking the wavelet coefficients is better than the one resulting from signal band-limitation.

2 a) After substituting the weights of individual measurements, the presented closed-form expressions for ambiguity search space location and volume clearly show the effect of inertial data with respect to ambiguity resolution. Since the accuracy of a particular inertial system can be predicted well in time by means of covariance propagation, a simple simulation can be used to evaluate its contribution for OTF ambiguity determination without the need of physical testing[1].

2 b) The simulations indicated that by including inertial data, the probability of resolving ambiguities faster and with fewer satellites improves considerably. This improvement is very pronounced for a navigation-grade INS while the benefits of using a tactical-grade system are minimal.

3 a) Hardware integration aspects, such as sensor placement and synchronization, system calibration and initial alignment, are as important for overall system accuracy as optimal data filtering and integration.

---

[1] It should be noted that this is meant in terms of probability (i.e., with respect to the accuracy of the float ambiguities defined by $Q_{\hat{a}}$). To study the contribution of a particular inertial system with respect to the whole norm $(\hat{a}-a)^T Q_{\hat{a}}^{-1}(\hat{a}-a)$, the actual data have to be provided. However, conclusions derived from such analysis would be valid only with respect to the particular data set.

4 a) The feasibility of using INS/DGPS data for the derivation of the parameters of exterior orientation has been demonstrated with actual data from an aerotriangulation. The empirical accuracy of translation parameters is about 0.15 m (1σ) horizontally and 0.20 m (1σ) vertically, while the orientation accuracy is about 3" (σ=0.001 deg) in pitch and 15" (σ=0.003 deg) in azimuth. The present data set does not allow to reliably evaluate the accuracy of roll. If similar accuracy for roll and pitch can be assumed, the DGPS positioning accuracy will be the limiting factor for direct georeferencing.

4 b) Aerotriangulation without *ground control* has been demonstrated with an accuracy level of about 0.3 m (1σ) as compared to 50 check points for 1:6 000 photography. Although the potential of the particular navigation system most likely has not been fully exploited (e.g. Section 7.2.1), these results would satisfy all but the most demanding engineering applications.

8.3 Recommendations

1) The method of de-noising inertial data using wavelets is recommended to be further investigated with respect to the choice of the base function, soft or hard thresholding and correlated noise models for other gyro technologies. In general, this method is recommended over low-pass filtering whenever the noise model can be considered

reliable. Future research should also investigate its applicability with respect to the GPS signal.

2) Since the implementation of centralized Kalman filtering considerably increases the probability of resolving ambiguities faster and with fewer satellites as compared to its decentralized counterpart, this form of filtering is recommended for applications of direct georeferencing by INS/DGPS.

3) The imaging sensor is recommended to be mounted together with the inertial system on a common, solid structure connected to the aircraft via vibration absorbers. The spatial distance between individual sensors must be kept as small as possible.

4) The synchronization between all sensors should be implemented using centralized hardware integration techniques, reducing the maximal uncertainties to less then 10^{-4} s.

5) In-flight alignment is recommended over the static alignment. Implementation of this method results in better time efficiency when using navigation-grade INS and allows use of tactical-grade INS without the need of transfer alignment. Moreover, increased dynamic during the in-flight alignment allows better estimation of other error parameters used in the Kalman filter, which subsequently improves the accuracy of the navigation system.

6) The calibration of orientation differences between the imaging sensors and the inertial system has to be done with extreme care since it constitutes a limiting factor for the overall accuracy, especially for digital imagery of a smaller format. Alternatives to the in-flight calibration should be investigated. This may include parking the aircraft in a hangar and placing a cluster of prisms underneath to observe control points on the ceiling, or using some other form of ‘static’ calibration outside the aircraft if both devices remain mounted on a solid common structure.

7) The feasibility of using INS/DGPS parameters for exterior orientation should be further tested in terms of repeatability and in areas remote from the actual calibration field. Such testing is important to confirm the technology and system robustness needed in an actual production environment.

8) Ongoing research in INS/DGPS trajectory determination will directly impact the method of direct georeferencing by means of this technology. Special attention should be given to investigations in the multi-model/adaptive form of Kalman filtering, atmospheric modeling, carrier phase networks and ambiguity determination over longer baselines.

REFERENCES

Abdulah, Q. (1997). Evaluation of GPS-Inertial Navigation System for Airborne Photogrammetry, ASPRS/MAPPS Softcopy Conference, Arlington, Virginia, July 27-30.

Asch, T, Silva, R, Brown, A, and La Mance, J. (1995). GPS/Inertial Mapping (GIM) System for Real Time Mapping of Roadways Using WADGPS, Proceedings of the Institute of Navigation, ION GPS-95, Palm Springs, CA, USA, September 12-15, pp. 1825-1830.

Bielas, M. S. (1994). Stochastic and dynamic modeling of fiber gyros, Proc. of the SPIE, Vol. 2292 Fiber Optics and Laser Sensors XII, pp. 240-254.

Bossler J. D, Goad C. and Novak, K. (1993). Mobile Mapping Systems, New Tools for the fast Collection of GIS Information, GIS'93, Ottawa, Canada, pp.306-315, March 23-35.

Britting, K.R. (1971). Inertial Navigation System Analysis, Wiley-Interscience, New York.

Bruton, A.M., Glennie, C.L, Schwarz, K.P. (1999a). Differentiation for Precision GPS Velocity and Acceleration Determination, GPS Solution, Vol. 2, No. 4.

Bruton, A.M., Skaloud J., Schwarz, K.P. (1999b). Denoising of Signals in Inertial Navigation Systems (INS) Using Wavelets. In preparation.

Cannon, M.E. (1991). Airborne GPS/INS with an Application to Aerotriangulation, Report No. 20040, Department of Geomatics Engineering, The University of Calgary, Canada.

Chaer, W.S, Bishop, R.H., Ghosh, J. (1997). A Mixure-of-Experts Framework for Adaptive Kalman Filtering. IEEE Trans. on systems, man, and cyberntetics - part B: cybernetics, Vol. 27, No. 3, June, pp. 452-464.

Cohen, C. and Parkinson B. (1992). Aircraft Applications of GPS Based Attitude Determination, Proceedings of ION GPS'92, Fifth International Technical Meeting, Albuquerque, pp. 775-282,.

Cosandier, D., T.A. Ivanco, M.A. Chapman and M. Dylke (1994). The Integration of a Digital Elevation Model in casi Image Geocorrection, Presented at the First International Airborne Remote Sensing Conference ad Exhibition, Strasbourg, France, September 11-15.

Counselman, C.C., Gourevitch, S.A. (1981). Miniature interferometer terminals for earth surveying: ambiguity and mulipath with the Global Positioning System. IEEE Transactions on Geoscience and Remote Sensing. Vol. Ge-19, No. 4 October, pp. 244-252.

Cramer, M., Haala, N.(1998). Direct Exterior Orientation of Airborne Sensors, Internal report of the Institute for Photogrammetry, Stuttgart, Germany.

Czompo, J. (1990). Use of Spectral Methods in Strapdown ISS Data Processing, Proceedings of the International Symposium on Kinematic Systems for Geodesy, Navigation and Remote Sensing, Banff, September 10-14, Springer-Verlag, New York.

D'Appolito, J.A., Roy, K. J. (1971). Satellite/Inertial Navigation System Kalman Filter Design Study. Tech. Rep. AFAL-TR-71-178, Air Force Avionics Laboratory. Wright-Patterson AFB, Ohio.

Donoho, D.L., Johnstone, I.M. (1994). Ideal spatial adaptation by wavelet shrinkage, Biometrika, 81, 3, pp. 425-455.

Donoho, D.L., Johnstone, I.M. (1995). Adapting To Unknown Smoothness via Wavelet Shrinkage, Journal of the American Statistical Association, Vol. 90, No. 432, December, pp. 1200-1224.

El-Mowafy, A. (1994). Kinematic Attitude Determination from GPS, UCGE Report #20074, Department of Geomatics Engineering, The University of Calgary, Canada.

El-Sheimy, N., Schwarz, K.P. (1994). Integrating Differential GPS with and Inertial navigation System (INS) and CCD Cameras for a Mobile GIS Data Collection System. Proc. 'The Canadian Conference on GIS', Ottawa, Canada, June 6-10, pp. 241-248.

El-Sheimy, N. (1996). The Development of VISAT-A Mobile Survey System for GIS Applications, UCGE Report #20101, Department of Geomatics Engineering, The University of Calgary, Canada.

Erickson, G.W. (1993). An Overview of Dynamic and Stochastic Modeling of Gyros, Proc. of the National Technical Meeting of the ION, January, pp. 339-351. .

Eueler, H.J, Landau H. (1992). Fast GPS ambiguity resolution on-the-fly for real-time applications, Proc. of Sixth International Geodetic Symposium on Satellite Positioning, Columbus, OH, March 17-20, pp.650-659.

Farrell, J.L. (1976). Integrated Aircraft Navigation, Academic Press, New York.

Fox, R, Taqqu, M.S, (1986) "Large-Sample Properties of Parameter Estimates for Strongly Dependent Stationary Gaussian Time Series", *Ann. Stat.*, Vol. 14, No. 2, pp. 517-532.

Frei, E. (1991). Rapid differential positioning with the Global Positioning System, PhD thesis, University of Berne, Switzerland, Geodetic and Geophysical Studies in Switzerland, Vol 44.

Friess, P. (1986). A simulation study on the improvement of aerial triangulation by navigation data, ISPRS Symposium, Commission III, Rovaniemi.

Gelb, A. (1974). Applied Optimal Estimation, The M.I.T. Press, Cambridge, Massachusetts.

Glennie, C.L., Schwarz, K.P. (1999). A Comparison and Analysis of Airborne Gravimetry Results From Two Strapdown Inertial/DGPS Systems, excepted for publication in Journal of Geodesy.

Glennie, C.L. (1999). An analysis of airborne gravity by strapdown INS/DGPS. Ph.D. thesis, Department of Geomatics Engineering, The University of Calgary. February 1999.

Goldfarb, J.M. (1987). Aerotriangulation Using An INS-Differential GPS, Report 20022, Department of Surveying Engineering, The University of Calgary, Canada.

Greenspan, R.L. (1995). Inertial navigation technology from 1970-1995. NAVIGATION, Journal of The Institute of Navigation, Vol 42, No. 1., pp. 165-186.

Grejner-Brzezinska, D.A., Toth, C.K. (1998). Airborne Remote Sensing Multi-Sensor System: Development, Testing and Applications, Western Workshop on Global Positioning System in Forestry, Kelowna, BC, Canada, November 16-18.

Grewal, M. S., Andrews A.P. (1993). Kalman Filtering - Theory and Practice. Prentice Hall.

Hammada, Y. (1996). A comparison of filtering techniques for airborne gravimetry, UCGE Report #20089, Department of Geomatics Engineering, The University of Calgary, Canada.

Han S., Rizos Ch. (1997). Comparing GPS Ambiguity Resolution Techniques, GPS World, p. 54-61, October.

Hatch, R. (1990). Instantaneous ambiguity resolution, ION GPS-95, Palm Springs, Sept. 12-15, pp. 1145-1153.

Hein, G.W, Baustert G., Eisfeller, B., Landau H. (1988). High Precision Kinematic GPS Differential Positiong: Experiences, Results, Integration of GPS with a Ring Laser Strapdown Inertial System, Proceedings of ION-GPS 88, Colorado Springs, Colorado. September 19-23.

Hein, G.W., Werner W. (1995). Comparison of different on-the-fly ambiguity resolution techniques, ION GPS-95, Palm Spring, California, September 12-15.

Kaiser, J.F. (1974). Non-recursive Digital Filter Design Using the I_o-Sinh Window Function, Proc. 1974 IEEE International Sym. On Circuits an Systems, San Francisco, pp.20-23, April.

Kalman, R. E. (1960). New Approach to Linear Filtering and Prediction Problems. Trans. ASME J. Basic Eng. 82, pp. 34-45.

Kay, S.M., Marple, S.L. (1981). Spectrum Analysis - A Modern Perspective, Proc. of the IEEE, Vol. 69, No. 11, November.

Kleusberg, A., Teunissen, P.J.G. (1996). GPS for Geodesy. Lecture notes in earth sciences No. 60, Springler-Verlag.

Krakiwsky E.J., Lachapelle G., Schwarz K.P. (1990). Assessment of Emerging Technologies for Future Navigation Systems in the Canadian Transportation Sector, UCGE Report #60007, Department of Geomatics Engineering, The University of Calgary, Canada, July.

Laird, N.M., Dempster, A.P., Rubin, D.B. (1977). Maximum Likelihood from Incomplete Data via the EM Algorithm, Annals Royal Statistical Society, pp. 1-38, December.

Levy, L.J. (1996). Suboptimality of Cascaded and Federated Kalman Filters. Proc. of the 52nd Annual Meeting of the ION, Cambridge, MA, June, pp. 399-407.

Li, Z., Schwarz, K. P. (1995) Chaotic Behavior in Geodetic Sensors and Fractal Characteristics of Sensor Noise, Proceedings of IAG Symp. # 114: Geodetic Theory Today (ed. F. Sanso), L'Aquila, Italy, May 30-June 4, published by Springer, pp. 246-258, 1995.

Liu, Z. (1992). Comparison of Statistical Methods for the Alignment of Strapdown Inertial Systems, Report No. 20047, Department of Geomatics Engineering, The University of Calgary.

Lu, G., Lachapelle, G., Cannon, M.E. and Vogel B. (1994). Performance analysis of a shipborne gyrocompass with a multi-antenna GPS system, IEEE Symposium on Position Location and Navigation (PLANS), pp. 337-343.

Macdonald, D. A., De Vries, T. W. and Merna, D. (1996). Flexible Software Implementation for a Miniature Integrated GPS/INS Tactical System, Proceedings of ION GPS-96, Kansas City, Missouri , pp. 1001-1008.

Magil, D.T. (1965). Optimal Adaptive Estimation of Sample Stochastic Processes. IEEE Trans. on Automatic Control, AC-10(4), October, pp. 434-439.

Mandelbrot, B.B., Van Ness, H.W. (1968) Fractional Brownian motions, fractional noises and applications, SIAM Rev., Vol. 10, October, pp. 422-436.

Maybeck P. S. (1979). Stochastic Models, Estimation and Control, I. New York, Academic Press, Inc. (republished by Navtech, 1994).

Maybeck P. S. (1982). Stochastic Models, Estimation and Control, II. New York, Academic Press, Inc. (republished by Navtech, 1994).

Merhav, S. (1996). Aerospace Sensor Systems and Applications, Springer Verlag, Berlin.

Mohamed, A.H. (1999). Adaptive Kalman Filtering for INS/GPS, Journal of Geodesy, accepted for publication (in press).

Mostafa, M.M.R, Schwarz, K.P., Chapman, M.A. (1998). Development and Testing of an Airborne Remote Sensing Multi-Sensor System, ISPRS Commission II, Symposium on Data Integration: Systems and Techniques, Cambridge, UK, July 13-17.

Ninness, B. (1998). Estimation of 1/f Noise, IEEE Transaction on Information Theory, Vol. 44, No. 1, January, pp. 32-46.

Oppenheim, A.V., Schafer, R.W. (1989). Discrete-Time Signal Processing, Prentice-Hall, Inc.

Parks, T.W., McClellan, J.H. (1972a). Chebyshev Approximation for Non-recursive Digital Filters with Linear Phase, IEEE Trans. Circuit Theory, Vol. CT-19, pp. 189-194, March.

Parks, T.W., McClellan, J.H. (1972b). A Program for the Design of Linear Phase Finite Impulse Response Filters, IEEE Trans. Audion Electronics, Vol. AU-20, No. 3, pp. 195-199, August.

Pilgram, B., Kaplan, D.T. (1998). A comparison of estimators for 1/f noise, Physica D, Vol. 114, pp. 108-122.

Rabiner, L.R, Gold, B. (1975). Theory and Applications of Digital Signal Processing, Prentice-Hall.

Reid, D.B., Lithopoulos, E., Hutton, J. (1998). Position and Orientation System for Direct Georeferencing (POS/DG), ION 54th Annual Meeting, Denver, Colorado, June 1-3, pp. 445-449.

Rockwell International (1996). C-MIGITS II - Integrated GPS-INS, Users' Guide.

Savage, P.G. (1978). Strapdown Sensors, in AGARD Lecture Series No. 95, NATO, Neuilly sour Seine.

Scherzinger, B. (1997). A Position and Orientation Post-Processing Software Package for Inertial/GPS Integration (POSPorc), International Symposium on Kinematic Systems in Geodesy, Geomatics and Navigation - KIS97, Banff, Alberta, Canada, June 3-6, pp. 197-204.

Schwarz, K.P., Fraser C.S., Gustafson, P.C. (1984). Aerotriangulation without Ground Control, International Archives of Photogrammetry and Remote Sensing, Vol. 25, Part A1, Rio de Janeiro, June 16-29.

Schwarz, K. P., Chapman, M. A., Cannon M.E and Gong, P. (1993). An Integrated INS/GPS Approach to the Georeferencing of Remotely Sensed Data, Photogrammetric Engineering & Remote Sensing, Vol. 59, No. 11, pp. 1667-1674.

Schwarz, K.P., Wei, M. (1995). Modeling INS/GPS for Attitude and Gravity Applications, 3rd International Workshop for High Precision Navigation, Stuttgart, Germany, April 3-6.

Schwarz, K.P. (1998). Sensor Integration and Image Georeferencing. Lecture notes for Duane C. Brown International Summer School in Geomatics, The Ohio State University, Columbus, Ohio, July 9-11.

Siouris, G.M. (1993). Aerospace Avionic Systems - A Modern Synthesis. Academic Press, Inc.

Skaloud J., Cosandier D., Schwarz, K. P and Chapman, M. A. (1994). GPS/INS Orientation Accuracy Derived From A Medium Scale Photogrammetry Test, International Symposium on Kinematic Systems in Geodesy, Geomatics and Navigation - KIS94, Banff, Alberta, Canada, August 30-September 2, pp. 341-348.

Skaloud, J., Cramer, M., Schwarz, K.P. (1996). Exterior Orientation By Direct Measurement of Camera Position and Attitude, XVII. ISPRS Congress, Vienna, Austria, July 9-19, Int. Archives of Photogrammetry and Remote Sensing, vol 31, part B3, pp. 125-130, 1996.

Skaloud, J., Li, Y.C and Schwarz K.P, (1997) Testing and Analysis of C-MIGITS II Integrated GPS/INS, Proc. of the International Symposium on Kinematic Systems in Geodesy, Geomatics and Navigation - KIS 97, Banff, Canada, June 3-6, pp. 161-166.

Skaloud, J. and Schwarz, K.P. (1998). Accurate Orientation for Airborne Mapping Systems, ISPRS Commission II, Symposium on Data Integration: Systems and Techniques, Cambridge, UK, July 13-17, pp. 283-290.
Also accepted for publication in the Journal of Photogrammetry and Remote Sensing.

Skaloud, J. (1998). Reducing The GPS Ambiguity Search Space by Including Inertial Data, ION-GPS 98, Nashville, Tennessee, Sept. 15-18, pp. 2073-2080.

Skaloud J., Bruton, A.M., Schwarz K.P. (1998). Detection and Filtering of Short-Term ($1/f^{\gamma}$) Noise in Inertial Sensors, submitted to the NAVIGATION, Journal of The Institute of Navigation, November.

Stewart, I. (1989). Does God Play Dice? The mathematics of Chaos, Basil Blackwell Inc., Cambridge, MA.

Strang, G., Nguyen, T. (1996). Wavelets and Filter Banks, Wellesley-Cambridge Press.

Teunissen, P.J.G. (1993). Least-squares estimation of the inter GPS ambiguities", Invited lecture, Section IV Theory and Methodology, IAG General Meeting, Beijing, August, also in Delft Geodetic Computing Center LGR series, No. 6, 16 pp.

Teunissen, P.J.G., Jonge de P.J., Tiberius C.C.J.M (1996). The Volume of the GPS Ambiguity Search Space and its Relevance for Integer Ambiguity Resolution, ION GPS-96, Kansas City, Missouri, Sept 17-20, pp.889-898.

Teunissen, P.J.G. (1997a). Precision, volume and eigenspectra for GPS ambiguity estimation based on the time-average satellite geometry. Journal of Geodesy, Vol 71, p.290-301.

Teunissen, P.J.G., (1997b). A canonical theory for short GPS baselines, Part I-IV", Journal of Geodesy, Vol 71, p.320-326, 389-401, 486-501, 513-525.

Tiberius, C.C.J.M. (1998). Recursive data processing for kinematic GPS surveying, NCG-Nederlandse Commissie voor Geodesie, Delft, Netherlands.

Wei, M., Schwarz K.P. (1995). FAST Ambiguity Resolution Using an Integer Nonlinear Programming Method, ION GPS-95, Palm Spring, California, September 12-15.

Wei, M., Schwarz, K.P. (1998) Flight test results from a strapdown airborne gravity system, Journal of Geodesy, Vol. 72, pp. 323-332.

Wong, R.V.C., Schwarz, K.P. (1983). Dynamic Positioning with an Integrated GPS-INS Formulae and Baseline Tests, Publication 30003, Department of Surveying Engineering, The University of Calgary.

Wornell, G.W., Oppenheim, A.V. (1992). Estimation of Fractal Signals from Noisy Measurements Using Wavelets, IEEE Transactions on Signal Processing, Vol. 40, No. 3, March, pp. 611-623.

Wornell, G.W. (1996). Signal Processing with Fractals - A Wavelet Based Approach, Prentice Hall, N.J.

Zhang, G., Schwarz, K.P., El-Mowafy, A. (1995). A Low-Cost Positioning/Attitude Reference System for Airborne Remote Sensing. Proc. of ISPRS/IAG/FIG Workshop on Integrated Sensors Orientation, Barcelona, September 4-8, pp. 248-260.

APPENDIX A

Summary of the EM algorithm (after Wornell and Oppenheim, 1992). The estimates of the parameters γ, σ^2 and $\sigma_w{}^2$ generated on the l^{th} iteration of the algorithm are denoted by $\hat{\gamma}^{[l]}$, $\hat{\sigma}^{2[l]}$, and $\hat{\sigma}_w^{2[l]}$, respectively.

E step: Estimate the noise and signal portions of the wavelet coefficient variances at each scale $m \in \mathbf{M}$ using current estimates of the parameters $\hat{\gamma}^{[l]}$, $\hat{\sigma}^{2[l]}$, and $\hat{\sigma}_w^{2[l]}$:

$$S_m^w(\hat{\boldsymbol{\Theta}}^{[l]}) = A_m(\hat{\boldsymbol{\Theta}}^{[l]}) + B_m^w(\hat{\boldsymbol{\Theta}}^{[l]})\hat{\sigma}_m^2$$

$$S_m^x(\hat{\boldsymbol{\Theta}}^{[l]}) = A_m(\hat{\boldsymbol{\Theta}}^{[l]}) + B_m^x(\hat{\boldsymbol{\Theta}}^{[l]})\hat{\sigma}_m^2$$

where,

$$A_m(\hat{\boldsymbol{\Theta}}^{[l]}) = \frac{\hat{\sigma}_w^{2[l]} \cdot \hat{\sigma}^{2[l]}\left[2^{\hat{\gamma}[l]}\right]^{-m}}{\hat{\sigma}_w^{2[l]} + \hat{\sigma}^{2[l]}\left[2^{\hat{\gamma}[l]}\right]^{-m}}$$

$$B_m^w(\hat{\boldsymbol{\Theta}}^{[l]}) = \left(\frac{\hat{\sigma}_w^{2[l]}}{\hat{\sigma}_w^{2[l]} + \hat{\sigma}^{2[l]}\left[2^{\hat{\gamma}[l]}\right]^{-m}}\right)^2$$

$$B_m^x(\hat{\boldsymbol{\Theta}}^{[l]}) = \left(\frac{\hat{\sigma}^{2[l]}\left[2^{\hat{\gamma}[l]}\right]^{-m}}{\hat{\sigma}_w^{2[l]} + \hat{\sigma}^{2[l]}\left[2^{\hat{\gamma}[l]}\right]^{-m}}\right)^2$$

M step: Obtain new parameters $\hat{\gamma}^{[l+1]}$, $\hat{\sigma}^{2[l+1]}$, and $\hat{\sigma}_w^{2[l+1]}$ using signal and noise variance estimates from the E step as:

$$2^{\hat{\gamma}[l+1]} \leftarrow \sum_{m \in \mathbf{M}} C_m N(m) S_m^x(\hat{\boldsymbol{\Theta}}^{[l]}) 2^{\gamma m} = 0$$

$$\hat{\sigma}^{2[l+1]} = \frac{\sum_{m \in \mathbf{M}} N(m) S_m^x(\hat{\boldsymbol{\Theta}}^{[l]}) \left[2^{\hat{\gamma}[l+1]}\right]^m}{\sum_{m \in \mathbf{M}} N(m)}$$

$$\hat{\sigma}_w^{2[l+1]} = \frac{\sum_{m \in \mathbf{M}} N(m) S_m^w(\hat{\boldsymbol{\Theta}}^{[l]})}{\sum_{m \in \mathbf{M}} N(m)}$$

where

$$C_m \equiv \frac{m}{\sum_{m \in \boldsymbol{M}} m N(m)} - \frac{1}{\sum_{m \in \boldsymbol{M}} N(m)}$$

APPENDIX B

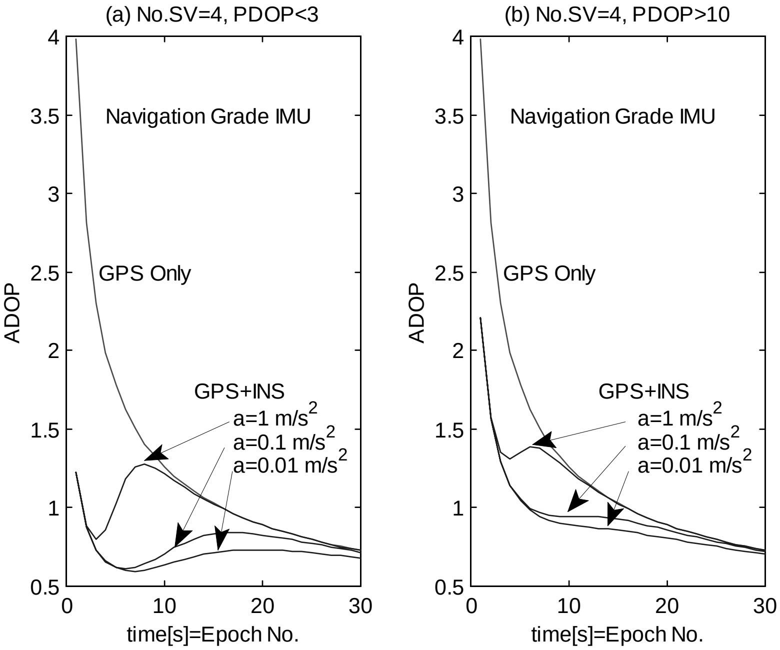

Figure B.1. The ADOP without and with a navigation-grade INS in different dynamics and (a) good geometry, (b) poor geometry; and GPS observations from 4 satellites.

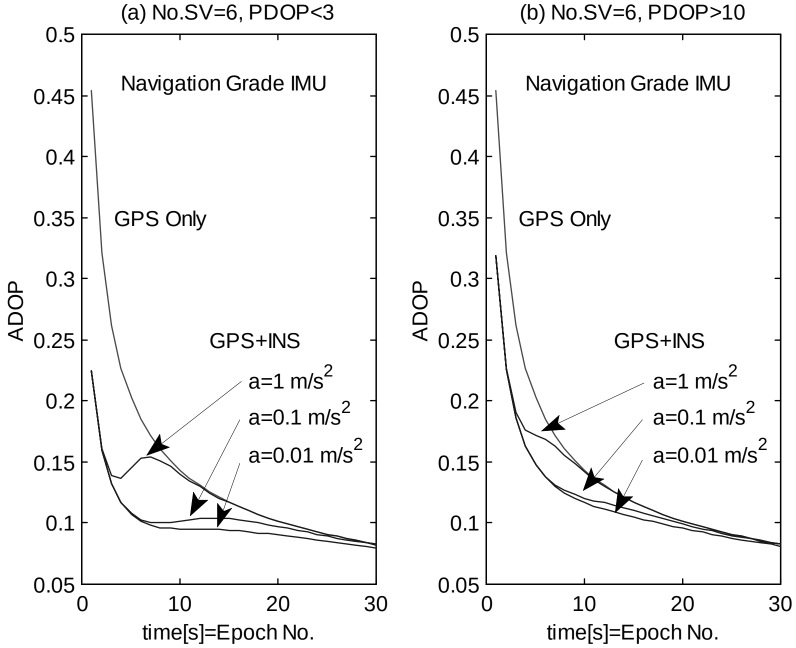

Figure B.2. The ADOP without and with a navigation-grade INS in different dynamics and (a) good geometry, (b) poor geometry; and GPS observations from 6 satellites.